STUDY OF THROUGH WALL IMAGING FOR TARGET DETECTION

A THESIS

Submitted in partial fulfilment of the requirements for the award of the degree of

DOCTOR OF PHILOSOPHY

in

ELECTRONICS AND COMPUTER ENGINEERING

by

ABHAY N GAIKWAD

DEPARTMENT OF ELECTRONICS AND COMPUTER ENGINEERING
INDIAN INSTITUTE OF TECHNOLOGY ROORKEE
ROORKEE-247 667 (INDIA)

JUNE, 2011

INDIAN INSTITUTE OF TECHNOLOGY ROORKEE
ROORKEE

CANDIDATE'S DECLARATION

I hereby certify that the work which is being presented in the thesis entitled **STUDY OF THROUGH WALL IMAGING FOR TARGET DETECTION** in partial fulfilment of the requirements for the award of the Degree of Doctor of Philosophy and submitted in the Department of Electronics and Computer Engineering of the Indian Institute of Technology Roorkee, Roorkee is an authentic record of my own work carried out during a period from July 2007 to June 2011 under the supervision of Dr. Dharmendra Singh, Associate Professor and Dr. M J Nigam, Professor, Department of Electronics and Computer Engineering, Indian Institute of Technology Roorkee, Roorkee.

The matter presented in this thesis has not been submitted by me for the award of any other degree of this or any other Institute.

(ABHAY N GAIKWAD)

This is to certify that the above statement made by the candidate is correct to the best of our knowledge.

(Madhav Ji Nigam)
Supervisor

(Dharmendra Singh)
Supervisor

Date: 27/06/2011

The Ph.D. Viva-Voce Examination of **Mr. Abhay N Gaikwad**, Research Scholar, has been held on 06/01/2012

Signature of Supervisors

Signature of External Examiner

To my mother

Abstract

Through wall imaging (TWI) is one of the most rapidly emerging technologies where it tries to 'see' through visually opaque material like different types of walls and detect and image various targets behind the wall. It is a challenge for current researchers to design TWI system as well as interpret its data. The detection of targets becomes more challenging when no *apriori* information of walls and targets is available. TWI scene may consist of various types of targets with different shapes and material properties (dielectric). Thus TWI system should have the capability to detect, locate, classify the objects and should be able to obtain size and shape of objects present in room which will be useful to the end user for interpretation.

It is well known that radar suffers with strong clutter problems. The signal received from radar consists of desired response of target with other signals arising mainly from radar system parameters, wall reflections, environment, and multiple reflections. The undesired component in the received signal is referred as clutter. In spite of tremendous amount of work by various researchers, it is difficult to select a suitable clutter reduction technique by which target detection accuracy can be enhanced and false target detection reduced.

In TWI, with several indoor objects of different material and shapes, robust detection and classification is an important area of concern to end users. An important step towards classification of targets is thresholding. Several algorithms have been proposed by researchers for computing optimum threshold level in order to discriminate between targets and background. Thresholding becomes difficult when target and background level posses substantially overlapping distribution. Thus optimum thresholding technique is required to be explored in TWI images.

There are different levels of obtaining information in TWI system depending on the application. Basic level which is called as 0-D provides information about presence of

target only. To get the location of the target, the next level 1-D is used which is also called as A-scan or range profile. But it does not indicate how many targets are present in cross range. B-scan system provides this information along with their locations. B-scan is a collection of A-scans recorded along scanning line. The highest level of information is provided by C-scanning which adds a third dimension of height to that of a B-scan system. C-scan is obtained from ensemble of B-scan. Height information may allow discrimination between targets having different dimension with price paid for more scanning time. In TWI, one of the major thrust in near future can be developing more efficient imaging algorithm for getting more information like size and shape of the target from C-scanning system.

Imaging methods in through wall have gained wide attention. Many imaging algorithms have been developed for TWI. The most commonly used techniques in TWI for image formation are back projection, beamforming, tomographic, ω–k, Kirchhoff's etc. These techniques can be analyzed further to find suitable technique for TWI applications.

The purpose of obtaining images is to extract essential information from images which should be used for recognition of targets. Many techniques have been developed to recognize targets based on feature extraction. Features can be obtained by electromagnetic analysis, time spectral analysis and statistical features. Pattern recognition technique can also be used to identify and classify targets. Very less work has been reported on pattern recognition based object classification in TWI.

So, the present thesis is an effort to detect and classify stationary targets present behind wall as well as to image targets for shape recognition. Therefore the main objectives are:

- Critical analysis of clutter reduction techniques for detection of metallic as well as low dielectric targets
- A novel approach to detect and classify targets based on statistical based techniques
- Study of prevalent imaging techniques for through wall target detection
- Application of pattern analysis techniques for shape recognition

The thesis is divided in seven chapters in which the first chapter provides a basic platform of research work by presenting a brief introduction, motivation, research gaps, problem formulations and details of experimental TWI setup. Experimental

setup is ingeniously assembled which consists of a SFCW radar in UWB range (3.95 GHz to 5.85 GHz) and a 2–D scanning frame. SFCW based radar consists of Rohde & Schwarz Vector Network Analyzer (VNA) ZVB8 and pyramidal horn antenna having bandwidth of 1.9 GHz. The scanner is made of wood which is used to scan the radar in horizontal as well as in vertical direction. SFCW radar system possesses several advantages over impulse type of radar systems. One of the main advantages of the SFCW system is that many sources of time varying measurement error including frequency dependent magnitude and phase variations of connectors, cables, directional couplers and antennas can be removed through calibration.

Data are collected using the designed TWI system for plywood and brick wall for different targets like low dielectric and metal of different shapes. The target considered for low dielectric constant material is Teflon. Different regular shapes like square, rectangular and circle are considered. Data has been collected by varying distances between TWI system and wall, between wall and targets to see the effect of positioning of TWI system on detection of targets. Before data are used for further processing, pre-processing techniques such as external calibrations and velocity corrections are applied. To do velocity corrections, knowledge of wall thickness and dielectric constant is required for which wall characterization has been done.

In Chapter 2, the existing techniques and methods for TWI system are briefly reviewed. The chapter addresses the development in techniques for improving detection, imaging and classification of targets.

Study and critical analysis of various clutter reduction techniques and its implementation on obtained data are presented in Chapter 3. Some of the existing methods for clutter reduction in TWI rely on background subtraction, time gating and spatial filtering. But these techniques have drawback. In background subtraction, clutter remains present if the data is not collected at exactly the same antenna positions and in addition it is not possible in real scenarios to collect data without target. Time gating is successful for targets which are far away from wall but for targets near to wall the target response overlaps in time domain and cannot be separated in time. A spatial filter is used to notch zero spatial frequency which represents wall reflections. This filter may subtract low frequency components of target as well due to practical design constraint of filter. Radar detects high dielectric discontinuities as presence of high contrast causes the reflected signal to be very

strong. The problem of distinguishing the targets becomes more difficult if the target is having dielectric constant near to that of medium of propagation. Thus in TWI if the scene consists of targets having low dielectric constant then important aspect will be to detect the target with low false detection. Presence of clutter and attenuation of signal deepen the problem further. Thus there is a need to provide a solution which can improve low dielectric constant target detection. Therefore, this chapter explores the applicability of different clutter reduction techniques based on statistical signal processing techniques like Singular Value Decomposition (SVD), Principle Component Analysis (PCA), Factor Analysis (FA) and Independent Component Analysis (ICA). To critically analyze different clutter reduction techniques two different data sets were collected in which in first data set a single metal target is kept behind wall and in second data set two targets, Teflon and metal are placed behind the wall. From first data set results, it is observed that metal target peak becomes visible significantly after clutter reduction and false target detection is minimized. The performance of clutter reduction techniques is compared on the basis of signal to clutter ratio. In second data set, the important aspect which is considered is detection of low dielectric constant target in presence of metal target. The raw B-scan image detects only metal target where as Teflon target is not observed due to weak reflection. When the raw B-scan image is processed using clutter reduction techniques, it is observed that only ICA is able to detect Teflon whereas other techniques fail to detect Teflon.

Chapter 4, focuses on statistical based thresholding approach for target detection as well as a probability distribution function based algorithm for target classification. An important step towards detection and good classification result is to extract target information from raw data by reducing clutter to maximum extent. The focus is to classify a metal and low dielectric targets behind the wall. Existences of false targets are observed after clutter reduction technique. After clutter reduction, thresholding is applied to segment the target from the background. Thresholding becomes difficult when low dielectric constant target is used as background gray levels and some of the target pixel intensities are same. Deciding optimum threshold is still a challenge in segmenting target from the background which is essential for correct classification of targets. Existing thresholding methods like maximum entropy, minimum cross entropy, cluster analysis technique, Otsu and statistics based (mean+standard deviation) are critically analyzed. The performance of algorithms is evaluated by

computing two performance measures, sensitivity and specificity. Sensitivity is proportion of pixels correctly identified by algorithms as target and specificity is proportion of pixels correctly identified as non target. The higher the values of these two measures (close to one) the more accurate is the algorithm. It is observed that when threshold value is small, false target detection increases. But detection sensitivity of low dielectric constant is still not adequate. To improve detection of low dielectric constant target and to reduce false alarm further, modified statistical based threshold technique is proposed. It meets the user specified performance requirement that is sensitivity and specificity in order to find optimum value of threshold.

In this chapter after thresholding target discrimination is approached as a classification problem. The statistics of thresholded images is obtained and is use to find probability density functions. Thus statistical method that characterizes radar data can be used to get the information about targets. In past probability distribution of various clutters has been modeled as Weibull, Rayleigh and normal from target detection point of view. But use of probability distribution to classify targets has been given less attention. In this chapter, image statistics after thresholding is evaluated on the basis of their probability distribution function and based on this results target are classified. To obtain statistical analysis of target pixels, various distributions like Normal, Rayleigh, Cauchy and Weibull are applied and best fit is chosen to model it. Probability density function is then obtained from them on the basis of Chi-squared goodness of fit test. It is observed that Weibull distribution fits both targets (metal and Teflon) more accurately than other three distributions. Once the distribution is known, parameters are estimated using maximum likelihood estimator and then the groups of pixels are labeled accordingly. The scale and slope parameter of Weibull distribution is obtained for metal and Teflon targets. Validations of proposed technique is carried out for different set of data where the parameters value are observed and class of target either high dielectric constant material or low dielectric constant material is classified.

The objective of chapter 5 is to explore some of the existing imaging algorithm like back projection, frequency wave number (ω-k) and delay sum techniques. Normal B-scan image depicts low resolution features in image. Since the goal is not only to localize the target but also to improve cross range resolution, synthetic aperture technique is applied. To compare different imaging algorithm, image quality is

measured using metric such as entropy and ratio of standard deviation to mean. Images due to different imaging techniques are obtained on B-scan experimental data. After applying imaging algorithms, a more focused image is obtained compared to Raw B-scan image in which no focusing algorithm is applied. It is observed that the brick wall causes an overall drop in coherence compared to case when plywood wall is used.

The objectives of chapter 6 are (i) C–scan imaging for target detection and (ii) feature extraction and shape recognition using neural network. Instead of using C-scan data for three dimensional image formations, two dimensional images is obtained. This reduces time complexity of imaging algorithm. After observing range profiles the location of target is determined. Either the peak magnitude at target location is taken or energy of pulse obtained by target reflection is taken as value at each grid point in two dimensional images. The obtained image is enhanced using image processing techniques like filtering, interpolation, and thresholding and edge detection. The basis of method of the target detection is thresholding. Though the target can be clearly detected after clutter reduction, the image obtained is still of poor quality. Thresholding helps in enhancement of image quality. For edge detection simple Sobel operator is used. This process detects outlines of an object and boundaries between objects and background of the image. From the resultant image the centre of target can be approximately obtained. Though the target image does not corresponds to actual shape of target, much vital information about the target can be inferred.

To enable reliable recognition of target shape, the essential information or features must be extracted. Features for two different targets should differ as much as possible. To recognize target from its shape, features are extracted using different methods like moment invariant, Fourier descriptor and waveform based technique. The features obtained by all these techniques for single image are combined to form single feature vector. These feature sets are used to train the network to recognize various shapes of targets of obtained data. A simple feed forward network with one hidden layer and one output layer is used. The number of nodes in output layer depends upon different types of shapes used. Since three shapes are used, three nodes are used in output layer. To train neural network on more data, features from images which are synthetically generated for different shapes with different dimensions are used. It is observed that the network is able to recognize shape of targets satisfactorily.

Chapter 7 presents the summary of contributions made in the thesis and future scope of work.

Acknowledgement

It is really difficult for me to acknowledge mere in words the help and support extended by many people. First and foremost, my deepest acknowledgement is extended to my supervisor Dr. Dharmendra Singh who accepted me to study under him and introduced me to the field of radar application. As an exceptional advisor and mentor both academically and personally he offered me spare-less guidance, support and encouragement throughout my doctoral study. It is his precious instructions and guidance that I have overcome a number of difficulties and arrived at this step. I have learnt a lot from him particularly the way he works with zeal and enthusiasm.

I would also like to thank my supervisor Dr. M J Nigam for his generous support and encouragement from time to time. I would like to thank the members of my research committee Dr. Vinod Kumar and Dr. D Ghosh for their helpful comments and suggestions during all my presentations related to research work. I would like to show my gratitude towards Head of the department Dr. S N Sinha for providing all the necessary facilities. I would like to thanks to former and present department research committee chairmen Dr. R Mitra and Dr. Mishra for providing their support in my research work. I am also thankful to Giriji for his help during experimentation.

My sincere appreciation goes to Principal Prof. N M Gatphane and the people at my parent institute Babasaheb Naik College of Engineering, Pusad, Maharashtra for supporting me to pursue Ph.D. I would be failing in my duties if I do not thank Prof. N P Jawarkar and Prof. M M Bundele for helping me and behind me as constant source of inspiration throughout my research. I would like to thank all my teachers whom I met throughout my academic life.

Special appreciations are extended to QIP centre, AICTE, India, for their partial financial support for this research. Special thank are due to the management of my

parent institute for sponsoring me and giving me the opportunity to pursue my Ph. D degree and gain valuable education and experience.

I would also like to thanks all the reviewers of papers for providing many valuable suggestions and criticism which had major influence in the quality of this work. Special recognition to Prof. Vasif Ahmed for editing my research papers and this thesis.

I cordially thank all the team members of remote sensing group in particular Vijaya, Gunjan, Harish, Pooja, Vivek, Dharamveer, Tasneem, Abhishek, Ajay for great team work spirit and friendly atmosphere created in laboratory. Thank are due to Rishi Prakash, Triloki Pant, Shiv kumar Verma and B M Patil for helping me from time to time during my stay at IIT Roorkee. I really enjoyed the time being with them. I thank Rohit, Pramod, Prashant, Vishal and Shashikant for working with me and sharing rounds of discussions where many naïve thoughts have generated.

To all my dear friends I would like to say thank for standing by me at all times by word and deed throughout the years I spent working on this thesis.

My deep gratitude and appreciation goes to my father and my brothers Avinash and Ajit for helping me achieve this vital milestone in my life. I am thankful to my wife Deepali for immense support, devoted sacrifice and prayers made by her for the sake of my success and happiness. It is my ultimate joy to thank my son Shishir and daughter Gauri. Their existence brought tremendous delight to my life during exhaustive research work. Last but not least I would like to thanks each one of them who have helped me directly or indirectly.

Table of Contents

List of Figures

List of Tables

Acronyms

ω-k	wave frequency number
1D	One dimensional
2D	Two dimensional
3D	Three dimensional
ADC	Analog to Digital Converter
BSS	Blind source separation
BW	Band width
CCRA	Classical Clutter Reduction Algorithm
CPI	Coherent Processing Interval
CR	Cross Range
EM	Expectation Maximization
FA	Factor Analysis
FAR	False Alarm Rate
FFT	Fast Fourier Transform
FMCW	Frequency Modulation Continuous Wave
GPR	Ground Penetrating Radar
HPBW	Half Power Beam width
HS	Hyperbolic Summation
ICA	Independent Component Analysis
IFFT	Inverse Fast Fourier Transform
ISAR	Inverse Synthetic Aperture Radar
KLT	Karhunen Loeve Transformation
KYT	Kittler Young Transformation
Lidar	Light Detection and Ranging
MSE	Mean Square Error

PC	Principle Component
PCA	Principle Component Analysis
PDF	Probability Density Function
PSD	Power Spectral Density
PSNR	Peak Signal to Noise Ratio
PSR	Power Spectral Response
Radar	Radar Ranging and Detection
RCS	Radar Cross Section
SAR	Synthetic Aperture Radar
SFCW	Step Frequency Continuous Wave
SN	Sensitivity
SNR	Signal to Noise Ratio
SP	Specificity
STFT	Short time Fourier Transform
SVD	Singular Value decomposition
SVM	Support vector machine
TOSM	Though open short and Match
TWI	Through wall imaging
UWB	Ultra wide band
VNA	Vector Network Analyzer

Chapter 1

Introduction

1.1 Motivation

Nowadays through wall imaging (TWI) is attracting more attention from various researchers because of its use in several civilian as well as in military applications. It is one of the most rapidly emerging technologies where the aim is to 'see' through visually opaque obstacles like different types of walls and detect as well as image various targets present behind the wall. TWI system can be based on either an active or passive technique. Sensors based on ultrasound, millimeter wave radiometry, infrared, Lidar and X-ray can be used for through wall imaging but the most suitable technique is Radar sensor. Ultrasound technique can be used to detect and locate target behind metallic or nonmetallic wall. But the disadvantage is that it cannot be used for imaging due to high resolution requirement. Millimeter wave radiometer uses energies radiated by bodies of targets behind the wall for detection but it works only up to very short distances [97]. Infrared can be used to image target through wall at very short distance as attenuation through wall is very high. X-ray based sensors

provide good imaging quality but are limited to very short range and are expensive and not safe.

Therefore, it is a challenge for current researchers to design TWI radar system for different types of wall i.e., plywood, brick as well as to obtain target information by processing techniques for interpretation of data. The radar techniques often employed in TWI are impulse radar, frequency modulation continuous wave (FMCW), step frequency continuous wave (SFCW) and noise radar that are used to generate wide band of frequencies for detection of hidden targets. SFCW radar works in frequency domain whereas pulse radar works in time domain. In SFCW, the frequency of each signal in the waveform is linearly increased in discrete steps, by a fixed frequency step whereas in time domain impulse radar transmits a short time pulse and receives the backscattered signal by using either sampling receiver or extremely fast analog to digital converters. One of the main differences between both is that impulse radar measures target frequency response simultaneously while SFCW radar measures target frequency response sequentially. The idea of using SFCW radar is not new [124, 185]. But due to its simple design and relatively lower cost, pulse radar dominated the industry. Now with advancement in technology, the cost of microwave components has decreased considerably. So it has become viable to design SFCW based radar system.

SFCW radar system possesses several advantages over impulse type of radar systems. The main advantage of the stepped frequency technique is that it covers wide bandwidth with lower signal distortions due to narrow instantaneous bandwidth. The other advantage of SFCW over impulse is greater measurement accuracy because it is much easier to synthesize a pure tone at a frequency than to measure a time delay i.e., accuracy with which the frequencies are set in SFCW radar is much greater than measurement time used in impulse radar [89]. SFCW has greater dynamic range and lower noise because it can transmit at higher power and uses a very narrow IF bandwidth. High average transmitting power is easier to obtain due to use of continuous wave signal. In SFCW, calibration procedure removes many sources of time varying measurement error. Shaping of pulse is also possible with help of windowing for reducing side lobes. The drawback of SFCW radar is its long data acquisition time. But for a particular application like detection and imaging of stationary targets long data acquisition time is generally in acceptable range.

TWI has different challenges to achieve the goal of detection, classification and recognition of different objects commonly observed behind the wall in a room environment. To meet the challenges, research in TWI is directed mainly in areas of signal processing, pattern analysis techniques, antennas and electromagnetic related issues. One of the challenges in TWI is to produce good quality images that may be used for classification and recognition. The basic rule for producing a good quality of image is that the resolving power of radar must be 1/10 times of maximum dimension of targets [54]. To achieve high resolution, it is important that TWI system is operated at high frequencies. On the other hand radar should transmit signal at low frequency to be able to penetrate through walls [53]. Thus, it is a challenging aspect in TWI radar to produce high quality images with reasonable penetration capability. Based on this, TWI radar can be classified into two categories: first working on low frequencies with good wall penetration capabilities but low spatial resolution and second working on high frequencies with high resolution but with limited penetration capabilities.

Another challenge in TWI is to understand the effect of presence of wall. The effect other than attenuation due to presence of wall on propagation of signal, is a shift in target position. So, TWI system should have the capability to overcome this problem to detect, locate, classify the objects and should be able to obtain size and shape of objects present in room which can be useful to the end user for interpretation. The detection of targets becomes more challenging due to the presence of strong clutter problems. The signal received from radar consists of addition of desired response of target with other signals arising mainly from radar system parameters, wall reflections, environment and multiple reflections. The undesired component in the received signal is referred to as clutter. In practical cases these clutter problems are more complex. Researchers have developed various clutter reduction techniques to enhance the detection accuracy and reduce false target detection [4, 240, 245]. Still, it is challenging to improve detection of weak target response in presence of strong unwanted interfering signal.

In TWI, with several indoor objects of different material properties and different shapes, robust detection and classification is an important area of concern to the end users. First important step is detection and after detection classification if possible. Detection is carried out by using thresholding techniques. Several algorithms have been proposed for computing the optimum threshold level in order to discriminate

between targets and background [39]. Thresholding becomes difficult when target and background level posses substantially overlapping distribution and hence optimum thresholding technique is required to be explored in TWI images. Preliminary work in TWI on target classification is reported [112, 143], but very less reported work is available till now.

One of the major thrust in TWI is to develop efficient imaging algorithm for getting more information about targets. Many imaging algorithms have been developed for TWI and have gained wide attention. The most commonly used techniques in TWI for image formation are back projections [90], beamforming [6] and several other migration algorithms like ω–k, Kirchhoff's migration etc. [162, 244]. These techniques need further analysis to find their suitability for TWI applications.

Another important aspect in TWI is recognition of targets. Essential information should be extracted from targets which should be used for recognition of targets. Many techniques have been developed to recognize a target which is based on feature extraction. Features can be obtained by electromagnetic analysis [66] and time spectral analysis [141]. First order and second order statistics such as mean, standard deviation, entropy and others have been used to recognize target shapes by Mahfouz et al. [138]. Pattern recognition technique can be used to identify and classify targets [170]. Pattern recognition based classification of objects in TWI is an area that needs further exploration.

In nutshell, considerable amount of attention and research is required for dealing different problems of TWI systems. This motivated to develop processing techniques to improve detection, localization and recognition of the targets.

1.2 Contribution of thesis

Present thesis embodies extensive investigation on post processing techniques to detect and classify the stationary targets present behind wall as well as to image the targets for shape recognition. For this purpose SFCW radar is ingeniously assembled in the frequency range of 3.95 GHz to 5.85 GHz. Therefore the main objectives are:

1) Critical analysis of clutter reduction techniques for detection of targets
2) To develop an adaptive approach to detect and classify the targets
3) Study of prevalent imaging techniques for through wall target detection

4) Application of pattern analysis techniques for shape recognition.

1.3 Methodology

Basically, it contains different parts which are as following,

1. To assemble TWI experimental setup
2. Data collection
3. Wall characterization
4. Pre-processing techniques such as calibration and velocity corrections
5. Post processing techniques like clutter reduction, detection, classification, imaging and recognition to obtain the target information.

Explanations up to point four is described in this chapter and the post processing techniques are explained in subsequent chapters.

1.3.1 Experimental setup

SFCW based radar system in a monostatic mode was ingeniously assembled with the help of Rohde and Schwarz Vector Network Analyzer (VNA) ZVB8 and antenna system with scanner as shown in Figure 1.1 for the frequency range of 3.95 GHz to 5.85 GHz. The SFCW radar system parameters are given in Table 1.1. A pyramidal horn antenna with 20 dB gain having bandwidth of 1.9 GHz is used for transmitting and receiving signal. The Half Power Beamwidth (HPBW) of antenna at centre frequency in Azimuthal plane and Elevation plane are found to be $\theta_a = 15.92^\circ$ and $\theta_e = 17.02^\circ$. The antenna is oriented in vertical polarization for data collection. The antenna was mounted on 2D-scanning frame made of wood on which the antenna can slide along horizontal direction and along height. Height of stand on which target is kept is 1 m and scanning starts at 0.5 m above the ground. Types of walls that are used in the experiments are plywood and brick wall. After calibrating VNA by standard two port calibration process i.e., Through Open Short Matched (TOSM), the scattering parameters S_{21} was measured in frequency domain for all the observations [142].

(a) *Important parameters of SFCW based TWI radar system*

The important parameters for TWI are such as SFCW radar parameters, image parameters, type of wall and target parameters.

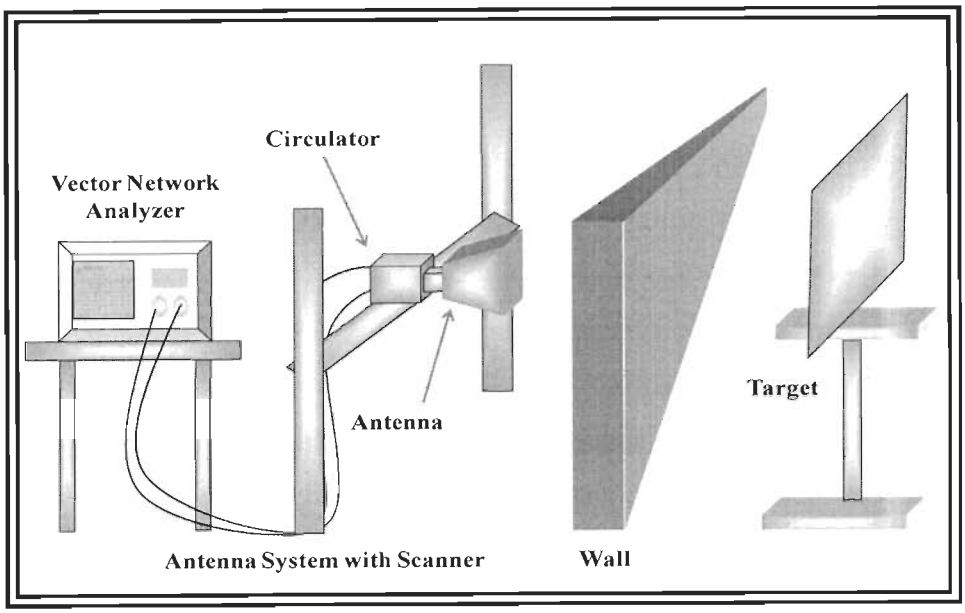

Figure 1.1 Experimental Setup

Table 1.1 SFCW radar parameters

Sr. No	Parameters	Value
1	Frequency range	3.95 to 5.85 GHz
2	Transmitted power	20 dBm
3	Number of frequency points	4001
4	Bandwidth	1.9 GHz
5	Range resolution in air	7.89 cm
6	Polarization	VV
7	Antenna Type	Horn Antenna
8	Gain of Antenna	20 dB
9	Beam Width	15.92^0 and 17.02^0

(i) *SFCW radar basics with parameters*: The waveform for SFCW radar consists of a group of K coherent signals whose frequencies are increased from signal to signal by a fixed frequency increment Δf as shown in Figure 1.2.

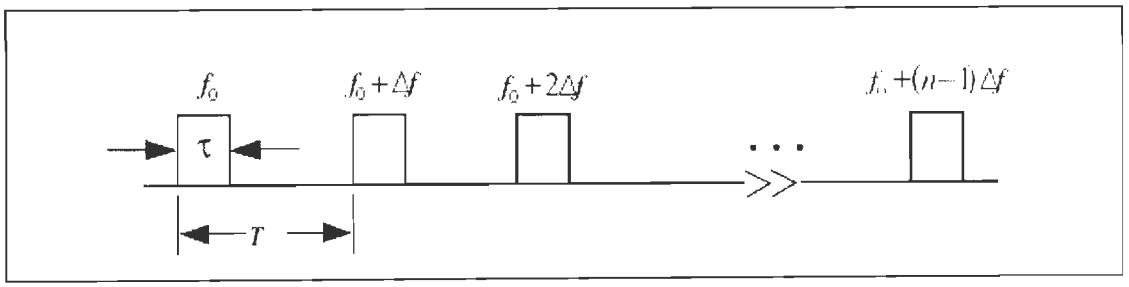

Figure 1.2 Frequency steps over complete bandwidth [210].

SFCW radar measures magnitude and phase of the received signal with respect to the transmitted signal at each stepped frequency. Let the transmitted signal at frequency f_k is

$$s(f_k) = Ae^{-j2\pi f_k t} \tag{1.1}$$

where

$$f_k = f_0 + k\Delta f, \qquad \Delta f = \frac{f_{K-1} - f_o}{K-1} \tag{1.2}$$

where f_0 is the starting carrier frequency, $k = 0,1...K-1$ with K as number of frequencies and Δf *is* the frequency step size, that is, the change in frequency from pulse to pulse. Each pulse is τ seconds wide and the time interval T between the pulses is adjusted for ambiguous or unambiguous range. Each signal dwells at each frequency long enough to allow the reflected signal to reach the receiver. Groups of K signals, also called a burst, are transmitted and received before any processing is initiated to realize the high-resolution potential of this waveform. The burst time, that is, the time corresponding to transmission of K signals will be called the coherent processing interval (CPI) [210].

The signal propagates toward the medium. Any change, within the propagation media as well as any object will produce a return signal which will be captured by receiving system. If only one object is within the unambiguous range then the signal backscattered by that object can be written as

$$s(f,t_i) = [A_1 e^{-j2\pi f_1(t-t_i)} \quad A_2 e^{-j2\pi f_2(t-t_i)} ... A_K e^{-j2\pi f_K(t-t_i)}] \tag{1.3}$$

where A_K is the reflection coefficient for the K^{th} frequency and t_i is the two way propagation delay to the object.

The output of the phase detector can be modelled as the product of the received signal with the reference signal followed by a low pass filter. For real sampling the phase detector output for the Kth signal is $A\cos\varphi_K$ and for the complex sampling it is,

$$Ae^{-j\varphi k} \tag{1.4}$$

where,

$$\varphi_K = 2\pi(f_o + k\Delta f)\frac{2z}{c} \tag{1.5}$$

Where z is range to the target.

SFCW radar determines distance information from the phase shift in a target reflected signal. The processing of the received signal is further discussed in Section 1.3.4 below.

The SFCW radar parameters for TWI application should be chosen carefully. The main parameters are number of frequency points and unambiguous range.

Number of frequency points

SFCW radar illuminates target with consecutive train of number of frequencies and processes it coherently after receiving them. Thus the process gain will be high, if numbers of frequency points are high. The choice of high frequency points result in small frequency step size for better resolution. If the numbers of points are chosen smaller then data acquisition time is reduced.

Unambiguous range

The unambiguous range is given by

$$R_u = \frac{c}{2\Delta f} \tag{1.6}$$

From equation (1.6) if the frequency step is narrow then ambiguous range will be greater. Frequency step size Δf is also calculated as

$$\Delta f = BW/(K-1) \tag{1.7}$$

Beam width of antenna

In monostatic radar system, with synthetic aperture techniques, the beam width of single antenna should be narrow [232]. If the antenna beam is narrow it is easy to pick line of sight target signal.

(ii) *Wall parameters*

The wall through which the signal is penetrating plays an important role in detection and imaging. To ensure signal penetration through wall it is desirable to have minimum attenuation at the working frequencies. The other parameters of wall which are important to combat effects of wall such as shift in target position and blurriness in image are thickness of wall and dielectric constant. These parameters should be known before hand for processing.

(iii) *Target parameters*

Behind the wall there are two possibilities of the targets i.e., moving or stationary. Microwave signal both penetrate and get reflected off from target material. The composition and thickness of the targets are prime factors for receiving the reflected signal. If the dielectric constant of target is high then reflection will be high whereas for low dielectric, reflections are very poor. Every target has unique response to signal which will be useful for classification and recognition.

(iv) *Image parameters*

High quality images of targets with reasonable penetration capabilities are required for general TWI application. To produce high quality images, the closely spaced targets should be resolved in both down range and a cross range direction.

Down Range Resolution

Down range resolution is the capacity of the radar to discriminate individual elements that are close to each other in down range as shown in Figure 1.3 (a). High down range resolution is obtained by using wide bandwidth and is given as equation (1.8) [4].

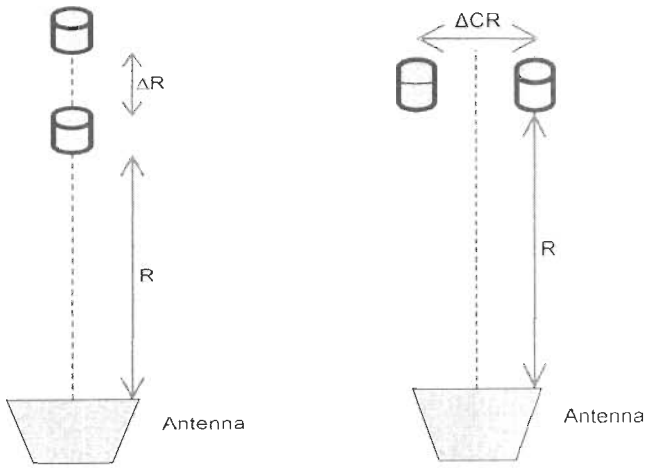

(a) (b)

Figure 1.3 Resolution (a) Range resolution (b) Cross range resolution

$$\Delta R = \frac{c}{2BW} \tag{1.8}$$

where c is speed of light and BW is operating bandwidth.

The effective bandwidth is determined by the total frequency excursion, i.e., $K \times \Delta f$.

The down range resolution of step frequency radar is given by equation (1.9)

$$\Delta R = \frac{c}{2K\Delta f} \tag{1.9}$$

where K is number of frequency points and Δf is step size.

The required bandwidth must be greater than 1 GHz to obtain range resolution in order to detect object size of few centimeters. The actual value is taken more than theoretical value.

Cross Range Resolution

Cross range resolution is the capacity of the radar to discriminate individual elements that are close to each other in cross range as shown in Figure 1.3(b).

Resolution in cross range is a function of wavelength at the lowest operating frequency, the length of physical antenna aperture and distance to target. Cross range resolution is defined as

$$\Delta CR = \frac{\lambda R}{D} \tag{1.10}$$

where λ is wavelength, R is distance to target in far field from antenna and D is physical aperture of antenna. For a real antenna, cross range resolution degrades with increasing target distance. To achieve high cross range resolution, narrow beam width is required for which the antenna aperture should be quite large which is physically unmanageable. Another approach is to introduce the concept of a fixed array or synthetic array. The idea of synthetic array is that a physical antenna moves to each point. Processing the data allows us to synthesize an effective aperture many times the size of a real aperture [91]. Thus, the distance travelled during data observation determines aperture size, limited by time required to scanning. If fixed array is used scanning time is reduced with increase in complexity of processing signals.

High frequency range is chosen at which the narrow beam width of antenna is achieved. Thus high cross range resolution requirement leads to the selection of higher frequency. But at high frequencies, penetration through the wall is low. Thus there is inherent tradeoff between resolution and penetration. Better resolution and penetration are the major challenges being faced in TWI. Various types of wall materials are used in different parts of the world like wood, asbestos, brick, concrete and so on. The characterization of common types of wall is described by [150]. The walls made of wood are approximately transparent to radar frequencies. Thus frequencies above 10 GHz can be used for imaging. On the other hand in brick wall attenuation is more. In brick wall, one way attenuation is reported as 5 dB/cm at 5 GHz and in concrete it is 10 dB/cm at 3 GHz [56].

(v) *Scanning*

Three scanning methods namely, A-scan, B-scan and C-scan were used to collect data. These are different levels of obtaining information in TWI depending on the application.

A-scan

Basic level which provides information about presence of target along with approximate location of the target is called as A-scan or range profile. But it does not indicate how many targets are present in cross range.

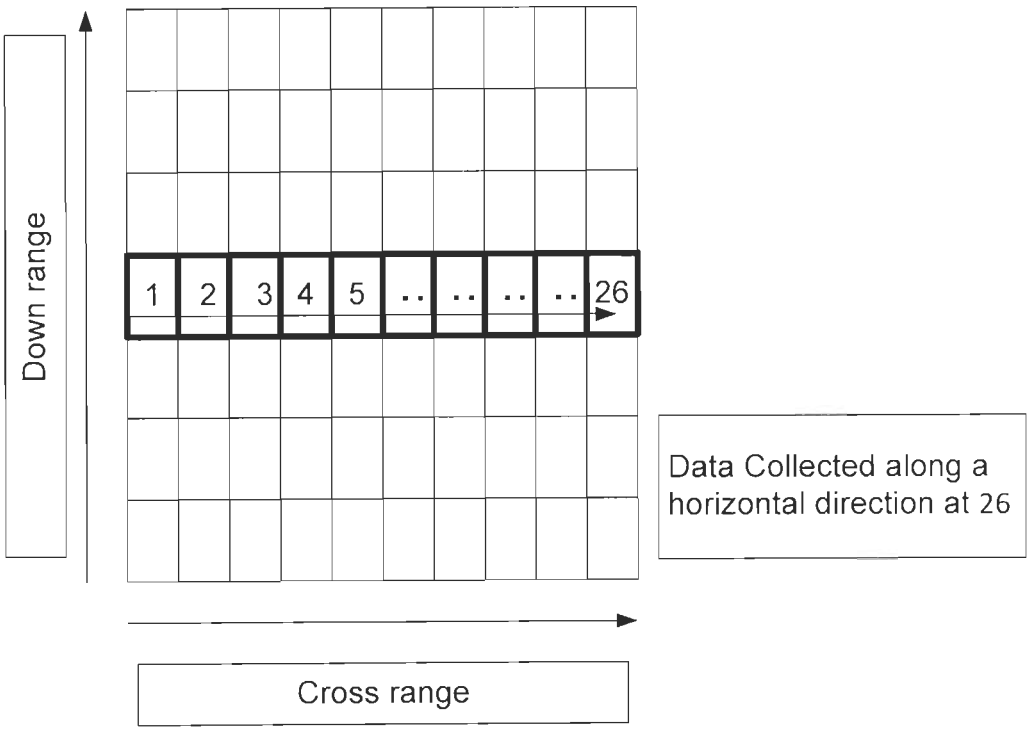

Figure 1.4 B-scan technique

B-scan

B-scan is a observation of A-scans recorded along scanning line, i.e., in monostatic case, radar transmits and received the signal and then moves to the next location and repeat operation along a predefined path in front of wall. B-scan system provides information about number of targets presents in cross range along with their exact locations.

Horizontal axis of B-scan data consists of number of antenna position marked as 1, 2, ... 26 and vertical axis is downrange distance from antenna as shown in Figure 1.4.

C-scan

C-scan (or three dimensional data presentation) data is obtained from the ensemble of B-scans, measured by repeated line scans along the plane. Accordingly 20 B-scan data (images obtained at different heights) is collected to form C-scan data as shown in Figure 1.5. In addition to range, C-scan provides valuable information about the target extent in length, width and height. Significant amount of time is required to complete the scanning.

(b) *Selection of parameter for assembling TWI system*

From these observations, selection of frequency range up to approximately 5 GHz can be used as attenuation is within acceptable range. On other hand bandwidth is chosen so as to resolve the targets in down range in tenth of centimeters.

So the selected frequency range of 3.95 GHz to 5.85 GHz with bandwidth of 1.9 GHz, number of frequency points as 4001, gives range resolution of 7.89 cm in air according to equation (1.9) and cross range resolution at 5 m distance with synthetic aperture as 1.5 m will be 20 cm at centre frequency according to equation (1.10).

1.3.2 Data collection

Observations were carried out as following,

1. Observations have been taken for single target behind plywood and brick wall
2. Observations have been taken for double target behind plywood and brick wall

All the observations have been carried out for A, B and C-scan.

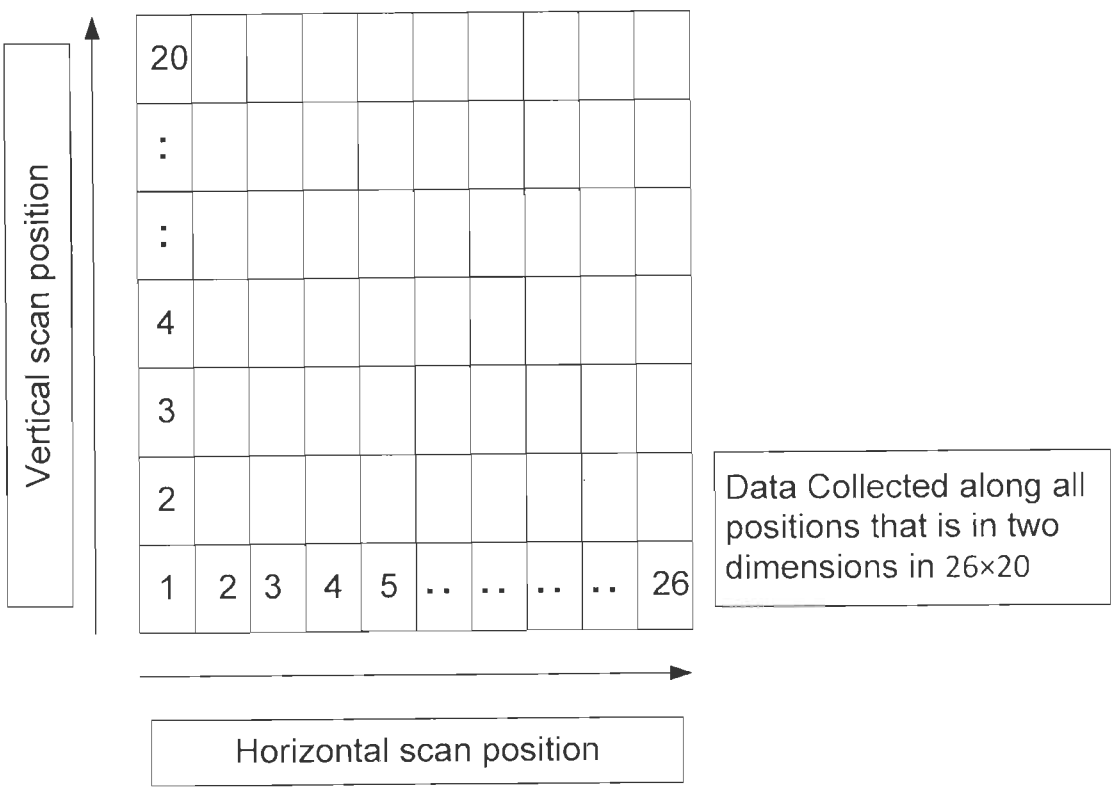

Figure 1.5 C-scan technique

(a) *Data collections for single target*

Figure 1.6 shows the experimental setup used for taking observations. TWI radar system with a single antenna is used to transmit and receive SFCW signal at one location and then is moved to next location at regular interval and same operation is repeated along the axis parallel to wall. The antenna is aimed normal to the front wall. The antenna scanner starts scanning at 0.5 m above ground and scans up to 1.5 m above ground in the regular interval. The system scans the region in two dimensions in vertical plane parallel to the wall at an interval of 5 cm along cross range and 5 cm along the height. The observations were taken for $X = 26$ antenna positions in cross range (horizontal scanning direction) and $Y = 20$ antenna positions in height (vertical scanning direction) means a matrix of 26×20 is scanned by shifting the antenna by 5 cm at each scanning point. The total number of observation points on the scanner for one target type behind wall is 520. Table 1.2 shows the measurement details with different type of walls used with single target having different shapes. The distance of the wall and target from the scanning system is different for plywood and brick walls. Details of target type, shape and dimensions are given in Table 1.2.

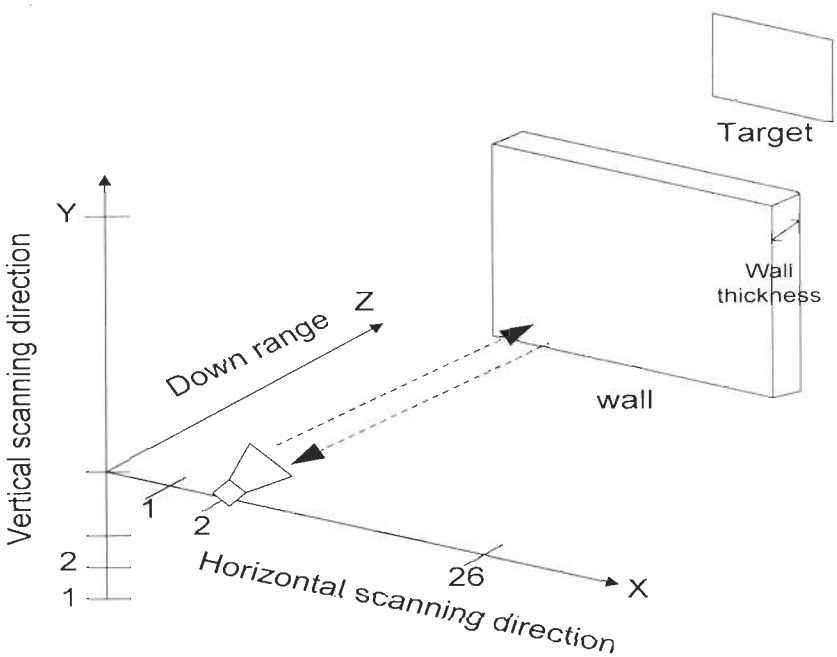

Figure 1.6 Geometrical arrangements for observations when single target is present behind wall.

Table 1.2 Data collection for single target

S. No.	Type of Wall	Type and Shape of target	Size of target	Distance between wall and antenna	Distance between wall and target
1	Plywood	Metal (Rectangle)	0.55 m× 0.60 m	1.9 m	0.3 m
2	Plywood	Metal (Circular)	0.58 m diameter	1.9 m	0.3 m
3	Plywood	Metal (Square)	0.58 m side	1.9 m	0.3 m
4	Brick	Metal (Rectangle)	0.55 m × 0.60 m	2.32 m	0.3 m
5	Brick	Metal (Circular)	0.58 m diameter	2.32 m	0.3 m

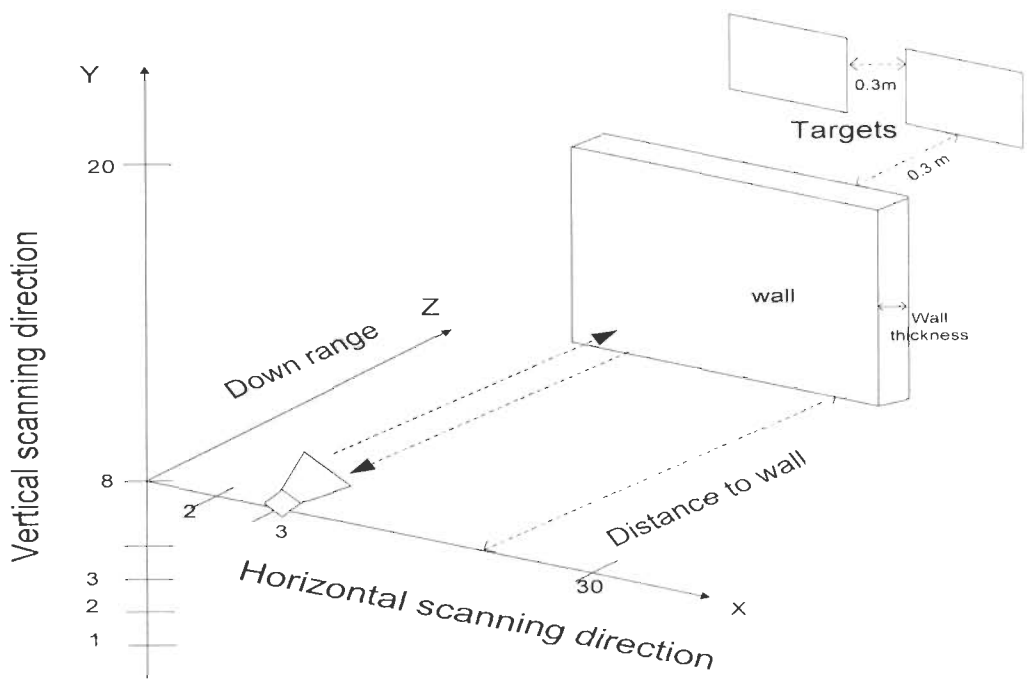

Figure 1.7 Geometrical arrangements for observations when double targets are present behind wall

(b) *Data collection for double targets*

Figure 1.7 shows the geometrical arrangement used for data observations when two targets are present behind the wall. The system scans the region in two dimensions in vertical plane parallel to the wall at an interval of 5 cm along cross range and 5 cm along the height.

Table 1.3 Data observation setting for double target

S. No	Type of wall	Target 1		Target 2		Distance between wall and antenna (m)	Distance between wall and target (m)	Distance between two targets (m)
		Type	Shape with dimension	Type	Shape with dimension			
1	Plywood	Metal	Rectangle 0.55 m × 0.60	Teflon	Square 0.58 m^2	1.90	0.3	0.3
2	Plywood	Metal	Circular 0.58 m diameter	Teflon	Circular 0.58 m diameter	1.90	0.3	0.3
3	Brick	Metal	Square 0.58 m^2	Teflon	Square 0.58 m^2	2.32	0.3	0.3
4	Brick	Metal	Circular 0.58 m diameter	Teflon	Circular 0.58 m	2.32	0.3	0.3

The scanning position is denoted as (X, Y) where X is horizontal scan position which varies from 1 to 30 and Y is vertical scan position which varies from 1 to 20. Thus the scanning length in horizontal direction is 1.5 m and 1 m in vertical scanning length. Data is collected for 600 scan points.

For 2D scanning, the number of measuring points is increased to 30 points in cross range. Metallic target plates along with the Teflon target plate with different shapes and dimensions have been taken as targets. Both targets are separated by a distance of 30 cm in cross range. The distance of the wall and targets from the scanning system for plywood and brick walls are given in Table 1.3.

1.3.3 Wall characterization

Many researchers have examined propagation through different types of wall materials [150, 134]. Although building material characteristics are available in the literature but for accurate assessment, it is necessary to know the exact parameters of wall which is used in experimentations. So, the characterization of wall is carried out using Insertion transfer method as described by Muqaibal and Safaai-Jazi, [149]. Then numerical method is applied to extract attenuation coefficient and dielectric constant of material. Wall characterization is described in following subsections.

(a) *Experimental setup and measurement for wall characterization*

Experimental setup for wall characterization is shown in Figure 1.8. It consists of VNA, transmitting and receiving antennas. Two measurements i.e., without wall (free space) and with wall present in between transmitting and receiving antennas are made. Care is taken to maintain same conditions during both measurements. The distance between transmitting and receiving antennas remain same and wall is kept exactly at the centre of both antennas. Two different wall materials, plywood and brick wall are selected for characterization. Table 1.4 shows the details of experiment which is carried out. The distance between two antennas is taken sufficiently large so that wall is in far field of each antenna. The height of antenna from ground was 1m. The transmitted power, frequency range and number of frequency points are 20 dBm, 3.95 GHz to 5.85 GHz and 201 respectively. The transmission characteristics for different wall materials in the given frequency range is observed.

Table 1.4 Details of characterization of wall

S. No.	Material	Dimension (cm) (length×width×thickness)	Distance between transmitting antenna and wall	Distance between wall and receiving antenna
1	Plywood	182.88×121.92×0.12	265 cm	265 cm
2	Brick wall	365.76×304.8×28	182 cm	182 cm

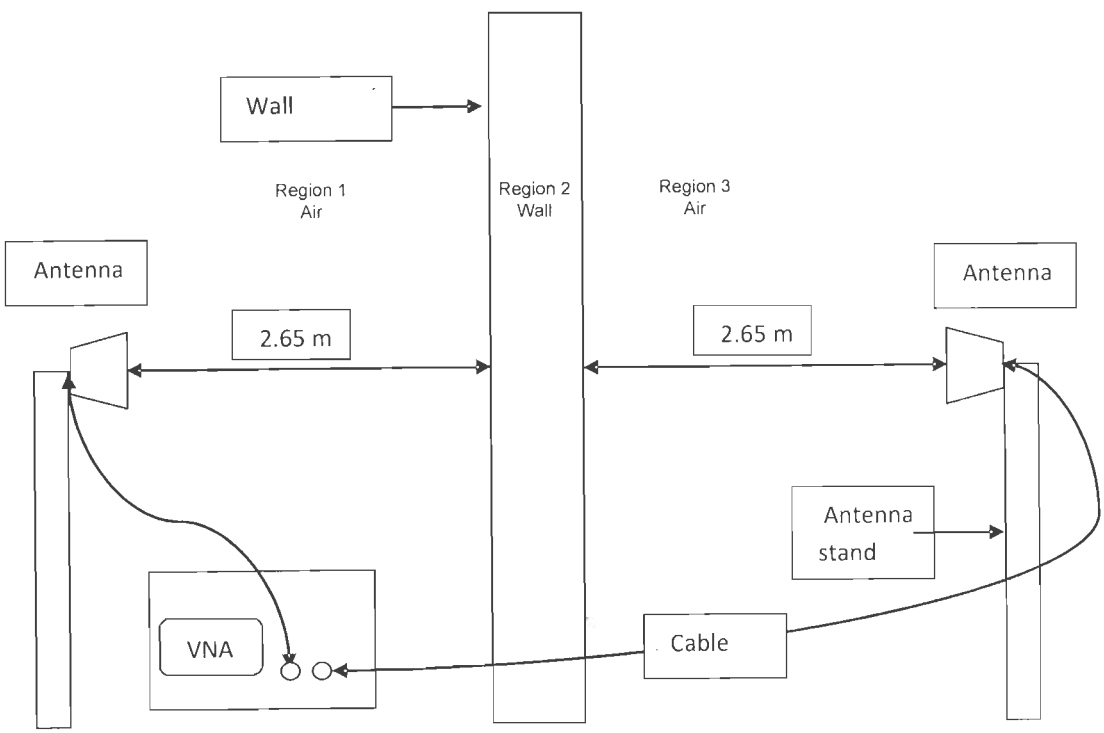

Figure 1.8 Experimental setup

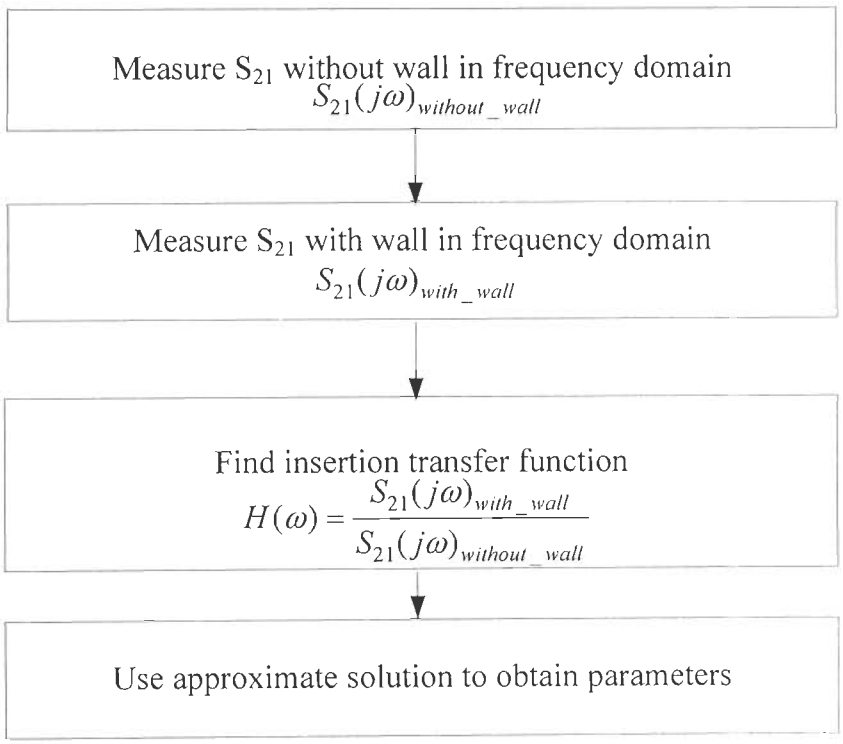

Figure 1.9 Flowchart of Wall characterization procedures

(b) *Dielectric measurements of walls*

The procedure for processing the measured data and extracting wall parameter is given in flowchart Figure 1.9. The insertion transfer function is obtained which is defined as ratio of two radiations transfer function given as

$$H(\omega) = \frac{S_{21}(j\omega)_{with\_wall}}{S_{21}(j\omega)_{without\_wall}} \tag{1.11}$$

where $S_{21}(j\omega)_{without\_wall}$ is measured in absence of wall and $S_{21}(j\omega)_{with\_wall}$ is measured in presence of wall.

A uniform plane wave is assumed to be normally incident on wall with thickness d_w as shown in Figure 1.8. The wall unknown complex dielectric constant $\varepsilon_r = \varepsilon_r' - j\varepsilon_r''$ is required to obtain. A reflected wave in region 1 (air), forward and reflected wave in region 2 (wall) and transmitted wave in region 3 (air) occurs. Applying boundary conditions for the electric and magnetic fields at the slab air interfaces, transmission coefficient can be calculated as

$$T = \frac{4}{e^{\gamma d_w}(2 + \frac{\eta_1}{\eta_2} + \frac{\eta_2}{\eta_1}) + e^{-\gamma d_w}(2 - \frac{\eta_1}{\eta_2} - \frac{\eta_2}{\eta_1})} \tag{1.12}$$

where

$$\eta_1 = \sqrt{\frac{\mu_o}{\varepsilon_o}} = 120\pi\,\Omega$$
$$\eta_2 = \sqrt{\frac{\mu}{\varepsilon_o(\varepsilon_r' - j\varepsilon_r'')}} \tag{1.13}$$

$$\gamma = \alpha + j\beta \tag{1.14}$$

$$\gamma = j\omega\sqrt{\mu o \varepsilon o(\varepsilon_r' - j\varepsilon_r'')} \tag{1.15}$$

where d_w is thickness of wall, γ is complex propagation constant, α is attenuation constant in N_p/m, β denotes the phase constant in rad/m, η_1 and η_2 are intrinsic impedance of medium 1 (air) and medium 2 (material), ω is radian frequency, ε and μ are permittivity and permeability of material respectively.

The insertion transfer function is related to transmission coefficient through

$$Te^{j\beta_o d_w} = H(j\omega) \tag{1.16}$$

where ,

$$\beta o = \frac{\omega}{c} \tag{1.17}$$

Thus

$$H(j\omega) = \frac{4e^{j\beta_o d_w}}{e^{\gamma d_w}(2 + \frac{\eta_1}{\eta_2} + \frac{\eta_2}{\eta_1}) + e^{-\gamma d_w}(2 - \frac{\eta_1}{\eta_2} - \frac{\eta_2}{\eta_1})} \tag{1.18}$$

Once the complex insertion transfer function $H(j\omega)$ is determined by measurements, equation (1.18) can be solved for complex dielectric constant [149]. In terms of scattering parameters that can be directly measured, equation (1.18) can be represented directly in following form,

$$(x+\frac{1}{x})\sinh(xP)+2\cosh(xP)-\frac{2}{S_{21}}=0 \tag{1.19}$$

where

$$x=\sqrt{\varepsilon}_{complex} \tag{1.20}$$

$$P=j\beta_o d_w \tag{1.21}$$

$$S_{21}(jw)=H(j\omega)e^{-j\omega\tau_o} \tag{1.22}$$

$$\tau_o=\frac{d_w}{c} \tag{1.23}$$

Equation (1.19) can be solved numerically by two dimensional search algorithm which may give the complex solution. The convergence of this algorithm is not always guaranteed. Thus by assuming wall to be low loss such that is $\varepsilon_r''/\varepsilon_r' << 1$, following expression is given which is now in terms of real part of dielectric i.e., ε_r':

$$\tan[\beta_o d_w - < H(j\omega)] + \frac{1-QX}{1+QX}\tan(\beta d_w)=0 \tag{1.24}$$

where

$$Q=-\left(\frac{\sqrt{\varepsilon r'}-1}{\sqrt{\varepsilon r'}+1}\right)^2 \tag{1.25}$$

and

$$x=e^{-2\alpha d}=\frac{[\cos(2\beta d_o)(\varepsilon_r'-1)^2+8\frac{\varepsilon_r'}{|H(j\omega)|^2}]-\sqrt{[\cos(2\beta d_o)(\varepsilon_r'-1)^2+8\frac{\varepsilon_r'}{|H(j\omega)|^2}]^2-(\varepsilon_r'-1)^4}}{(\sqrt{\varepsilon_r'}-1)^4} \tag{1.26}$$

Solving equation (1.24) numerically, ε_r' is obtained and attenuation can be obtained from equation (1.26) and $\varepsilon r''$ can be obtained from following expression:

$$\varepsilon_r''=\frac{2c\alpha\sqrt{\varepsilon_r'}}{\omega} \tag{1.27}$$

(c) *Results of dielectric measurements*

To observe the signal loss through wall (one way), insertion loss is calculated and given by (1.28).

$$IL = 20\log_{10}(H(j\omega)) \tag{1.28}$$

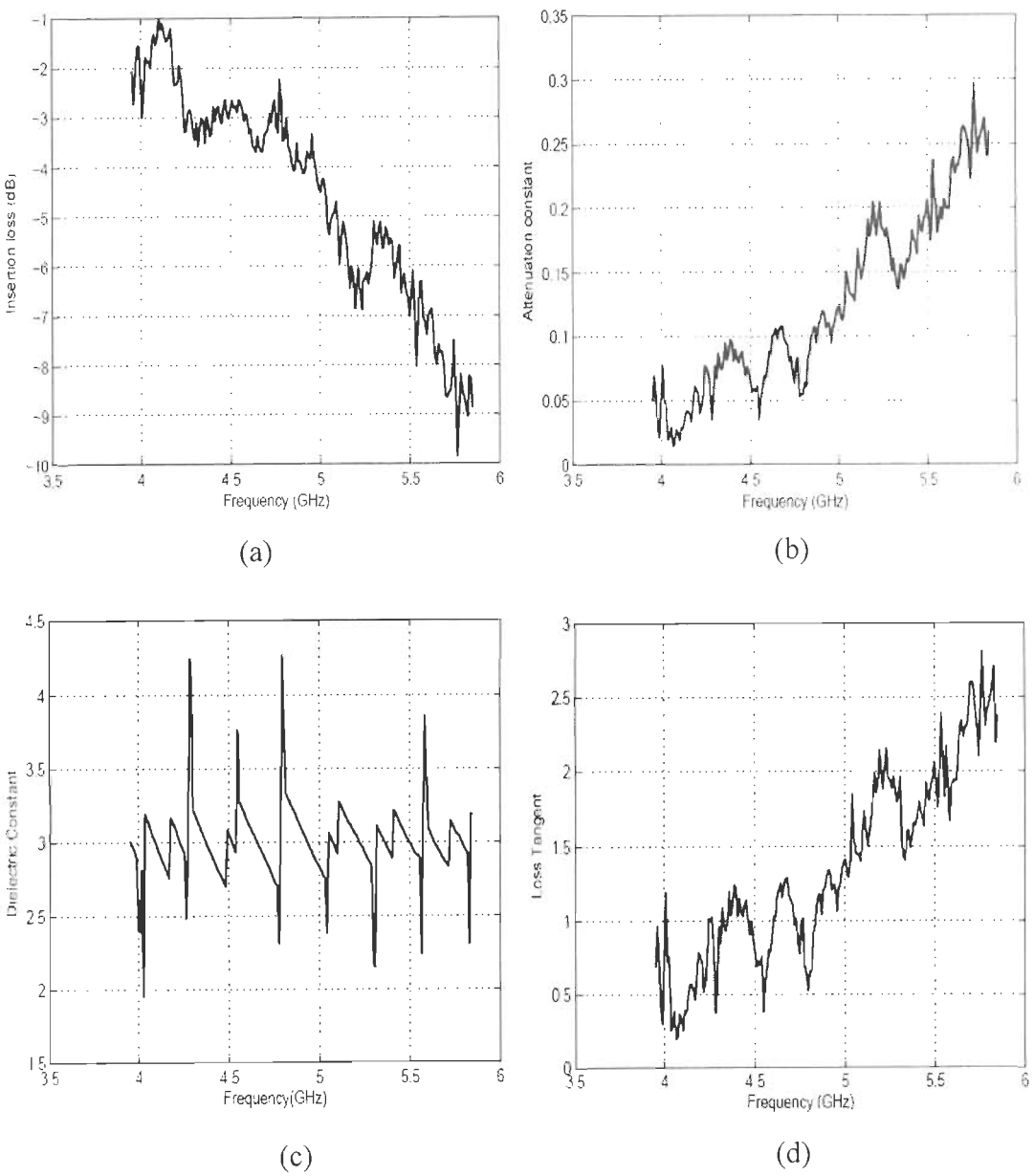

Figure 1.10 Results for brick wall (a) insertion loss versus frequency (b) Attenuation constant versus frequency (c) dielectric constant versus frequency (d) Loss tangent versus frequency

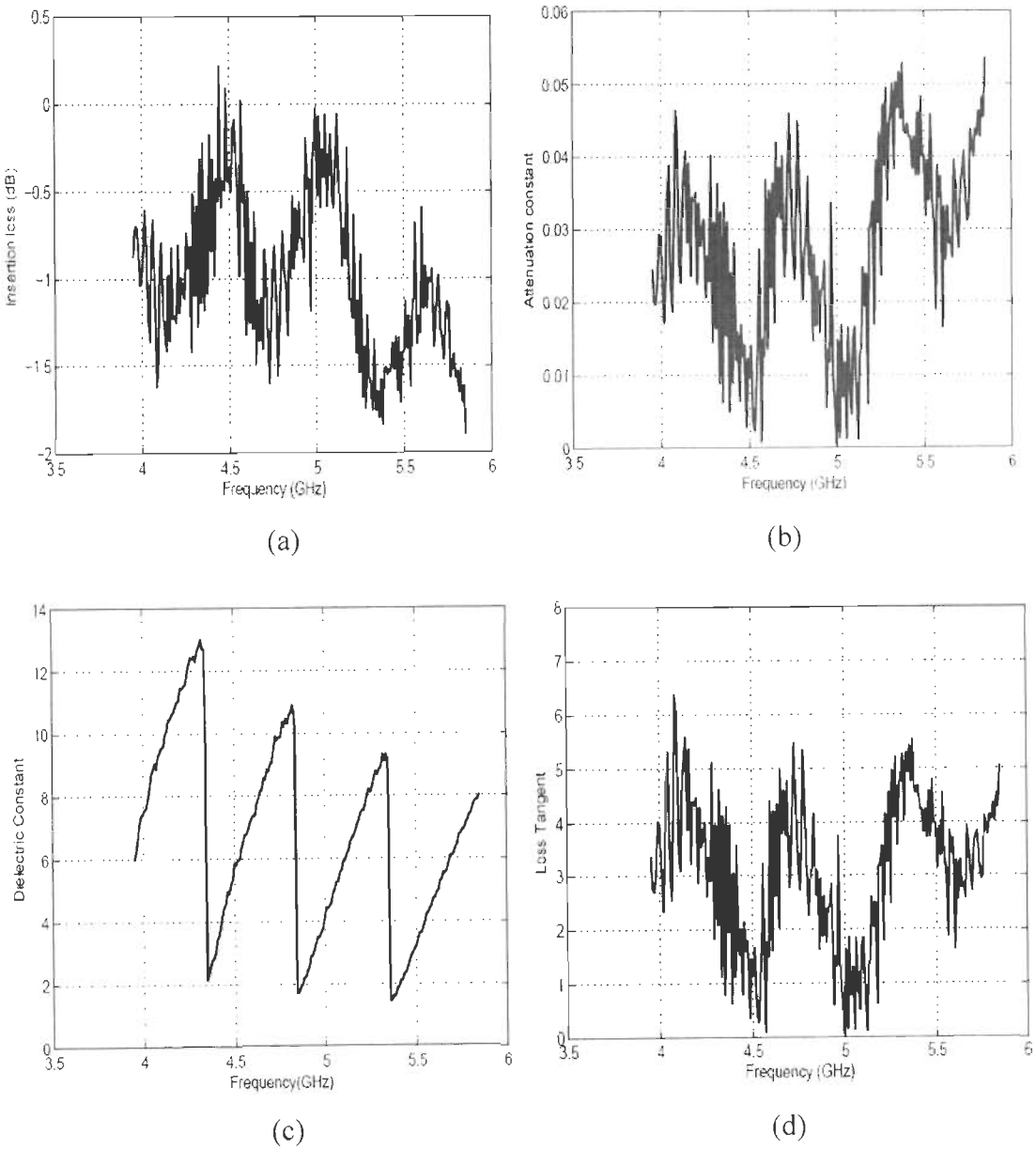

Figure 1.11 Results for plywood wall (a) Insertion loss versus frequency (b) Attenuation constant versus frequency (c) dielectric constant versus frequency (d) Loss tangent versus frequency

It is found that, lower the frequency, lesser will be wall attenuation as observed from Figure 1.10 (a) for brick wall and Figure 1.11 (a) for plywood wall. The results for attenuation constant, dielectric constant and loss tangent as observed are shown in Figure 1.10 b, 1.10 c and 1.10 d for brick wall and Figure 1.11 b, 1.11 c and 1.11 d for plywood wall. It is observed from figures that these parameters exhibit frequency dependence as expected. The average value of relative dielectric constant, in case of brick wall was 3 where as in case of plywood wall it was 5.5. This study of calculation of attenuation due to brick wall also helps to know the detection capability of radar. If wall is highly attenuating then the signal would not reach the target.

1.3.4 Pre-processing

Pre-processing step mainly consists of 1) frequency to spatial domain 2) calibration and 3) velocity correction. Before detection process, pre-processing techniques are applied. The detailed signal pre-processing steps which are used is given in flow chart as Figure 1. 12 and are described in the following subsections.

Step 1. Frequency to time domain

A-scan signal is obtained by placing an antenna at a specific position. SFCW radar generates the data in frequency domain, which may be filtered by applying a standard windowing function, such as the Hamming window [12, 85]. When the hamming window is applied, the side lobes are reduced which will help to reduce false alarm rate and will improve dynamic range of detection. But due to windowing, range resolutions deteriorate, so it is not applied here. After receiving data in frequency domain, it is converted into time domain by using Inverse Fast Fourier Transform (IFFT). The converted signal is presented as signal strength vs. time delay. The signal received at one of the antenna location after IFFT is given by Freundorfer, et. al., [58],

$$s(t) = \sum_{k=1}^{K} S(f_k)\exp(j2\pi f_k t) \tag{1.29}$$

where K is maximum number of frequency points, $S(f_k)$ is the received reflected signal in frequency domain at k^{th} frequency and t varies from 0 to $(K-1)/BW$ with step interval of $1/BW$, BW is bandwidth of the system.

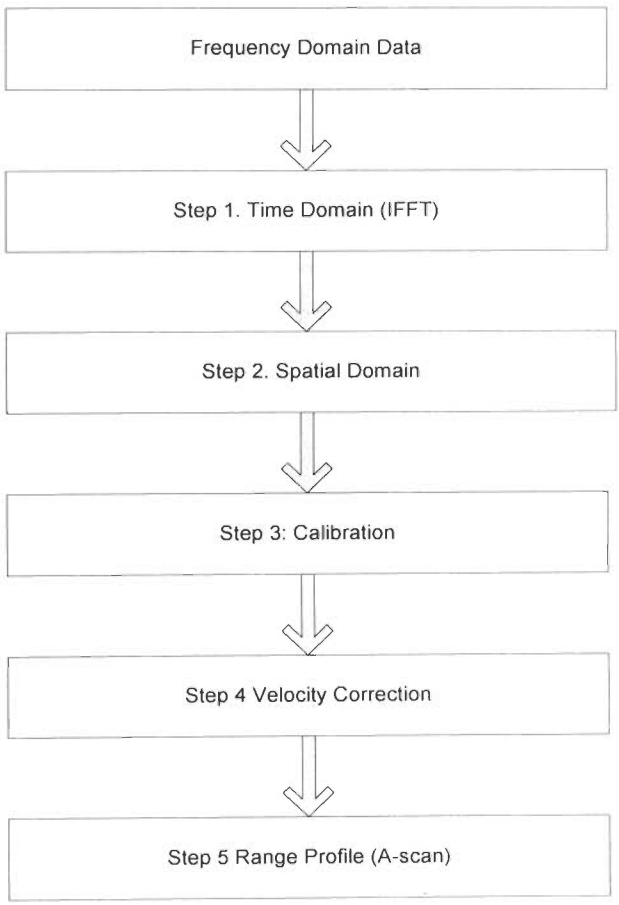

Figure 1.12 Flowchart for signal pre-processing

Step 2. Time domain to spatial domain

SFCW radar determines the distance to targets by constructing a synthetic range profile in the spatial domain. The time domain signal is converted into spatial domain also called as range profile. Range profile is one dimensional information and given by expression as

$$S(z) = \sum_{k=1}^{K} S(f_k)\exp(j2\pi f_k(2z/c)) \qquad 0 < z < z_{\max} \tag{1.30}$$

where z is down range distance given as

$$z = (c * t)/2 \tag{1.31}$$

and c is velocity of light.

The maximum distance is calculated by

$$Z_{\max} = c(K-1)/2BW \tag{1.32}$$

which is 315 m. But distance for range profile is taken as per the room dimension i.e., 5 m, by truncating data after 5 m.

Step 3. Calibration using metal sheet

TWI Radar system must be calibrated to remove systematic errors such as uneven frequency responses, the cables and the antennas. Calibration is performed by placing a large metallic plate in front of transceiver [156]. The metallic plate is kept at a known distance i.e., at the location of wall and the range profile is plotted from which delay due to antenna system is calculated. To find out the exact distance between antenna systems and wall, the delay due to antenna system is taken into account. This data can be stored and may be used for future reference. If a large metallic plate (reference) is located at a known distance of R_{ref} from antenna then one way propagation delay t_{ref} is given by (1.33)

$$t_{ref} = \frac{R_{ref}}{c} \tag{1.33}$$

But when plotted with the experimental data, the actual time at which reflection due to reference plate is observed as t_{obs} and delay is calculated by (1.34)

$$t_{delay} = t_{obs} - t_{ref} \tag{1.34}$$

The corrected range profile will be

$$s(z) = \sum_{k=1}^{K} S(f_k)\exp\{j2\pi f_k(2z/c + 2Z_{shift}/c)\} \tag{1.35}$$

where Z_{shift} is shift in distance due to t_{delay}.

Step 4. Velocity correction

Since the antenna is placed at a standoff distance from wall, the signal travel in air first, then through wall and then again in air before being reflected from target. The presence of the wall has to be accounted in processing the signal otherwise shifted target from their actual position is obtained. For determination of accurate position of target, velocity correction must be applied on received signal [7]. The delay time through walls compared to free space propagation is determined by

$$t_{wall\_delay} = \frac{D_{wall}\left(\sqrt{\varepsilon_{rwall}} - 1\right)}{c} \tag{1.36}$$

where D_{wall} is thickness of wall and ε_{rwall} is dielectric constant of wall. The corrected range profile after calibration and velocity correction is given by (1.37)

$$s(z) = \sum_{k=1}^{K} S(f_k)\exp\{j2\pi f_k(2z/c + 2z_{shift}/c + 2D_{wall}(\sqrt{\varepsilon_{rwall}} - 1)/c)\} \tag{1.37}$$

It is assumed that the emitted signal and received signal propagates in perpendicular direction with respect to wall and multiple reflections are neglected.

(a) *Implementation of flow chart Figure 1.1*

Results obtained at different stages of pre-processing technique are described in this section. Two different types of data have been selected for analysis. First data from Table 1.2, S. No. 1 is taken in which plywood wall is used and second data from Table 1.2, S. No. 4 is taken in which brick wall is used. Results obtained for single target made-up of metal that is kept behind plywood wall is discussed first and then for brick wall.

(i) *Implementation of Preprocessing for target behind Plywood wall*: Figure 1.13 shows the normalized A-scan plotted at different steps of flow chart Figure 1.12. Normalization is defined as:

$$E_{normalization} = \frac{E - E_{\min}}{E_{\max} - E_{\min}} \tag{1.38}$$

where, E is the prescribed data value and E_{min} and E_{max} are minimum and maximum data values of the range profile respectively. A-scan or Range profiles are observed for presence and absence of target at different scanning locations.

When the target is absent behind wall only two significant peaks p_1 and p_2 are observed as shown in Figure 1.13 (a) with red dashed line. When the target is present in front of scanner, three peaks due to different scatterers are observed in the range profile as shown in Figure 1.13 (b) with blue solid line. The first peak marked as p_1 is due to weak isolation between transmitting and receiving port of antenna system, second peak marked as p_2 is due to plywood wall and third peak marked as p_3 is due to target. It is observed that the target position is different from the actual distance taken in measurements. Distance from antenna scanning system to plywood is 1.9 m and from wall 0.3 m. The total distance from scanner to target is approximately 2.212 m.

As shown in Figure 1.13 (b) the wall is observed at 2.368 m and the target is observed at approximately 2.684 m from the scanning system in raw range profile plotted at step 2. Calibration and velocity correction as described in Section 1.6.1 is applied. After applying calibration (step 3) and velocity correction (step 4) the target position is shifted towards actual value. In case of plywood wall, range profile as shown in Figure 1.13 (c) represents raw range profile that is before calibration (red dashed line) and range profile after calibration (blue solid line). Then applying velocity correction, position of target is observed at 2.211m which is nearly equal to original position. Figure 1.13 (d) represents range profile before and after velocity correction. Since the thickness of plywood wall is very small (0.012 m) the change in distance due to velocity correction is negligible. It infers that shift in target distance by 0.473 m is mainly corrected by calibration.

(ii) *Implementation of preprocessing for target behind brick wall*: In case of brick wall, when the target is absent behind wall only three peaks p_1, p_2 and p_3 are observed as shown in Figure 1.14 (a) with red dashed line. The first peak marked as p_1 is due to weak isolation between transmitting and receiving port of antenna system, second

peak marked as p_2 is due to front side of wall, third peak marked as p_3 is due to other side of brick wall. When the target is present, four peaks are observed in the raw range profile (step 2) as shown in Figure 1.14 (b) with blue solid line, the fourth peak being marked as p_4 is due to target. It is noted that, position of the target from the scanning system is different for the brick wall. Distance from antenna scanning system to brick wall is 2.32 m and the target is approximately 2.9 m away from the antenna scanning system (Table 1.2, sr. no. 4).

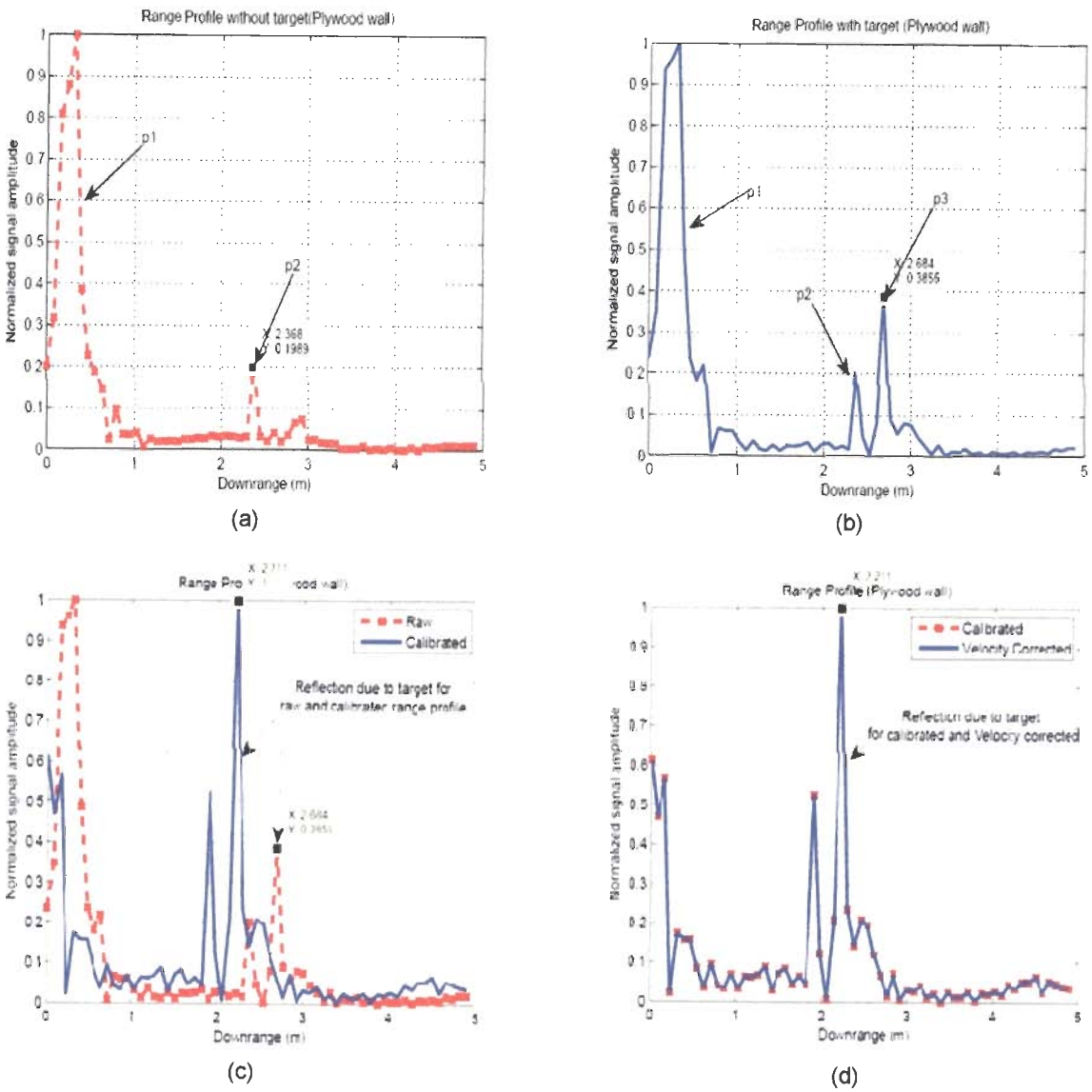

Figure 1.13 (a) Raw range profile with target at step 2 (b) Raw range profile without target at step 2 (c) Range profiles before and after calibration (step 3) (d) Range profile before and after velocity correction (step 4)

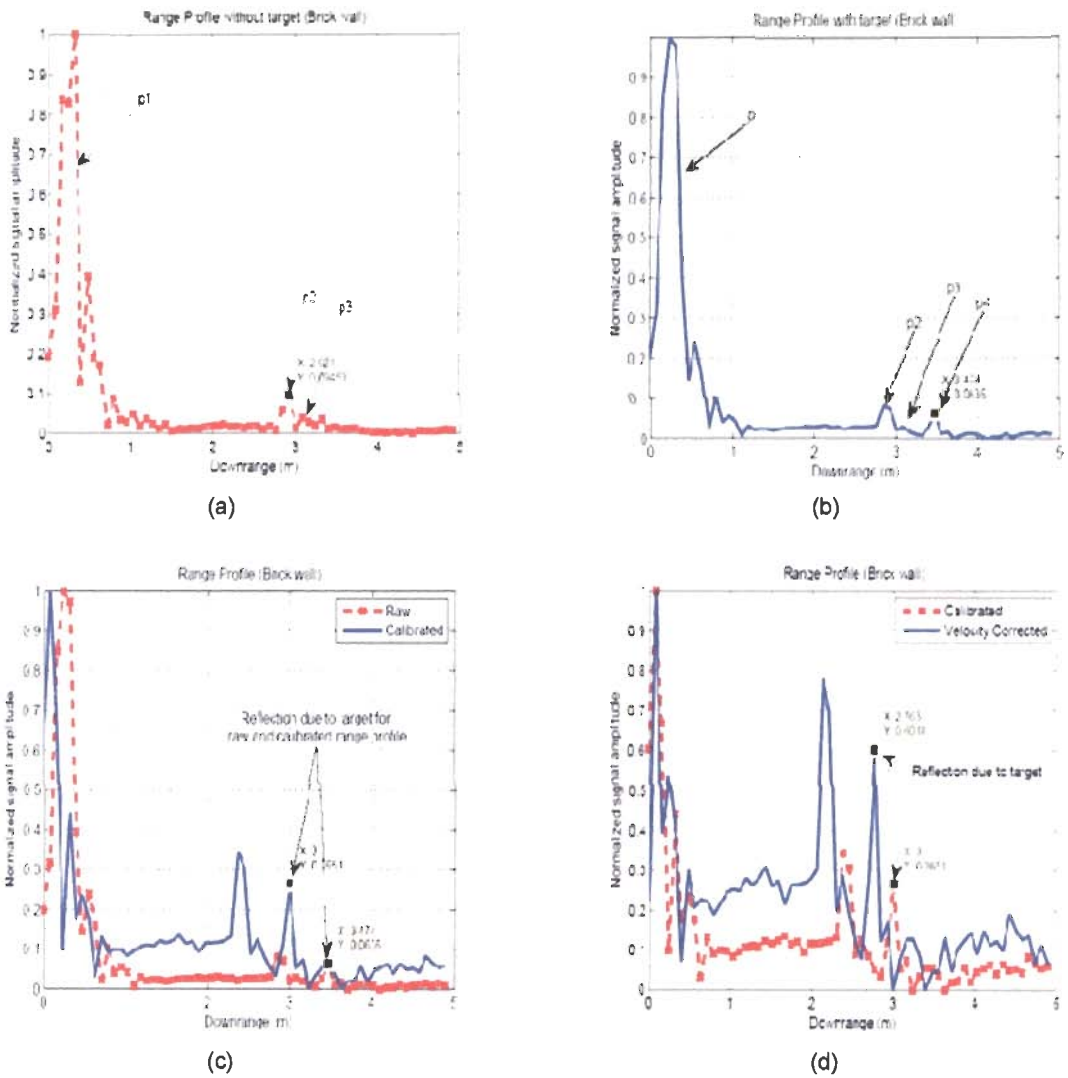

Figure 1.14 (a) Raw range profile without target at step 2 (b) Raw range profile with target at step 2 (c) Range profile before and after calibration (step 3) (d) Range profile before and after velocity correction (step 4)

It is observed from Figure 1.14 (b), range profile plotted at step 2, that the target position is 3.47 m which is greater than actual distance. To obtain the correct position of target behind brick wall, corrections are applied as described in flowchart Figure 1.12. Observing range profile before and after calibration (step 3) from Figure 1.14 (c), the target is observed at approximately 3 m from the scanning system. Figure 1.14

(d) represents range profile after velocity corrections (step 4) on calibrated range profile. The target is now observed at 2.76 m which is quite near to actual position of target. The error in range measurement is by an amount equal to range resolution value that is 0.0789 m. It is observed that signal gets attenuated more in brick wall as compared to plywood wall. A weaker reflection from target is observed in case of brick wall compared to plywood wall as expected.

1.4 Organization of the thesis

The organization of thesis work is as following. In Chapter 2, the existing techniques and methods for TWI system are briefly reviewed. The chapter addresses the development in techniques for improving detection, imaging and classification of targets. Study and critical analysis of various clutter reduction techniques and its implementation on obtained data are presented in Chapter 3.

Chapter 4 critically discusses the statistical based thresholding approach for target detection and probability distribution function based target classification. The focus is to classify metal and low dielectric targets behind the wall.

The objective of Chapter 5 is to study and apply some of the existing imaging focusing algorithms like back projection, frequency wave number (ω-k) and delay sum techniques for obtaining the image. The objective of Chapter 6 is divided into two parts; first part is C–scan imaging for target detection and second part consists of feature extraction and shape recognition using neural network. The summary of contributions made in the thesis and future scope of work is presented in Chapter 7.

Chapter 2

Brief review of literature

2.1 Introduction

Ferris and Currie presented a state of the art for TWI system in 1998 and expected that advancement will take place in next ten years [54]. Till today the research in TWI focuses on the areas of transceiver design, electromagnetic aspects, signal processing, detection, imaging, classification and identification of targets [14, 51, 154, 223, 241, 242, 243]. It is also a point of research to design high bandwidth antenna with reasonable gain for various imaging applications [31, 32, 67, 68, 78, 79, 80, 81, 82, 95, 145, 182, 193].

Different technologies like pulse, FMCW, SFCW and UWB random noise that are used in communication can be used in TWI system [18, 28, 42, 48, 61, 134, 153, 202, 221, 234]. Nowadays researchers are using new approach of compressive sensing in SFCW to get better resolution by reducing the amount of collected samples [83, 88, 96, 211]. Several radars have been built and tested experimentally for TWI applications [62, 64, 76, 169, 214, 228]. Selection of frequency range is one of the

important parameter in radar. Selection of higher frequencies allows large bandwidth at the expense of reduction in penetration capability. So selection should be done carefully. The researchers have used different frequency ranges for radar. Allan Hunt [91] has chosen 500 MHz to 2 GHz, Soldovieri et al. [202] worked in frequency range of 0.8 GHz to 4 GHz, Ahmad et al. [6] have worked in the range of 1 to 12.4 GHz and Dehmollaian and Sarabandi [42] have worked in the range of 1 to 3 GHz.

Fine range resolution is obtained due to wide bandwidth. One dimensional information is known as A-scan that only provides range information. Due to fine resolution, multiple targets in down range can be easily separated and discriminated. To achieve fine cross range resolution, either array or synthetic aperture radar imaging concept is used. To emulate a large aperture by moving single antenna in monostatic mode called as B-scan and is discussed in Figure 1.4 chapter 1. A coherent summation of data collected over a path will form a high resolution image known as two dimensional or B-scan image which is useful to know exact location of target and targets lateral dimension. C-scanning system provides extra information to B-scan images i.e height (Figure 1.5 chapter 1). The image obtained from C-scanning is 3 dimensional.

Developments in TWI are primarily motivated due to application of ground penetrating radar (GPR) techniques to TWI system. The review of TWI is quite exhaustive. So only selected areas given below are considered for review:

- Processing of received signal to remove clutter and to improve target signal strength
- Detection of target and classification
- Imaging algorithm
- Shape recognition

2.2 Brief review of work related to clutter reduction

A common problem for every radar system is the appearance of clutter in the received signal. Clutters are undesired component in the received signal i.e., those signals that are unrelated to the target scattering characteristics but occur in the same sample time window and have similar spectral characteristics to the target signatures. In TWI, received signal consists of desired response of target along with addition of other

signals arising mainly from radar system parameters, wall reflections, environment of room and multiple reflections. Radar system must be calibrated to remove systematic errors such as uneven frequency responses due to cables and antennas. Calibration is an important aspect for any radar system [35]. In satellite SAR images radiometric calibration is to be done [116, 133, 144, 212] but for TWI system external calibration has to be carefully carried out. Since the reflected signal from target is small compared to other reflected signals, the detection of targets become difficult. To improve the quality of detection and reduce false alarm, signal to clutter ratio must be increased. For optimal target recognition, clutter removed signal is very helpful. Researchers have developed various clutter reduction techniques to enhance the detection accuracy and reduce false target detection [1, 36, 101, 102, 107, 128, 141, 158, 175, 252].

In general, clutter reduction techniques are classified into two methods, classical technique and statistical method. Potin et al. [175] used classical digital filter technique to attenuate the surface reflections from ground. One of the main methods from this category is classical clutter reduction algorithm (CCRA) [36,102]. The difficulty with this technique is that the coefficients are not optimized to represent noise and target. Zoubir et al. [252] explored different signal processing techniques with emphasis on Kalman filter based approach to detect the target. The drawback of Kalman filter is that it is computationally intensive.

A parametric clutter suppression method is proposed by Merve et al. [141], which models the variations in received signal. The drawback of this method is that a reference signature of target is required which is not always available practically. Ho et al. [86] computed linear prediction coefficients adaptively. But the problem in this method is that it makes the assumption of Gaussian noise for the prediction error which is not yet proven. Other clutter removal approaches based on statistics are given by Xu et al. [227]. The difficulty with this technique is lack of robust estimate of these statistics. Non statistical approach that extract response of landmine from noisy radar was proposed by Lopera et al. [128]. Karlsen et al. [101] decompose GPR data into clutter and target signal using Principle Component Analysis (PCA) and Independent Component Analysis (ICA) techniques. Abuzarad et al. [2] have used Singular Value Decomposition (SVD) and Factor Analysis technique along with PCA and ICA, to decomposed GPR data into clutter and target. Verma et al. [217] have

applied statistical clutter reduction techniques like SVD, PCA, FA and ICA on TWI images obtained when plywood wall is used. It is found that metal target got detected easily after applying clutter reduction techniques. Comparison is done among these techniques by obtaining signal to clutter ratio and it is found that ICA techniques gives highest signal to clutter ratio. But when low dielectric target such as Teflon is used then only ICA is able to detect target. Similar results are obtained when plywood wall is replaced by brick wall to increase the complexity of detection of low dielectric target [60].

One of the commonly used methods for clutter reduction in TWI relies on background subtraction, where two images taken with and without target are subtracted [240]. But this technique has a drawback because clutter remains present if the data is not collected at exactly the same antenna positions in both cases. In addition, it is not possible in real scenarios to collect data without target. Polarization difference imaging can be used to reduce wall reflections [243]. Time gating is another method used to reduce clutter [4]. It is successful for targets which are far away from wall but for targets near to wall the target response overlaps in time domain and cannot be separated in time. Recently a spatial filter based clutter reduction technique is developed in which zero spatial frequency which represents wall reflections is notched from the image [245]. This filter may subtract low frequency components of target as well. This method removes reflections from wall but does not discuss about reduction in reflections due to other non target objects (clutters). There exists a need for further study to explore suitable clutter reduction techniques which can be applied successfully for detecting the target behind wall with reduced false alarm.

2.3 Review of work related to detection and classification

2.3.1 Detection

In TWI, with several indoor objects of different material and shapes, robust detection and classification is an important area of concern to the end users. The key issue of any microwave based sensor for target detection is probability of detection and false alarm rate [24]. The performance of a TWI radar system as a detector is governed by radar cross section of target, its distance from radar, propagation properties of wall

and performances of radar. Daniel [36] presented effect of frequency on probability of detection and it is observed that as frequency increases, probability of detection decreases. However, when the comparison of radar images at 1 GHz and 2 GHz over the area and depth range was carried out, it was observed that at higher frequency, spatial information from images increased [205].

Carvevic, D. [23], proposed an algorithm based on wavelet packet decomposition for detection of shallowly buried targets. Wavelet decomposition has been found to be useful since it provides a flexible representation of the signal by selectively matching its time, scale and frequency characteristics. However, wavelet packet decomposition is not invariant to time shifts of the signal which affect the performance of detectors.

In TWI, detection is possible due to dielectric contrasts between two different kinds of targets or between target and media. If contrast is very weak then detection becomes difficult. The electromagnetic waves transmitted by the radar propagate through air, non metallic wall and other objects. TWI radar detects any object that lie in its line of sight if the conductivity of object or dielectric constant or permeability is different from the surrounding medium. Since change in absorption mainly affects absorption so it is usually the contrast in the permittivity that leads to a reflection of the electromagnetic waves radiated by the transmit antenna. Metal target will reflect more energy and appear bright while target having low dielectric constant will reflect less energy and appear dark. Bright area will indicate presence of target while dark area will not be detected. One of the important aspects in radar is to detect the target with low dielectric constant because the radar reflection from the low dielectric constant target is very weak and reflection from low dielectric target in presence of clutter will be very difficult to be distinguished. Impulse radar used to detect buried non-metallic targets was addressed by Brunzell [20]. One of the major problems with GPR is strong back scattered signal from ground surface. If the object is buried deeply below the surface then there is no problem since back scattered signal from surface will arrive earlier than the target signal and using time gating reflection from ground surface can be removed. But when the objects are shallowly buried time gating is not possible since backscattered signal from surface and target will arrive almost simultaneously. Brunzell [20] presented spatial filter based algorithms that separate weak target signal from strong ground backscattered signal.

Another technique to detect low contrast was described by Paik et al. [164] in which review of various mine detection techniques with emphasis on image processing methods like filtering, enhancement and feature extraction was described. Problem of detection of target due to low contrast is solved by morphological contrast enhancement technique and histogram equalization method. For automatic segmentation techniques using statistical features and regional properties, B-scan images are used to train neural network to distinguish targets from non targets [192]. Real aperture FMCW radar was developed by Yamaguchi et al. [233] for detection of objects buried in heavily wet snowpack. In this, synthetic aperture technique for imaging was not used, i.e., non-coherent B-scan images were obtained for detection of target. SAR images obtained in different applications use various detection techniques but in TWI system detection needs more attention [3, 11, 30, 33, 38, 103, 110, 207].

Barrie [15] carried out a preliminary study on using ultra wide band synthetic aperture for through the wall detection with focus on detection of human body without considering wall effect on detection. For target detection simple data processing technique is used to extract the data pertaining to reflected fields by target. Bistatic SFCW based radar with two step strategy was proposed [9, 47, 130, 131, 188]. The first step is detection and localization and second step is imaging of objects using linearized microwave tomography algorithm.

Clutter removal is not sufficient to improve detection of targets as quite good amount of unwanted signal still exists. So for minimizing the unwanted signal after clutter removal, thresholding technique may be applied. Several thresholding algorithms have been proposed for computing the optimum threshold level in order to discriminate between targets and background [63]. Statistical analysis of ground clutter data has been done to design optimum detection algorithm by Billingsley et al. [17] in which best fit has been obtained as Weibull model. Similarly statistical modeling of radar backscattering from sea surface was done by Greco et al., [75]. Detection of target in Weibull clutter was described [71, 191]. Raghavan [178] proposed a method for estimating the parameters of k-distributed clutter when the available sample size or the data is limited.

Detection of target based on principles of classical detection theory using Neyman-Pearson criterion to derive probability of detection and false alarm has been done [41]. In this method, statistics of radar image was examined to obtain probability

density functions for modelling background noise and target returns. The method based on statistical binary hypothesis testing in which background model is defined and all other objects which significantly deviate from this model are detected as targets. Similar study based on Neyman–Pearson criterion, detection of target was presented by Lai et al. [112], with a difference that hypothesis is obtained after applying auto correlation.

A simple method to detect change in TWI scenario was presented by Soldovieri [203, 204]. If access to different sides of structure is possible then fusion of multi view TWI radar images can generate single image. Fusion of images from multiple locations improves the probability of detection. Ahmad et al. [5] have presented multiplicative combining and RCS based direct thresholding scheme for fusing of TWI images obtained from multiple vantage points along two sides of structure under consideration. Debes et al. [39] found that fused images obtained using wideband through the wall synthetic aperture beamforming have high signal strength and improvement in false target detection compared to individual images. Papson and Narayanan [168] also presented fusion strategies for multiple location SAR and ISAR images.

Target detection based on analysis of the polarization characteristics was described by Yamaguchi and Moriyama [231, 235] where polarimetric synthetic aperture FMCW radar was used to detect buried objects in actual snowpack. Discussion about polarimetric filtering principle that uses characteristics polarization states to discriminate two targets is given [77]. Method based on high order statistical features has been used to discriminate between landmine targets and the background [192]. Matched filters are commonly used for detection of known targets in presence of clutter [46]. Landmine detection is done using different techniques like derivative feature extraction [59], and Radon Transforms [209]. Automatic detection of targets based on Hough transform was proposed for GPR applications. Statistical signal processing techniques have also been used to localize target [227]. The goal is to discriminate target from clutter using Bayesian approach and Hough transform [209]. Hough transform was used in Lidar [125]. Different techniques are available in literature [45, 54, 70, 74, 93, 100, 108, 109, 110, 122, 123, 126, 127, 135, 140, 152, 160, 163, 165, 166, 167, 176, 180, 181, 198, 199, 200, 213]. Thresholding becomes difficult when target and background level possess substantially overlapping

distribution. Thus thresholding technique needs further investigation from TWI point of view.

2.3.2 Classification of targets

Classification of radar data can be done in three ways; electromagnetic analysis, time spectral analysis and spatial analysis. Aim of classification technique is to extract more information with minimum *apriori* information. Some of the techniques which have been developed to classify targets based on these techniques are reviewed. Discrimination of mine target based on estimation of dielectric constant has been investigated by Spagnolini [208]. Some researchers have used Polarimetric SAR for classification purpose [37, 231]. Use of polarimetric SAR images enhances the classification accuracy but these methods require more observation vectors.

Mine features extracted using time spectral analysis was described by Merwe and Gupta, [141]. The other techniques for extracting features of mine are Karhunen Loeve Transformation (KLT) and Kittler Young Transformation (KYT) [164].Preliminary work in TWI on target classification was reported by Debes et al. [40], and Mobasseri and Rosenbaum [143]. Matched illumination based detection and classification of objects was considered by Estephan, et al. [49] in which optimized waveform was designed that maximizes probability of correct target classification. A scheme in which after segmentation, feature extraction using superquadrics and classification using nearest neighbor and Support vector machines has been used was presented by [143]. Quite less work has been reported in classification of targets used in TWI system. Therefore there is a need to give more attention which can address these problems.

2.4 Review of work related to imaging

Imaging methods for TWI system receive wide attention. Many imaging algorithms have been developed for TWI system. One of the challenges in TWI is that the microwave signal should be able to penetrate through wall with relatively little attenuation so that reconstruction algorithm should be able to give maximum information about target. Moreover the fine resolution of imaging should be obtained. Reconstruction or image formation can be coherent or non coherent. Non coherent

imaging is based on envelope of signal and does not include phase information whereas coherent techniques are based on complex signal amplitude. Non coherent systems can be useful for localization of target using trilateration techniques [4]. Coherent imaging provides high resolution images. Various imaging techniques are described by several researchers [6, 16, 27, 90, 117, 120, 151, 250]. TWI radar based on pulse signals was introduced in which back projection technique was used for image formation [151]. Hunt [90] has applied back projection technique for image formation for SFCW based radar system. The blending of ultra wide band short pulse radar and synthetic aperture radar (SAR) processing for TWI application was described by Barrie [15]. The broadband content of a radiated pulse provides fine range resolution, while synthetic processing enhances cross range resolution. Zetik et al. [248] presented modified cross correlated back projection algorithm and demonstrated with numerical examples that image quality was improved without increasing computational complexity compared to back projection.

Delay sum algorithm for image formation approach along with synthetic aperture radar technique was presented by Ahmad et al. [6]. Dehmollaian and Sarabandi [43] proposed differential SAR based imaging technique. Researchers have used polarimetry as a tool for monitoring earth surface with SAR images [26, 98, 99, 136, 174, 177, 230]. Techniques of tomography have been developed for TWI applications which were originally used in medical imaging [155]. Soldovieri and Solimene, [202] proposed linear inversion algorithm in which only qualitative information about target like location and geometrical features were obtained and not the quantitative information like dielectric constant and conductivity of target.

Unprocessed B-scan image exhibits undesired hyperbola and therefore have low resolution features. To solve these problems various migration techniques have been developed and applied to focus the scattered energy at their true spatial location in object space. Several migration algorithms to focus the reflection signatures back to their true positions have been reported in the literatures. Ozdemir et al. [161] have applied hyperbolic summation (HS) type focusing technique to remove distortion from hyperbolic dispersion in B-scan GPR images. Focused GPR images were obtained for experimental data. There is a need to adopt this technique to inhomogeneous, lossy and anisotropic mediums. Also the applicability is limited for single target detection.

Morrow and Genderen [147] described techniques to sense low dielectric contrast object using integration method. Significant improvement in detection performance and image contrast was obtained by combining this technique with cross polarimetric images. The algorithm and techniques developed are thought suitable for standalone ground penetrating radar system. Morrow [148] addressed problem in near field detection like direct antenna coupling, air/ground coupling receiver noise floor and degradation in dynamic range due to which loss of target signal, range resolution and range accuracy may occur. Due to improvement in signal magnitude, range resolution and range accuracy, even objects with low dielectric contrast were detected. The results confirmed that it was possible to effectively image a range of buried metallic and dielectric objects either individually or clustered. The deficiency in HS was that some unwanted defocusing effects were generated especially when two or more buried objects are close to each other.

The survey of focusing algorithms namely hyperbolic summation, and frequency wave number (ω-k) was given by Ozdemir et al. [160, 167]. The proposed techniques enhances lateral resolution of B-scan GPR images. It was observed that performances of both techniques were different when same scene was imaged. It was observed that ω-k methods focus the target signatures better than HS method [160]. Yigit et al. [244] presented frequency domain based imaging algorithm to obtain well focused GPR images. Because of similarity of data collection scheme between GPR and TWI, synthetic aperture radar (SAR) based focusing technique could also be applied on TWI data. These techniques could be analyzed further to decide most appropriate technique for TWI applications. Targets of interest are generally easier to be recognized and isolate on three dimensional data sets than on conventional two dimensional images. For example, 3D images help in discrimination between targets having different dimensions [19, 69, 84, 111, 194, 195, 247].

Imaging faces a challenge due to the presence of wall. The propagating wave slows down, encounters refraction and is attenuated as it passes through the wall. The composition and thickness of wall, its dielectric constant and the angles of incidence affect the characteristics of signal propagating through the wall. In image formation techniques, if propagation effects are not included in the process, then the propagation distortions due to signals passing through walls will create ambiguities in imaging the

scene. Study of wave propagation through wall at microwave frequencies is useful [13, 44, 87, 115, 172, 184, 236].

The effects of incorrect estimates of the wall thickness and dielectric constant on performance of imaging have been investigated [7, 104, 119, 246]. A technique which can remove ambiguities in wall parameter was proposed [219, 220]. The approach obtains two images at two standoff distances from wall. For different values of wall thickness and dielectric constant target position is shifted. The wall parameters corresponding to the intersection point of target image trajectories for two standoff distances provide target exact positions. Study on wall parameter ambiguities was presented by Ahmad et al. [7]. Image quality metrics were used to obtain focus images. Another study of wall effects on imaging was carried out by Dehmollaian and Sarabandi [42]. Sensitivity analysis was carried out to study the effect of wall in particular degradation in imaging.

The information on electromagnetic properties like dielectric constant and loss tangent of building materials was presented [149, 183]. In TWI, severe multipath effects are incurred. Due to multipath effect the incorrect target location will be detected. It will also cause single target to be detected in multiple locations. If in front of imaging object, undesired object is placed then due to shadow, faithful representation will not be possible. The internal wall structure also has a large impact on the propagated signal. A hollow portion in the wall will affect the propagation through the wall. The propagation effects can be corrected using image focusing techniques to perform proper signal correction. Propagation diffraction and multipath have been partially addressed [113, 206, 218, 251].

Burkholder and Browne [21] proposed techniques in which low coherence features were suppressed by using coherence factor filtering which increases clarity and uniformity. TWI image obtained through back projection were quantified using coherence factor to check the wall effect. Coherence factor can be used for correction in wall parameters to improve focused image. In satellite SAR images for contrast enhancement different techniques were used [72, 73, 215, 216, 229, 237, 238, 239].

2.5 Review of work related to shape recognition

The purpose of obtaining images is to provide target information to end user/operator. Essential information is extracted from targets which is used for recognition. The design of recognition system requires careful attention to following issues, definition of pattern classes sensing environment, pattern representation, feature extraction and selection, cluster analysis, classifier design and learning, selection of training and test samples and performance evaluation. Review papers summarize and compare some of the well known methods used in various stages of pattern recognition system [94]. Pasolli et al, [170] proposed a novel pattern recognition system to identify and classify buried objects. The complete process consisted of preprocessing, thresholding, search of hyperbolic pattern and finally recognition of material type of identified objects using support vector machine (SVM). Moriyama et al, [146] discuss the classification of targets buried underground by radar polarimetry. Two techniques, one based on power polarization anisotropy coefficient and other based on polarimetric signature were used for classification.

Yarovoy et al. [242] used frequency spectrum analysis to detect human respiration. Falconer [50] measured the power spectral density of a variety of objects and used the difference in the shaping of the power spectral density (PSD) to differentiate between targets and infer the activity level of human targets. Spectrogram based features for identification of human being was proposed by Gurbaz [83]. Al-Nuaimy et al, [10] proposed a technique in which neural network was used to identify target reflection from radar image using Welch power spectral density and Hough transform was then applied as pattern recognition.

Recent research has addressed the topic of time-frequency and Doppler signature estimation for target classification and identification [173, 179]. Time-frequency algorithms are only able to estimate linear and stationary signal. GPR target detection and discrimination using time frequency features was described by Savelyev et al. [190]. Wigner distribution was used as a target signature due to its good properties. The other conventional time frequency analysis techniques include short time Fourier transform (STFT), wavelet analysis [114, 141]. A new target recognition technique based on adaptive joint time frequency such as adaptive Gaussian processing was proposed by Kim et al. [106]. GPR landmine discrimination based on deconvolution

algorithm was proposed by [189]. Frigui et al. [59] used edge histogram descriptors for feature extraction of landmine targets. In through wall radar, human activity behind wall was detected [112, 157]. Hilbert Huang transform was only able to analyze non-liner and non-stationary signals. Anthony [86] investigated the classification and identification of different objects behind wall. The different materials are defined based on their permittivity, permeability and conductivity and include concrete, wood, glass and, metal. Many methods decompose the transient signal into a sum of decaying sinusoids. These sinusoids were represented by their poles and residues. Detailed analysis of the poles and residues was then carried out with the aim of classifying them based on material medium of the object. Classification of received signal was carried out by studying pole patterns obtained by using Prony's method.

Due to presence of wall, imaging algorithm which uses C-scan data to generate images are not clear from point of view of target recognition. Thus the user or operator will face the problem of proper interpretation of image. C-scan images are highly subjected to degradation due to the fact that antenna beam is not focused. In post processing filtering, interpolation, thresholding and edge detection techniques were applied to enhance the detection and visualization [192]. Column filtering techniques smoothen the transitions from one pixel to another in the image. Automatic recognition of target by shape will be very useful in TWI to discriminate between different targets.

To enable reliable recognition of targets, the essential information must be extracted from the obtained image [225]. In order to recognize target shapes, first order and second order statistics such as mean, standard deviation, entropy and many others were proposed as features by Mahfouz et al. [138]. Previous work on target recognition in TWI was based on micro-Doppler effect [112]. Mobassori and Rosenbaum used PCA for object recognition [143]. But the features were not position invariant. Pattern recognition technique can be used to identify and classify targets [132, 170]. In the literature related to TWI, very few researchers have mentioned about recognizing shape of object [121]. So shape detection techniques used in other application area were searched. Mahtre et al. [139] describes several shapes determination techniques. Different techniques like chain code based string feature, Fourier descriptors, region based features and moment based descriptor are used for

shape description. The complete study and comparison between Fourier descriptors and curvature scale space descriptors is described by Zhang et al. [249]. Less work has been reported on pattern recognition based recognition of objects for TWI.

Chapter 3

Critical analysis of clutter reduction techniques for detection of metallic as well as low dielectric material behind wall

3.1 Introduction

The electromagnetic waves that are transmitted by TWI system have to propagate through air, wall and other objects present in room. So, TWI radar should have capability to detect any object that lie in its line of sight. It is usually the contrast in the permittivity that leads to a reflection of the electromagnetic waves radiated by the transmitting antenna and helps in detection process. The reflected signal also depends on ratio between size of object and wavelength of signal.

The signal received from TWI system as described in Section 1.3.1 consists of addition of reflected signal from target with other undesired signals arising mainly

from TWI system parameters i.e. improper isolation between receiving and transmitting port, wall reflections and multiple reflections. The undesired components (i.e. unwanted signal) in the received signal are considered as clutter. The large energy of reflection from wall that occurs due to high contrast between the dielectric constant of wall and air leaves very small amount of energy to pass through the wall. The signal which passes through wall will be reflected from target and again passes through wall to reach the receiver. Very weak target signal will be observed in the received signal. Further, if the target dielectric constant value is comparable to medium (i.e. low dielectric constant target), then the weak target signal may get obscured due to strong clutter. The presence of high clutter level leads to unacceptably large number of false alarms. Thus, the challenge in TWI is to detect the weak target signal in presence of heavy clutter. To increase the detection accuracy of target and reduce false target detection it is therefore necessary to reduce clutter.

Various clutter reduction techniques are used to increase the target signal to clutter ratio. Mainly statistical clutter reduction techniques have been applied in ground penetrating radar (GPR) applications successfully by various researchers [36, 141, 227, 252]. Researchers working in TWI have developed various clutter reduction techniques to enhance the detection accuracy and reduce false target detection [4, 43, 240, 245]. The review of different clutter reduction techniques like back ground subtraction, time gating or spatial filtering etc. are described in Chapter 2. The drawbacks of each technique have been discussed. So clutter reduction is still a challenging task.

The main aim of this chapter is to find suitable clutter reduction technique by which target information may be enhanced. From statistical category mainly Singular Value Decomposition (SVD), Principle Component Analysis (PCA), Factor analysis (FA) and Independent Component Analysis (ICA) clutter reduction techniques have been chosen. Researchers are using various clutter removal techniques in ground penetrating radar (GPR) data but in TWI, importance of these techniques is yet to be explored.

This chapter is organized as follows. Section 3.2 describes brief description of methodology used for obtaining B-scan images. In this section different statistical clutter reduction techniques are described. In Section 3.3, the results are illustrated for metal target behind plywood and brick wall. Detection of low dielectric constant

target behind wall is described in Section 3.4. Concluding remarks are finally reported in Section 3.5 of the chapter.

3.2 Methodology

The clutter reduction techniques are applied on raw B-scan image. Figure 3.1 gives the flowchart which describes steps used to obtain clutter reduced B-scan images. According to flowchart Figure 3.1, following procedure is followed to obtain clutter reduced B-scan image.

- Formation of raw B-scan image (after step 6 from flowchart)
- Clutter reduction techniques

3.2.1 Formation of raw B-scan image

Before raw B-scan image is obtained, the pre-processing technique as described in Section 1.3.4 (Figure 1.12) is applied. Technique as described by Yamaguchi et al. [232] is used to form raw B-scan image from the B-scan data. The method of collection of B-scan data is described in Section 1.3.1. In short, in this technique for monostatic case, a single antenna is used to transmit and receive the radar signal at one location and then moved to the next location in horizontal direction to collect radar signal. Thus information at more than one A-Scan positions is collected. This set of A-Scans can thus be assembled together in a two dimensional structure, and visualized as an image known as raw B-scan image. Raw B-scan can be represented by (3.1)

$$I(z,x) = \sum_{k=1}^{K} S(f_k)\exp(j2\pi f_k(2z/c + 2z_{shift}/c + 2D_{inwall}(\sqrt{\varepsilon_{rwall}} - 1)/c)) \tag{3.1}$$

where z is distance (down range) and x is the antenna scanning positions in horizontal direction.

This raw B-scan image taken represents down range (corresponding to distance) versus intensity on the plane of scanned width (corresponding to the direction of antenna scan). On the obtained raw image, different statstical clutter reduction techniques are applied as described in the following section.

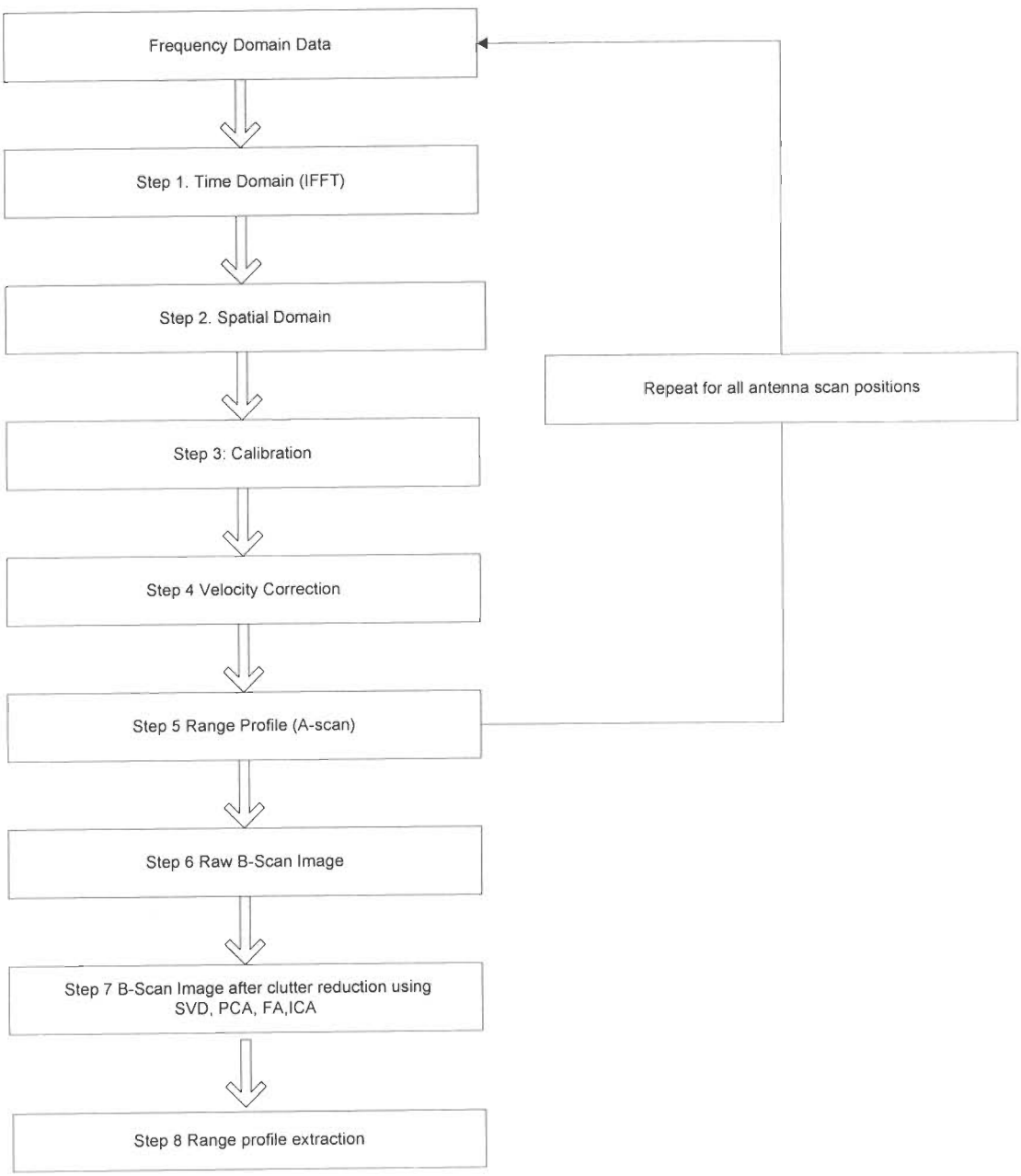

Figure 3.1 Flowchart for clutter reduction

3.2.2 Clutter reduction techniques

In statistical method data is decomposed into suitable subspace components that contain desired target response and clutter. From signal processing point of view, the techniques used for clutter reduction are called blind source or signal separation (BSS) methods [22]. BSS means separation of a set of signals called source signals from their mixture signals without acquaintance of any information (or very little information) about mixing background and signals. BSS is the separation of a set of signal in which the regularity between the signals is minimized (correlation is minimized) or the regularity between the signals is maximized (statistical independence is maximized).

In TWI system, it is assumed that the scattered response is composed of superposition of responses from individual scatterers i.e. linear model of superposition is assumed. Thus mainly two components are assumed. One is clutter and second is reflection from desired target. Using clutter reduction techniques, signal can be decomposed into desired target and clutter. Numerous statistical clutter reduction techniques exist for ground penetrating radar (GPR) but its application on TWI is yet to be explored. In this chapter Singular Value Decomposition (SVD), Principle Component Analysis (PCA), Factor Analysis (FA) and Independent Component Analysis (ICA) are applied due to ease of implementation on TWI data. Brief descriptions of these techniques are given in following subsections.

(a) *Singular Value Decomposition (SVD)*

The purpose of signal processing techniques in clutter reduction is to separate data into complementary subspaces called target signal and clutter subspaces in order to increase target signal to clutter ratio [1]. SVD is one of the most stable and computationally effective techniques in linear algebra.

B-scan image is represented by equation (3.1) whose dimension is $M \times N$ ($z = 1, 2, ..., M$; $x = 1, 2, ..., N$) where z denotes the distance index (down range) and x denotes the antenna position index (cross range). The number of discrete distance points is greater than antenna position index, therefore $M \geq N$ will be assumed. The SVD of raw B-scan image represented by equation 3.1 is given as:

$$I = USV^T \tag{3.2}$$

where U and V are ($M \times M$) and ($N \times N$) unitary matrices respectively, S = diag (σ_1, σ_2,..., σ_r) and σ_i are singular values with order $\sigma_1 \geq \sigma_2 \geq ... \geq \sigma_r \geq 0$. The columns of U and V are called left and right singular vectors respectively. Basically U and V are eigenvectors of $\{II^T\}$ and $\{I^TI\}$. For (r = N < M), the SVD is given by (3.3-3.5)

$$I = \sigma_1 \begin{pmatrix} \vdots \\ u_1 \\ \vdots \end{pmatrix} \left(\cdots v_1^T \cdots \right) + \sigma_2 \begin{pmatrix} \vdots \\ u_2 \\ \vdots \end{pmatrix} \left(\cdots v_2^T \cdots \right) + \cdots + \sigma_N \begin{pmatrix} \vdots \\ u_N \\ \vdots \end{pmatrix} \left(\cdots v_N^T \cdots \right) \tag{3.3}$$

$$I = \sum_{i=1}^{N} \sigma_i u_i v_i^T \tag{3.4}$$

$$I = I_1 + I_2 + I_3 + ... + I_N \tag{3.5}$$

where I_i are matrices of same dimensions as I and are called as modes or i^{th} eigenimage of I. After applying SVD on experimental data and analyzing all the Eigen images, it is found that first Eigen image provides clutter information and second Eigen image provides target information. The remaining Eigen images are discarded.

Thus I can be decomposed into two subspace, target and clutter respectively.

$$I = I_{target} + I_{clutter} \tag{3.6}$$

Thus clutter can be directly estimated by (3.7) and target by (3.8).

$$I_{clutter} = I_1 = \sigma_1 \times u_1 \times v_1^T \tag{3.7}$$

$$I_{target} = I_2 = \sigma_2 \times u_2 \times v_2^T \tag{3.8}$$

(b) *Principle Component Analysis (PCA)*

PCA has proven to be an exceedingly popular technique for signal processing, data compressing, data visualization and pattern recognition and is discussed at length in most of the texts on multivariate analysis. The advantage of PCA over SVD is that PCA performs better when signal strength is weak [101]. PCA is second order

statistical method in which covariance between observed variables are used for estimation. The goal is to express data set in terms of linear combinations of small set of factors that are assumed to be uncorrelated and gaussianly distributed. The first principle component accounts for variability in data as much as possible and each succeeding component accounts for the remaining variability as much as possible. Principle component techniques have been applied to GPR data analysis for detection of landmines by Karlsen et al. [101].

In TWI, for clutter reduction using PCA, B-scan data is represented by a matrix I, whose dimensions are $M \times N$ (z = 1, 2, ..., M ; x= 1, 2, ..., N). Here z denotes the distance index (down range) and x denotes the antenna position index (cross range). The K Principal components ($K< N$) of data matrix I can be given by (3.9).

$$Y = A^T I \tag{3.9}$$

where I is the zero-mean input data matrix, Y is the output matrix called the vector of principal components (PCs), and A is an $N \times K$ matrix that transforms I into Y. PCA expresses input data variables into smaller number of uncorrelated linear combination of a set of zero mean random variables while retaining as much of the information from the original variables as possible. PCA assumes that A is an orthonormal matrix ($A_i^T.A_j=\delta_{ij}$) such that the covariance matrix of Y, C_y is diagonalized. A can be computed using covariance matrix. Let I be the data matrix after normalization. Then covariance matrix C_x of I is given by (3.10).

$$C_x = \frac{1}{N} II^T \tag{3.10}$$

The Eigen vector and Eigen value matrices of C_x are Φ and Λ respectively and can be computed by (3.11).

$$C_x \Phi = \Phi \Lambda \tag{3.11}$$

Here Λ= diag (λ_1, λ_2, λ_3, ...,λ_K) and λ_1, λ_2, λ_3, ...,λ_K are the Eigen values. After arranging Eigen values in decreasing order, $\lambda_1 \geq \lambda_2 \geq \lambda_3 \geq \ldots \geq \lambda_K$ the matrix of K leading Eigen vectors A is given by (3.12).

$$A = [\Phi_1, \Phi_2, \Phi_3, \ldots \Phi_K] \tag{3.12}$$

Thus PCA can be used to detect target and reduce clutter by selecting components that mainly carry target information say A_p. Rest components represent clutter. The principle component matrix S can be given by (3.13).

$$S = A^T I \tag{3.13}$$

The reconstructed clutter free signal space can be extracted from the raw B-scan matrix containing target and clutter information. After calculating principle components, target can be extracted by second column of transformation matrix A that is A_2 and principle components matrix S that is S_2 and given by (3.14).

$$I_{target} = A_2^T S_2 \tag{3.14}$$

(c) *Factor Analysis (FA)*

The main application of Factor Analysis is to reduce data variables and to classify them accordingly. Basically Factor Analysis extracts set of factors from data set using correlation. These extracted factors are orthogonal and are ordered according to the proportion of the variance of original data [29, 226]. Therefore only a subset of factors is considered as relevant and remaining factors are considered either irrelevant or clutter.

For clutter reduction, B-scan data is represented by a matrix I, whose dimensions are $M \times N$, (z = 1,2,...,M ; x =1,2,..., N). Here z denotes the distance index (down range) and x denotes the antenna position index (cross range). The observed variables are modeled as linear combinations of the factors plus error terms.

$$I_z = \sum_{x=1}^{N} a_{zx} s_x + e_z \tag{3.15}$$

In the matrix notation it can be written by (3.16).

$$I = AS + E \tag{3.16}$$

where I is the matrix consisting of M A-scans in each row with x time samples, S is the $K \times N$ matrix of factor scores (latent variables), A is the $M \times K$ matrix of factor loading, and E is a matrix of error terms. The Factor Analysis can be modeled in terms of variances and covariances given by (3.17).

$$\Sigma = A \Phi A^T + \Psi \tag{3.17}$$

where Σ is the $M \times M$ population covariance matrix of the observed variables, Φ is the $K \times K$ covariance matrix of the factors and Ψ is the $M \times M$ residual covariance matrix.

The primary assumption is that factors are uncorrelated which implies that covariance matrix should be identity matrix i.e. $\Phi = I$, and the M-dimensional e is distributed according to K $(0; \Psi)$, where Ψ is diagonal matrix. The assumption of diagonality of Ψ implies that observed variables are conditionally independent (given the factors). The distribution of observed variable x must have zero mean and covariance Σ.

Factor Analysis finds optimal A and Ψ which best describe the covariance structure of x. The best model of A and Ψ can be found using Expectation Maximization (EM) algorithm. The EM algorithm is a two step iterative procedure for maximizing the log likelihood. A brief explanation of generalized EM algorithm for maximum likelihood method is discussed in this paper. Detailed explanation of EM algorithm for maximum likelihood Factor analysis is given by Rubin and Thayer [186].

In expectation step, it calculates the expected value of log likelihood function with respect to unknown variable z that is given as (3.18).

$$Q\left(Y \middle| Y^{(T)}\right) = E_{z|x,Y^{(T)}}\left[log\, L\left(Y|X,Z\right)\right] \tag{3.18}$$

where Y is the unknown parameter to be estimated under the conditional distribution of Z when X is given, $L(Y|X,Z)$ is the likelihood function.

Maximization step finds the optimal parameter values that maximize the expectation which is computed in Expectation step given by (3.19).

$$Y^{(T+1)} = arg\,\max_{Y}\left\{Q\left(Y\middle|Y^{(T)}\right)\right\} \tag{3.19}$$

Apply these two steps iteratively until a converged solution for Y is obtained. After applying FA on experimental data; it is found that it splits data matrix X into factor score matrix S and factor loading matrix A given by (3.16). Target can be extracted by selecting the factor score and factor loadings components which carry the target information given by (3.20). Generally the second column of A and S give the information of target and first column give the information of clutter.

$$I_{target} = A_2^{\,T} S_2 \tag{3.20}$$

(d) *Independent Component Analysis (ICA)*

ICA is used to solve blind source separation problem. ICA divides data into statistically independent components while other techniques such as Principal component Analysis (PCA) or Factor Analysis represents data into uncorrelated components. Therefore PCA or FA cannot separate signals efficiently because uncorrelatedness is not enough. Statistical independence is necessary which takes into consideration higher order moments which is a stronger statistical property than decorrelation. Therefore ICA is widely used in many applications such as feature extraction and noise reduction from the images, finding hidden factors from financial data and mostly used in telecommunications for separating the original source signal from interfering signals [1, 34, 92, 101].

Let us consider a B-scan data to be represented by a matrix I, whose dimensions are $M \times N$, ($z = 1, 2, ..., M$; $x = 1, 2, ..., N$). Where z denote the distance index (down range) and x denotes the antenna position index (cross range).

ICA assumes that every I is a linear combination of each s_x as follows:

$$I_x = \sum_{j=1}^{N} a_{ij} s_j \tag{3.21}$$

j= 1, 2, 3, … , N or in the matrix notation

$$I = AS \tag{3.22}$$

where A is an $M \times N$ basis transformation or mixing matrix, and S is the matrix holding the N independent source signals in rows of N samples. ICA of matrix I can be found by finding a full rank separating matrix W such that output signal Matrix can be defined by $Y=WI$. The estimation of source signal can be done using equation:

$$\hat{s}_j = y_j = \sum_{i=1}^{N} w_{ji} I_i \tag{3.23}$$

j= 1, 2, 3,……,N or in the matrix notation

$$\hat{S} = Y = WI \tag{3.24}$$

where W is an $N \times M$ matrix which makes the outputs from $\hat{S}$ from the linear transformation of the dependent sensor signals I as independent as possible.

Formulation of ICA can be done in two steps, first one is to formulate a contrast function $G(y)$ that estimates the level of statistical independence between the components of y and second is optimization of contrast function that enables the calculation of independent components. Contrast function estimates the level of statistical independence between the components of y means optimization of contrast function provide the independent components. To apply ICA some preprocessing is needed. The most basic preprocessing is "centering" in which mean is subtracted from each range profile in B-scan matrix I. Second preprocessing is whitening in which observed vector X is transform into new vector $\tilde{I}$ which is white means its components are un-correlated and their variance equal unity.

FASTICA [92] algorithm is used which is fixed point iteration based algorithm that calculates the separating matrix W by finding a maximum of non Gaussianity of $W^T I$. After computing separating matrix W, mixing matrix A can be computed by taking inverse of it i.e. $A = W^{-1}$. Since mixing matrix is known, corresponding independent component S matrix can be calculated using (3.22).

After applying ICA on experimental data; the number of independent components is as much as the number of A-scans obtained. By considering each row of independent component matrix S and column of mixing matrix A; images have been generated using (3.22) and observed. Image that contains target information can be chosen and rests are discarded.

$$I_{target} = A_{target} S_{target} \tag{3.25}$$

3.3 Results and discussion

Clutter reduction techniques as discussed in above section are applied to the experimental data and the resultant images have been compared. Only B-scan data at one of the height at which target is present is taken for analysis in all the cases. Signal to noise ratio (SNR) can be given as ratio of average energy of image matrix after clutter reduction to the average energy of clutter matrix. The denominator clutter term is obtained by subtracting the clutter reduced image from raw B-scan image. The final image after applying clutter reduction is supposed to have information only about target but actually it is not. Therefore, in the numerator term average energy of image giving target information is not taken as this contributes more to the numerator term of SNR and makes it difficult to compare different clutter reduction techniques. Thus peak signal to noise ratio [222] is calculated by taking the numerator term of SNR as the peak value of normalized image matrix. It infers that PSNR may be used as a first hand indicator to compare the results of various clutter reduction techniques. PSNR can be calculated using (3.26) and (3.27).

$$PSNR(dB) = 10\log\{1/MSE\} \tag{3.26}$$

$$MSE = \frac{1}{M \times N} \sum_{i=1}^{N} \sum_{j=1}^{M} \{g(i,j) - f(i,j)\}^2 \quad (3.27)$$

where $g(i, j)$ is the original B-scan image; $f(I, j)$ is the image after clutter reduction; MSE is mean square error; M and N are dimensions of image.

3.3.1 Clutter reduction for single target behind wall

(a) *For plywood wall*

Experiment was carried out for detection of a metal plate kept behind a plywood wall. The data collected as described in Table 1.2, S. No. 1 is used for analysis. The processing steps as shown in Figure 3.1 are applied to obtain clutter reduced B-scan image. Calibration and velocity correction (step 3 and step 4) as already explained in Section 1.3.4, are applied before B-scan image is obtained. Figure 3.2 (a) shows the B-scan image formed at step 6 of Figure 3.1. The vertical axis corresponds to down range distance and horizontal axis represents the scanned width (cross range) which is number of A-scans. Here, one B-scan image consists of 26 A-scans. In the B-scan image shown in Figure 3.2, a strong reflection marked as p_1 which may be due to isolation problem between transmitting and receiving ports is observed. The reflection is constant along horizontal scanning line. Similar constant reflection p_2 along horizontal scanning line is observed due to presence of plywood wall. Reflection due to target is observed and marked as p_3. Since target length is smaller than scanning length, reflection due to target is not observed throughout the horizontal line. Thus, the reflection p_1 and p_2 may be called as unwanted signal i.e. clutter.

Then the clutter reduction techniques as discuss above are applied on obtained raw B-scan image. Results obtained at step 7 i.e., after applying clutter reduction techniques like SVD, PCA, FA and ICA are shown in Figure 3.2 (b), (c), (d) and (e) respectively. From these results, it is observed that clutter is suppressed in one hand and in other hand reflection due to target is enhanced. The image obtained after applying clutter reduction is supposed to have mainly information about the target but actually it is not and contains good amount of background noise. Thus signal to noise ratio of final image i.e. after clutter reduction with different techniques has been computed to compare the results and the effectiveness of individual clutter reduction techniques is seen.

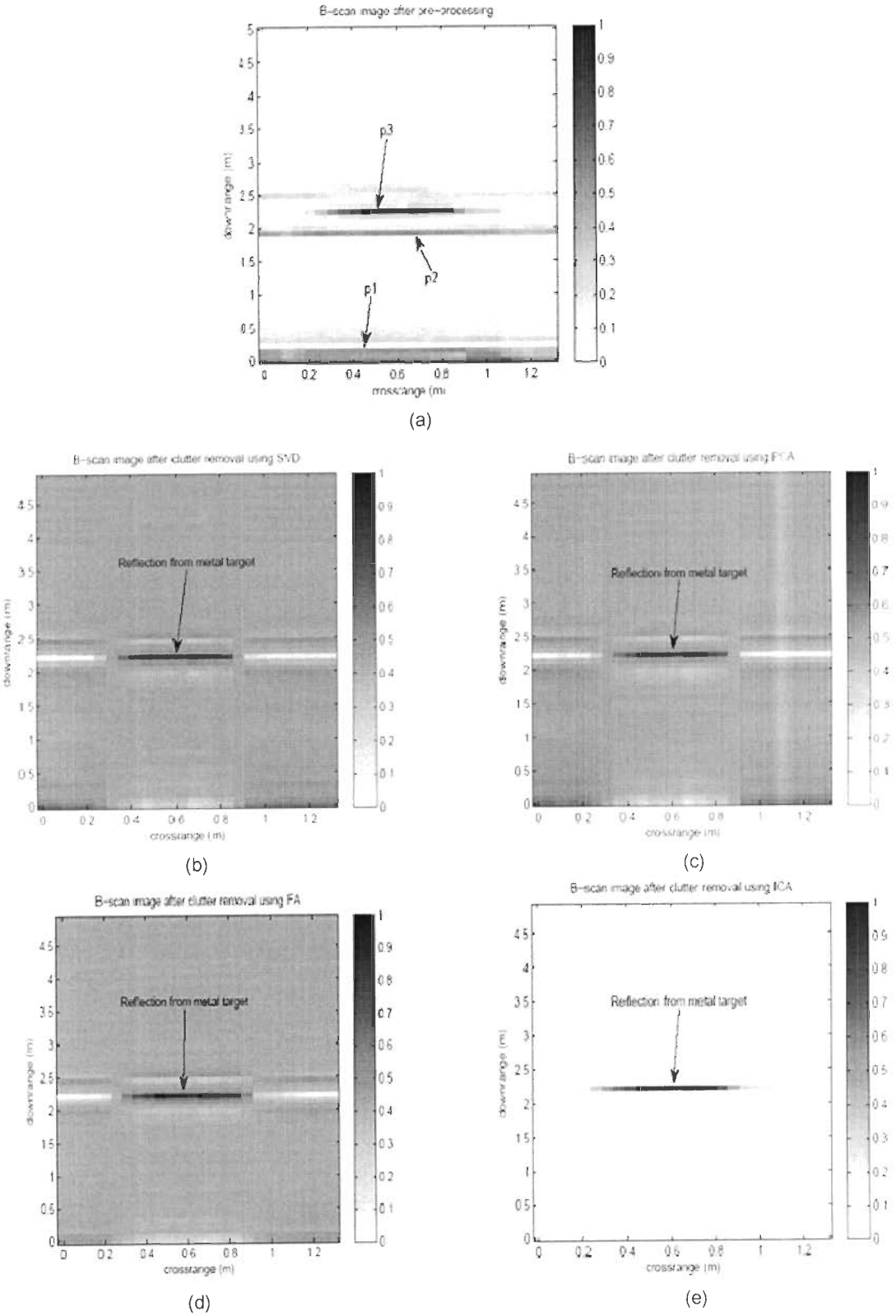

Figure 3.2 B-scan image plotted for single target behind plywood wall (a) At step 6 (b) At step 7 using SVD (c) At step 7 using PCA (d) At step 7 using FA (e) At step 7 using ICA

Table 3.1 Performance of clutter reduction technique on basis of PSNR in case of single metal target behind plywood wall

S. No	Clutter reduction technique	PSNR(dB)
1	SVD	20.07
2	PCA	19.85
3	FA	21.44
4	ICA	43.69

The PSNR value computed using equation 3.2 and equation 3.3 for different clutter reduction techniques are shown in Table 3.1. It is clearly observed from Table 3.1 that ICA has better PSNR compared to other three techniques. By visualizing the results shown in Figures 3.2 (b), (c), (d) and (e), it is observed that in ICA based technique target is enhanced more i.e. the contrast between target and background of image is more.

(b) *For brick wall*

The performance of various clutter reduction techniques is evaluated by replacing plywood wall by brick wall in this experiment. The problem of detection of target increases further when brick wall is used because attenuation of signal due to presence of brick wall increases. Thus very weak target reflection will reach receiver making it as absent i.e. missed target. The details of data collection are described in Table 1.2, S. No. 4. The B-scan image obtained at step 6 is shown in Figure 3.3 (a). It is observed that clutter dominates and obscures the weak target reflections. Constant reflection p_1 due to problem of isolation between transmitting and receiving ports is observed. Similar constant reflection p_2 along horizontal scanning line is observed due to front side of brick wall. A constant reflection p_3 along horizontal scanning line is expected even for other side of brick wall as thickness of brick wall is greater than down range resolution but it is observed that at some places the reflection is very weak. Though single target is kept behind wall, multiple comparable reflections indicating that multiple targets are present are observed in the image. These indicate false targets. After observing these reflections it is difficult to say that there is only one target without *apriory* information.

Table 3.2 Performance of clutter reduction technique on basis of PSNR in case of single metal target behind brick wall

S. No	Clutter reduction technique	PSNR(dB)
1	SVD	17.17
2	PCA	16.26
3	FA	15.51
4	ICA	42.84

This false target detection can be minimized with the application of clutter reduction techniques. Figures 3.3 (b), (c), (d), and (e) show B-scan image obtained at step 7 that is after applying SVD, PCA, FA and ICA respectively. It is clearly observed that a good amount of clutter is minimized and target is highlighted. The calculated values of PSNR are tabulated in Table 3.2 from which it is again observed that ICA based clutter reduction technique outperform in comparison to other techniques.

(c) *Extracted range profile for brick wall*

Performance of various clutter reduction techniques was also evaluated by extracting the range profile from the clutter reduced B-scan image when brick wall was used. In Figure 3.4, range profiles are plotted for antenna position x=16. It represents target signal before applying clutter reduction techniques (blue solid line) and after applying clutter reduction (red dashed line). Reflection due to target is clearly visible as other reflections have been reduced in clutter reduced range profile. Figure 3.4 (a, b, c, and d) represent range profiles after step 4 and after step 7 by applying SVD, PCA, FA and ICA. One can see a strong target peak at around 2.763 m in each range profile after applying clutter reduction techniques. It is observed that signal to clutter ratio is quite improved for all applied clutter reduction techniques. The probability of false alarm is also reduced after minimisation of false peaks by application of these clutter reduction techniques which is clearly shown by the dashed line in Figures 3.4 (a), (b), (c) and (d). Data points are shown at each peak from which signal strength can be read. In range profile without clutter reduction, strongest peak amplitude of 0.9053 is observed which may be due to the isolation problem between transmitting port and receiving port. It is marked in Figure 3.4 (a) as $p1$.

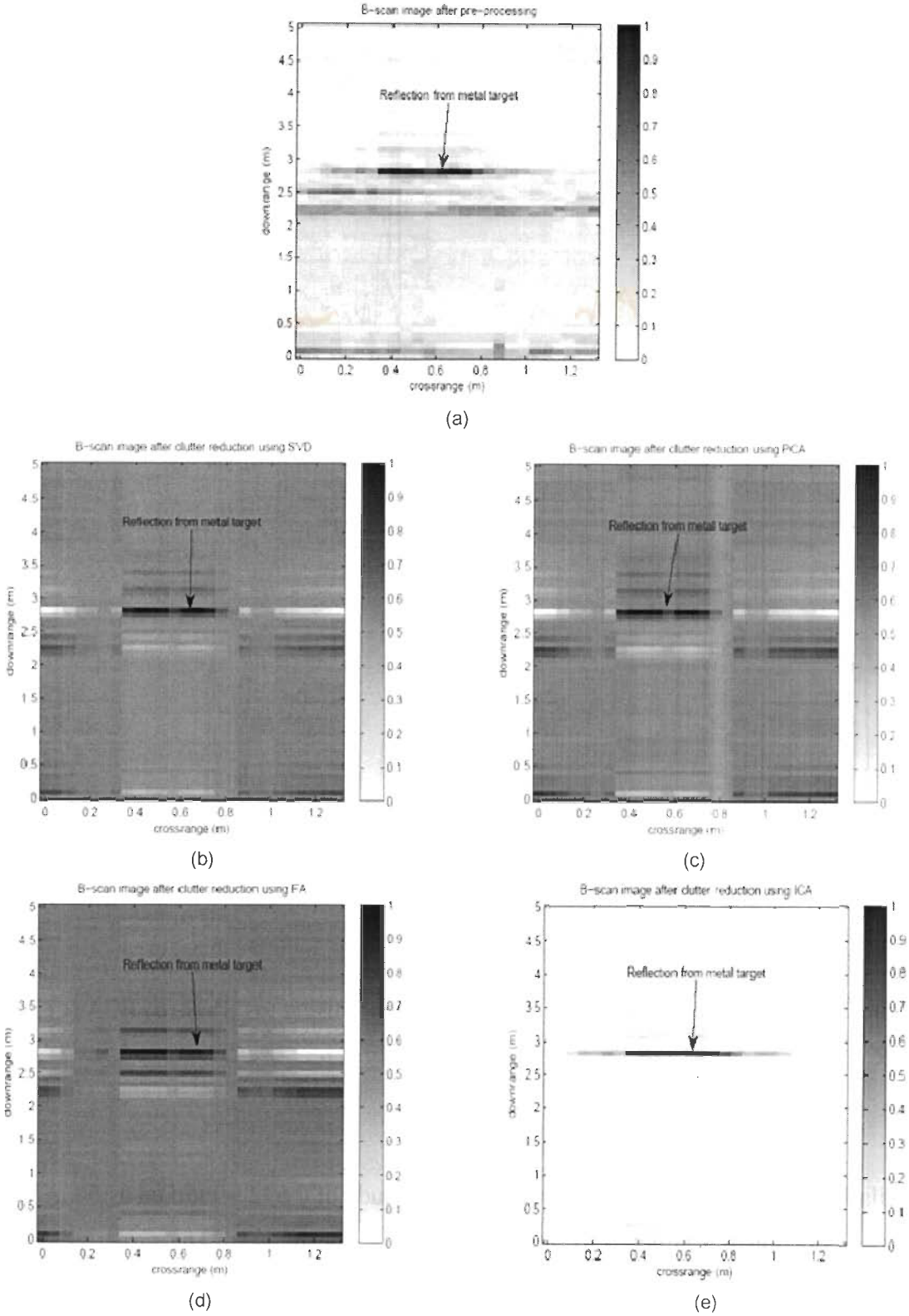

Figure 3.3 B-scan image plotted for single target behind brick wall (a) After step 6 (b) After step 7 using SVD (c) After step 7 using PCA (d) After step 7 using FA (e) After step 7 using ICA

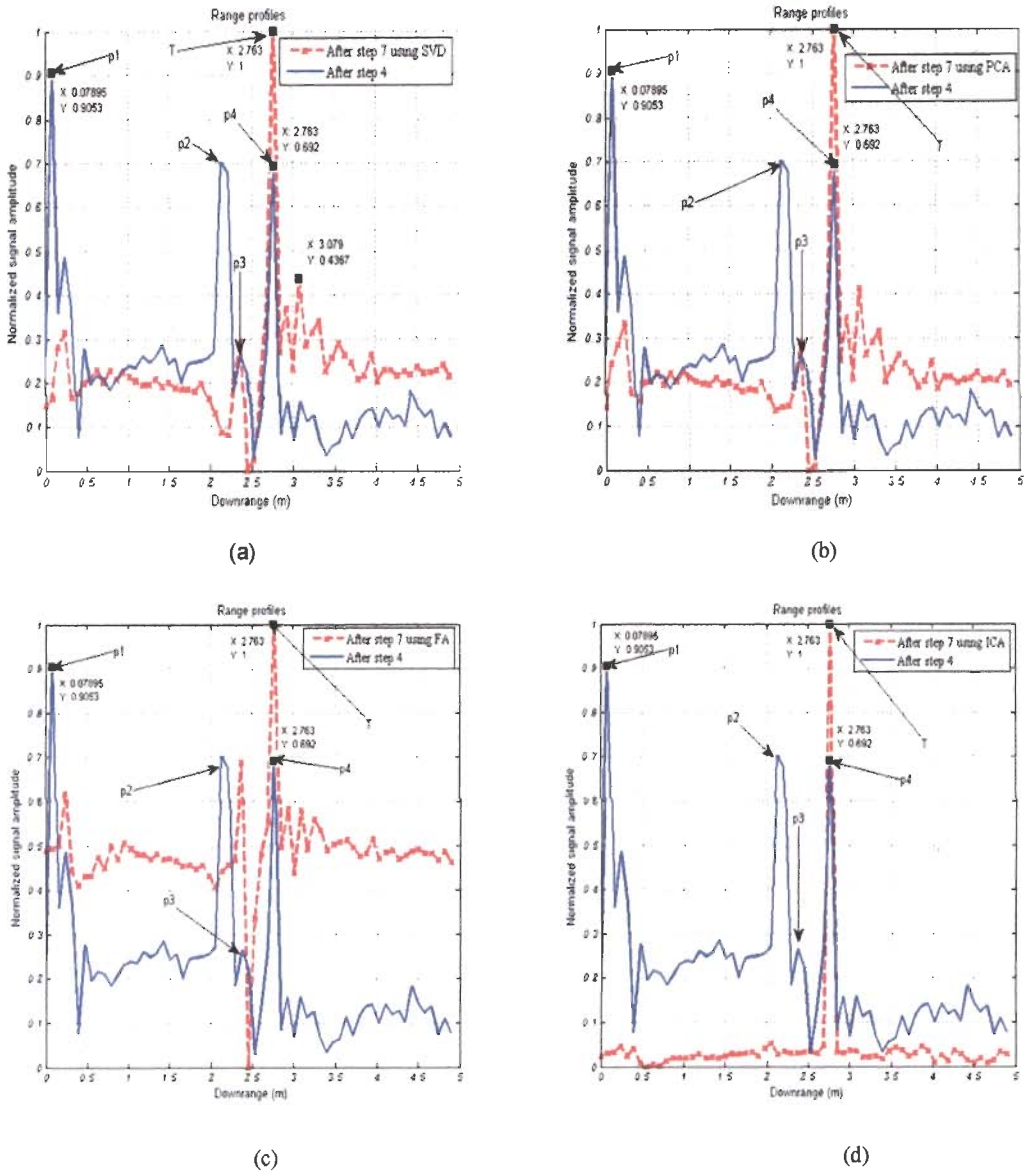

Figure 3.4 Range profiles after step 4 and after step 7 using (a) SVD (b) PCA (c) FA (d) ICA

Similarly target peak which is weak and has amplitude of 0.692 is marked as *p4*. After clutter reduction the target peak is expected to be the highest. The target peak is observed in each technique from Figures 3.4 (a), (b), (c), and (d) and is marked as T in each case. In case of SVD the maximum amplitude difference between target peak and undesired peak is 0.5633 whereas in PCA, FA and ICA it is 0.5888, 0.3111 and 0.9479 respectively. It is inferred that target peak is enhanced more by the application of ICA as compared to other techniques.

3.3.2 Clutter reduction for double target behind the wall

In TWI, detection is possible due to dielectric contrast between target and room environment. Detection of low dielectric constant material becomes more difficult due to weak reflection from such targets. To verify detection of low dielectric constant material, Teflon whose dielectric constant is approximately 2.0 is taken as target.

(a) *For plywood wall*

In this experiment, to verify detection capability, both metal and Teflon targets are kept at same distance in down range behind plywood wall with separation in cross range distance by 0.3 m between them. The geometrical setup is as described in Figure 1.7 (Chapter 1) with the data collection details as in Table 1.3, S. No. 1.

After plotting raw B-scan image as shown in Figure 3.5, only one target is observed and it is due to stronger reflection from metal target. The second target (Teflon) is not observed due to weak reflections. Weak reflection occurred due to low dielectric contrast between air and Teflon and reflection level of Teflon may be difficult to distinguish with the level of clutter being so high. So, the raw image is processed using clutter reduction techniques to reduce clutter and enhance target information. From results as shown in Figure 3.5 (b), (c), (d) and (e), it is observed that all the considered clutter reduction techniques have clearly resulted in improvement in detection of metal target while Teflon target is detected only after the application of ICA.

Table 3.3 Performance of clutter reduction technique on basis of PSNR in case of double target behind plywood wall

S. No	Clutter reduction technique	PSNR(dB)	Results
1	SVD	29.07	Only metal target detected
2	PCA	29.23	Only metal target detected
3	FA	33.89	Only metal target detected
4	ICA	35.59	Both metal and Teflon target detected

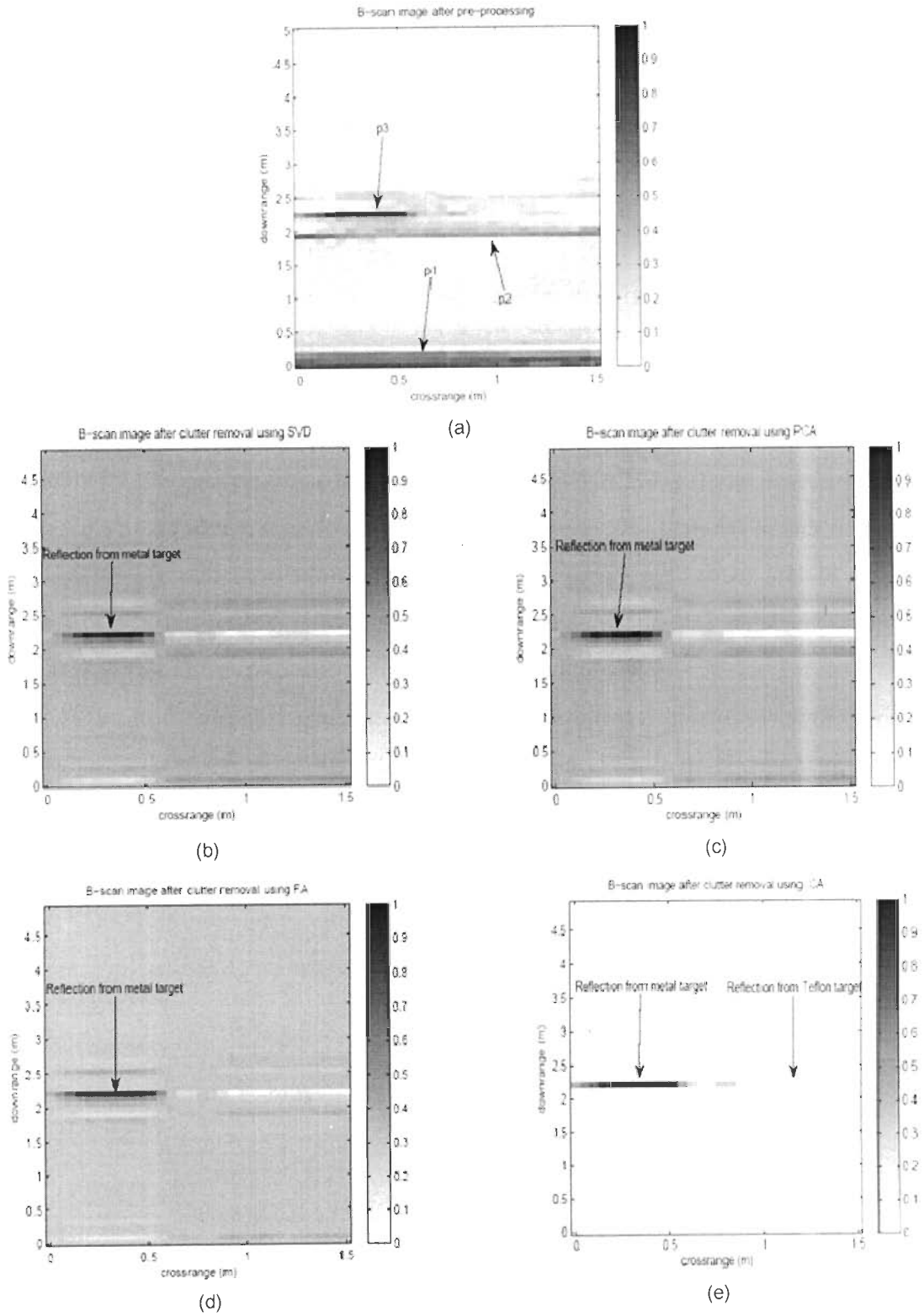

Figure 3.5 B-scan image plotted for double target behind plywood wall (a) After step 6 (b) After step 7 using SVD (c) After step 7 using PCA (d) After step 7 using FA (e) After step 7 using ICA

(b) *For brick wall*

Since detection of Teflon target is possible only due to ICA clutter reduction technique, only ICA is further evaluated for detecting Teflon target behind brick wall. In this experiment, two targets i.e. a metal plate and a Teflon plate are used. The details of target dimension and separation between them are given in Table 1.3. S. No. 3. After plotting raw B-scan image, only one stronger reflection from metal target is observed. Second target is not observed due to weak reflection from Teflon. After processing using ICA clutter reduction technique, the detection of Teflon target is possible. Results before and after clutter reduction using ICA are shown in Figure 3.6 (a) and (b) respectively.

To further analyze the effect of clutter reduction, range profiles after step 7 at antenna scan position at which target is present is observed. Comparison of range profiles obtained with and without applying clutter reduction is carried out. It is observed from range profiles at different antenna scan positions that the target peak amplitude varies considerably with antenna scan position in horizontal scanning direction. From B-scan, the lateral position of the point of strong reflection is observed at x=5, which is the position of metal target and x=25 is the position of Teflon target.

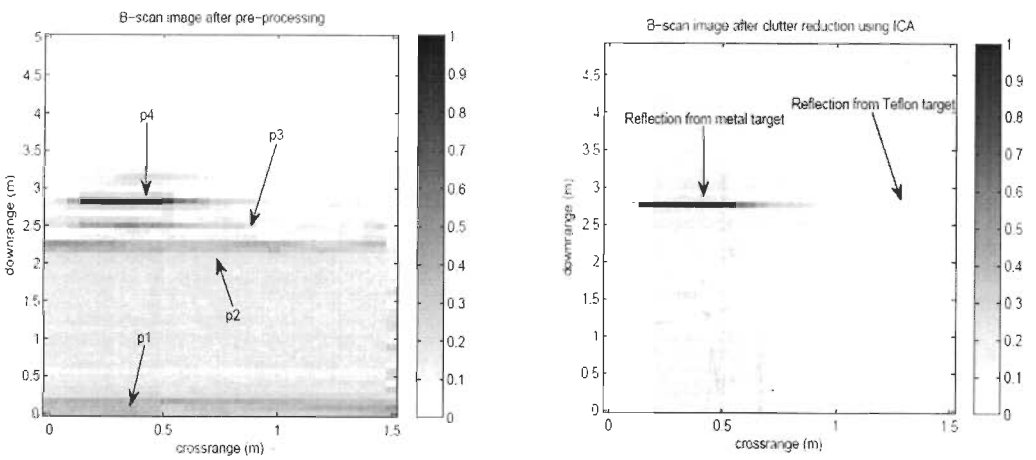

(a) (b)

Figure 3.6 B-scan image plotted for double target behind brick wall (a) After step 6 (b) After step 7 using ICA

The range profiles are extracted from B-scan image (Figure 3.6 (b)) for antenna scan position at which target is present. Since the metal target is detected quite significantly after clutter reduction techique, the range profile for metal plate is not shown here. Range profile is observed for antenna scan position x= 25, which represent Teflon target. Figure 3.7 represent range profiles after step 4 and after step 7 by applying ICA. Data points are shown at target and clutter peak from which the signal strength can be read. As discussed in Section 1.3.4, and observed here in the range profile without clutter reduction (blue solid line), the first peak marked as p_1 is due to weak isolation between transmitting and receiving port of antenna system, second peak marked as p_2 is due to front side of brick wall, third peak p_3 is due to back side of brick wall and the fourth peak p_4 is due to target. Since the first peak is strongest it is considered as highest clutter signal. The observed signal strength at clutter peak (p_1) and weak Teflon target peak (p_4) are 0.6583 and 0.1682 respectively. After applying clutter reduction technique ICA, the peak due to Teflon target (red dashed line) is quite enhanced as shown in Figure 3.7. The strong target peak is observed around 2.763 m in range profile after applying clutter reduction techniques. The peak is marked as T. The level of clutter is less than 0.1 and the peak of Teflon target is enhanced to approximately 1.0. Thus the difference between amplitude of target and clutter is enhanced from 0.4901 to 0.9 by using ICA clutter reduction technique.

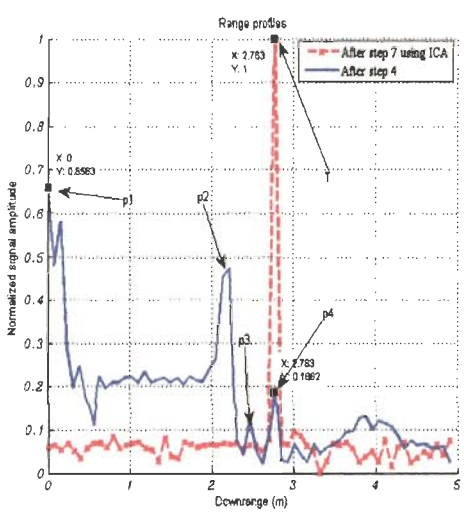

Figure 3.7 Represents range profile for Teflon target with and without application of clutter reduction techniques.

It infers that ICA has capability to reduce clutter more efficiently and increase the detection capability of low dielectric target behind the wall.

3.4 Concluding remarks

The focus of this chapter is to explore the possibility of application of various existing clutter removal techniques for TWI data and also to check the possibility of detection of low dielectric target. After applying clutter reduction techniques, clutters are successfully minimized which implies that the techniques are powerful. Detection of metal target kept behind wall is improved using all the clutter removal techniques described here. It is found that ICA based technique gives better result in comparison to other clutter removal techniques like SVD, PCA and FA. PSNR for B-scan image obtained by using ICA clutter removal technique is quite high when compared to B-Scan images obtained by using other clutter removal techniques.

SVD, PCA and FA are not able to detect the target having low dielectric constant, like Teflon behind the plywood wall and for brick wall. On the other hand ICA based clutter removal technique has a better potential to detect low dielectric constant target like Teflon behind the plywood wall and even for brick wall. Thus ICA based technique may be applied to enhance the target signal detection. Processing using clutter reduction increases target signal strength which increases the probability of correct target detection and hence it is useful for further process of identification.

Chapter 4

A novel approach to detect and classify the targets

4.1 Introduction

The objective of this chapter is to address two issues i.e. target detection and classification. Preprocessing and application of clutter reduction techniques on B-scan images were discussed in Chapter 1 and 3. The detection of targets as well as classification of the targets with TWI system evokes high practical importance. Thus after detection certain dominant characteristics of target of interest should be extracted which will be different from other objects present in TWI scene. Detection of targets is addressed in [39] using principles of classical detection theory to TWI. Neyman-Pearson criterion is used to derive probability of detection and false alarm. FMCW radar based detection of target buried in wet snowpack is presented by Yamaguchi et al. [233]. For classification, radar data can be interpreted broadly in three ways, electromagnetic analysis, time-spectral analysis and spatial analysis. Discrimination of target based on estimation of dielectric constant has been

investigated [208]. Savelyev et al. [190] used time–frequency features of an ultra wideband target response for discrimination between landmine and other targets. In most of the cases, particularly in ground penetrating radar (GPR), pattern recognition technique is used to identify and classify buried targets [170]. Since learning process is statistical in nature, statistical classification has been widely used [94, 227]. Shihab et al. [192] has used high order statistical features to discriminate between targets and background. Mine targets were classified by extracting features using Karhunen Loeve transformation (KLT) and Kittler Young transformation (KYT) [164]. Other feature based techniques used for classification are Hough transform, Radon transforms [209] and Wavelet transforms [23]. Most of the techniques described above are either sensitive to shift in time due to changes in position of target and changes in antenna position from wall or sensitive to propagation effect. Some techniques require large set of training data or are computationally intensive. Thus utmost care should be taken for selection of feature extraction method. In this chapter, target material discrimination is approached as a classification problem.

The chapter is organized as following. Section 4.2 describes the existing different thresholding techniques. Section 4.3 compares the results of different thresholding technique. Further the statistics of typical TWI thresholded images is examined and thresholding model development for detection of low dielectric constant material with fixed false alarm rate (FAR) is proposed in Section 4.4. In Section 4.5, appropriate pdf for modelling of multiple targets is obtained. Concluding remarks are mentioned in Section 4.6.

4.2 Existing thresholding techniques

B-scan image is thresholded after clutter removal to discriminate between targets and background. Several algorithms have been proposed for computing optimum threshold value in order to segment target information [187]. The pixels with value below threshold are pertaining to background and pixels with values above threshold represent target. Thresholding becomes difficult when the target and background gray levels possess substantially overlapping distribution. Various thresholding methods based on information such as space clustering, entropy and spatial information were exploited by various researchers and are discussed in this section. Five methods,

namely as cluster based thresholding given by Ridler and Calvard [137], Otsu's thresholding [159], cross entropy [118], maximum entropy [224] and thresholding based on statistics (mean and standard deviation) [28] have been implemented and compared.

4.2.1 Cluster based thresholding method

In this method, gray levels samples are clustered in two parts, background and foreground [137]. Threshold may be calculated by using equation (4.1)

$$t = \frac{\mu_o + \mu_1}{2} \tag{4.1}$$

where μ_o and μ_1 are means of each of the two components of the histogram separated by the threshold. An iterative algorithm is as follow:

- An initial threshold value is selected
- Two means for two distributions on either side of threshold are calculated
- New threshold is obtained using equation 4.1
- The process is continued until the value of threshold converges

4.2.2 Otsu's thresholding method

Otsu's method [159] is a very popular global automatic thresholding technique, in which a threshold is determined by maximizing discriminant measure. Otsu's method maximizes the *aposteriori* between class variance $\sigma_B^2(t)$, which is given by

$$\sigma_B^2(t) = \omega_o(t)\omega_1(t)[\mu_1(t) - \mu_o(t)]^2 \tag{4.2}$$

This expression is reduced to equation (4.3) with the terms defined in (4.4)

$$\sigma_B^2(t) = \omega_o(t)[1-\omega_o(t)]\left[\frac{\mu_T(t) - \mu_t(t)}{1-\omega_o(t)} - \frac{\mu_t(t)}{\omega_o(t)}\right]^2 \tag{4.3}$$

$$\left.\begin{aligned}\omega_o(t) &= \sum_{i=0}^{t} \frac{n_i}{N} \\ \omega_1(t) &= 1 - \omega_o(t) \\ \mu_t(t) &= \sum_{i=0}^{t} i \frac{n_i}{N} \\ \mu_T(t) &= \sum_{i=0}^{L-1} i \frac{n_i}{N}\end{aligned}\right\} \tag{4.4}$$

where n_i represents the number of pixels with gray level i , L is the number of gray levels and N is the total number of pixels in the image. Optimal threshold t_{op} is found through a sequential search for the maximum of $\sigma^2_B(t)$ for the values of t , where $0 \leq t < L$. The advantage of this method is its simplicity and optimal value is selected automatically based on global properties and not on local properties.

4.2.3 Iterative method for minimum cross entropy thresholding

An iterative method to obtain the threshold that minimizes the minimum cross entropy is used in [118]. For a histogram, the zeroth and the first moments of the foreground and background portions of the thresholded histogram are respectively

$$\left.\begin{aligned}m_{0a}(t) &= \sum_{i=0}^{t-1} h(i) \\ m_{0b}(t) &= \sum_{i=0}^{L} h(i) \\ m_{0c}(t) &= \sum_{i=0}^{t-1} i * h(i) \\ m_{0d}(t) &= \sum_{i=0}^{L} i * h(i)\end{aligned}\right\} \tag{4.5}$$

And the portions' means are defined as

$$\left.\begin{aligned}\mu_a(t) &= \frac{m_{1a}(t)}{m_{0a}(t)}, \\ \mu_b(t) &= \frac{m_{1b}(t)}{m_{0b}(t)}\end{aligned}\right\} \tag{4.6}$$

The minimum cross entropy method selects the threshold which minimizes the cross entropy of the image and its segmented version. The criterion function is found to be

$$\eta(t) = -m_{1a}(t)\log\{\mu_a(t)\} - m_{1b}(t)\log\{\mu_b(t)\} \tag{4.7}$$

The optimal threshold t_{op} is given by the minimiser of equation (4.7)

$$t_{op} = \arg\min, \eta(t) \tag{4.8}$$

The calculation of the optimal threshold involves the evaluation of $\eta(t)$ for all possible threshold values. The computation can be significantly reduced by developing a numerical method for the minimization. A necessary condition for the minimum of $\eta(t)$ is obtained by setting the derivative of $\eta(t)$ to zero. The derivative of $\eta(t)$ is given as equation (4.9).

$$\eta'(t) = h(t)\left[t\log\frac{\mu_a(t)}{\mu_b(t)} - \{\mu_a(t) - \mu_b(t)\} \right] \tag{4.9}$$

For $\eta'(t)$ to be zero, either $h(t)=0$ or the second term in equation (4.9) is zero. As $h(t)=0$ is satisfied only by those threshold values where the image does not contain such gray values, these solutions can be considered as trivial solutions to the thresholding problem. Thus the solution is sought at the zero of the second term in equation (4.9). Setting the second term to zero and simplifying results in,

$$t = \frac{\mu_b(t) - \mu_a(t)}{\log\{\mu_b(t) - \mu_a(t)\}} \tag{4.10}$$

Applying the one-point iteration method to (4.11), the following iterative procedure is obtained for calculating the optimal threshold

$$t_{n+1} = round\left\{ \frac{\mu_b(t) - \mu_a(t)}{\log\{\mu_b(t) - \mu_a(t)\}} \right\} \tag{4.11}$$

where n ≥ 0 with an initial guess t_0 until the iteration converges. The convergence is the conditions where $t_{n+1}=t_n$. The round (x) function is generally used to round x to its nearest integer. Additional description of this algorithm has been given by Li et al. [118].

4.2.4 Maximum entropy-based thresholding method

This method is based on the maximum entropy principle in which both spatial information and gray level distributions of image are used. The optimal threshold value is determined by maximizing *aposteriori* entropy that is subject to certain inequality constraints which are derived by means of special measures characterizing uniformity and shape of the regions in the image. The maximum entropy principle serves as a certain criterion to select *apriori* probability distributions when very little or nothing is known. It states that, for a given amount of information, the probability distribution, which best describes the knowledge, is the one that maximizes the Shannon entropy subject to the given evidence as constraints.

A bi-level image is obtained after thresholding the image by a threshold value t. *Aposteriori* probability of the pixels with gray values less than t is given by

$$F(t) = \sum_{i=0}^{t} p_i \tag{4.12}$$

$$where \quad p_i = \frac{n_i}{N} \quad and \quad N = \sum_{i=0}^{L-1} n_i \tag{4.13}$$

where N is total number of pixels in the image and L is the total number of gray levels.

Similarly, the *aposteriori* probability of all those pixels with values greater than or equal to t is $1–F(t)$. Thus, the Shannon entropy of image is

$$H(F(t)) = -F(t)\log F(t) - \{1 - F(t)\}\log\{1 - F(t)\} \tag{4.14}$$

Logarithm is taken with respect to base 2, and 0log0 is assumed to be zero as described by Wong and Sahoo [224]. The goal is to maximize (4.14) in order to obtain the optimal threshold value for the image while satisfying constraints that is

derived from the spatial information of the image. These measures provide constraints for the probability of the pixels corresponding to both classes. The two measures are as following: (1) uniformity measure and (2) shape measure. The details regarding these measures are given by Wong and Sahoo [224].

Maximization of $H(F(t))$ subject to the obtained constraints always yields a unique solution; thus, the optimal threshold t^* is determined from

$$t^* = \arg\max H(F(t)) \tag{4.15}$$

such that the threshold image will have maximum uniformity as well as maximum shape information.

4.2.5 Statistics based thresholding

Following technique is used for statistics based thresholding [28].

$$t = \mu + \sigma \tag{4.16}$$

where μ is mean of image pixel and σ is standard deviation of image pixel.

4.3 Results of thresholding techniques

4.3.1 Data used

Figure 1.7 shows the geometrical arrangement used for the observation taken in the experiment. The details of the experiment are described in Chapter 1, Table 1.3.

Metallic and non metallic (Teflon) targets (flat surface plates) are used for analysis. Teflon target (approximately dielectric constant is equal to 2) with low dielectric contrast with air is chosen to check the performance of the technique, as it would be difficult to detect and image the low dielectric target behind the wall. Shape of targets is square with dimension 0.58 m each side. Since the B-scan images contain reflections from the scanning area where target is present behind wall, only ten set of TWI B-scan images are selected for analysis.

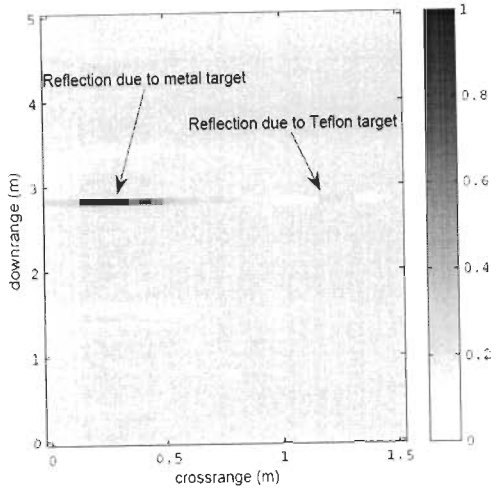

Figure 4.1 B-scan images for double target at different stages after applying Clutter reduction technique

These ten B-scan images are obtained at different heights for which target size and shape does not change within the scanning portion i.e. scanning position 10 to 20. The obtained observations are used to assess the performance of target detection and classification. Figure 4. 1 shows one of the B-scan image at one of the height (height number 11) after applying calibration technique, velocity corrections and clutter reduction using ICA technique as described in Chapter 3. The reflection due to metal target is significantly higher when compared to reflection due to Teflon target.

4.3.2 Comparison of existing thresholding techniques

For comparison between different thresholding techniques, normalized B-scan image is obtained after clutter reduction. Normalization is done to remove dependence on target dimension and distance between antenna and target. It is defined as:

$$E_{normalization} = \frac{E - E_{\min}}{E_{\max} - E_{\min}} \tag{4.17}$$

Where, E is the prescribed data value and E_{min} and E_{max} are minimum and maximum data values of the image respectively.

To compare the thresholding algorithms, the performance of algorithms was evaluated by computing performance measures. Two performance measures i.e. sensitivity (SN) and specificity (SP) as given in (4.18) and (4.19) were used

$$SN = \frac{\text{Correctly detected target pixels}}{\text{Total target pixels}} \tag{4.18}$$

$$SP = \frac{\text{Correctly detected non target pixels}}{\text{Total number of pixels - Total number of target pixels that exist}} \tag{4.19}$$

Since sensitivity is proportion of pixels correctly identified by algorithms as target and specificity is the proportion of pixels correctly identified by the algorithms as non-target, the higher value of these two measures (closer to one), results in greater accuracy of algorithm. This study helps to choose a technique based on performance on both measures i.e. sensitivity and specificity, particularly for Teflon targets. The total number of existing pixels for each target is determined with the help of *apriori* information i.e. known size of targets, resolution of image and position of targets. The antenna position x=3 to 13 represent metal target and 20 to 30 represent Teflon target. Out of 11 positions, in case of metal target, most of them are detected whereas in case of Teflon few are detected.

Table 4.1 shows comparison of the performances of all five thresholding techniques in terms of sensitivity and specificity for detecting metal and non metallic target at different heights.

Significant sensitivity was achieved for metal target by all the thresholding methods, whereas in case of Teflon target Otsu thresholding technique was unable to detect pixels successfully. Results show that cross entropy and iterative algorithm thresholding techniques detect Teflon significantly. But, when compared with respect to sensitivity and specificity, maximum entropy outperforms other techniques.

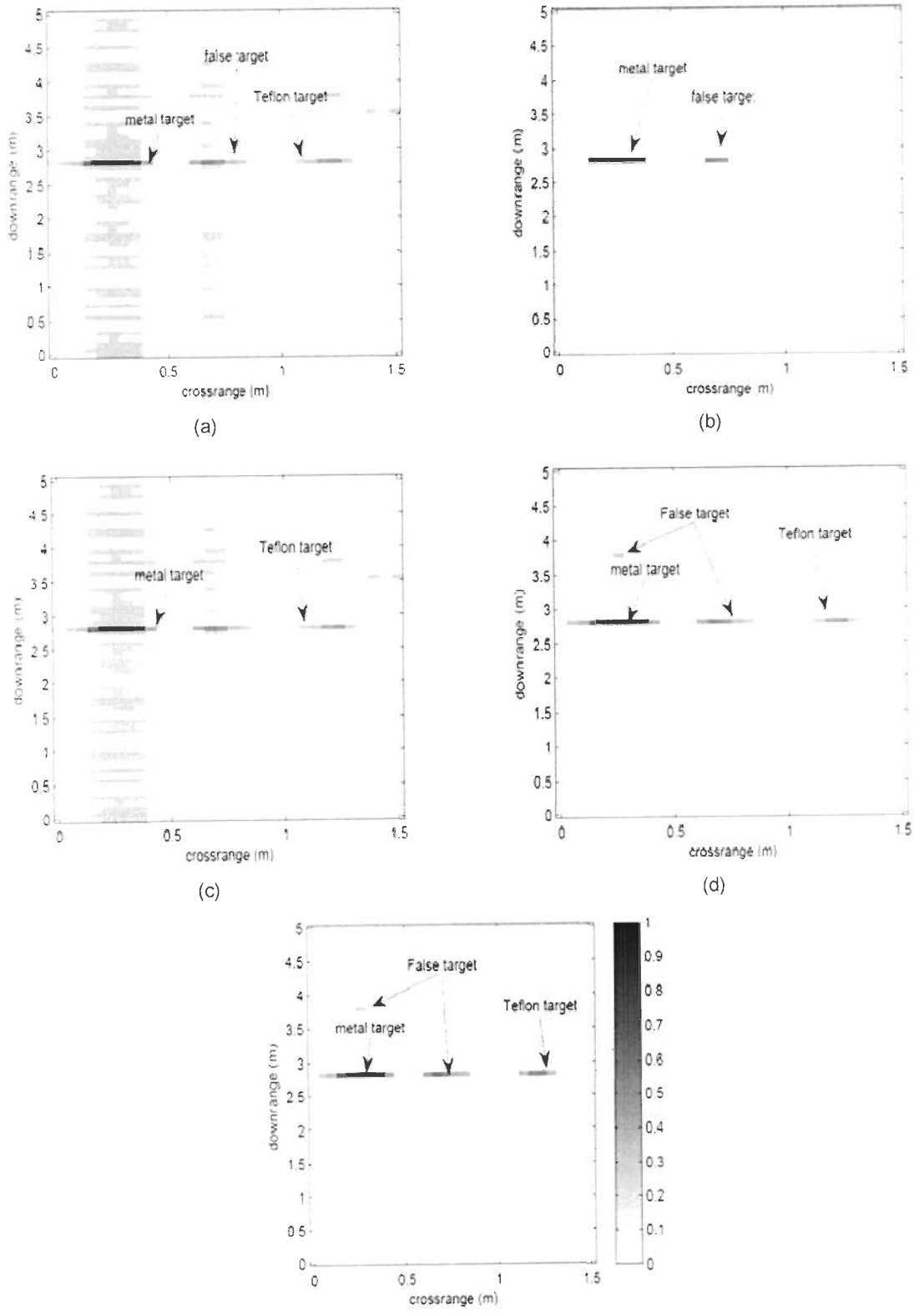

Figure 4.2 B-scan image after thresholding (a) Cluster based thresholding (b) Otsu method (c) cross entropy method (d) maximum entropy method (e) mean with standard deviation method.

Results obtained after applying all the described thresholding techniques on B-scan image are shown in Figure 4.2. The threshold values obtained for B-scan image due to different thresholding techniques are 1) Cluster based = 0.2401; 2) Otsu = 0.4501;3) Cross entropy = 0.2399; 4) Maximum entropy = 0.2700; 5) Statistic based (mean+std) = 0.2688. As observed from Figure 4.2 (a) and (c) that if the threshold value is small, number of pixels detected for Teflon target is more but number of false targets also increases. The pixel intensities which do not represent target may be due to noise or remaining clutter data. These pixels are called false target. If the threshold value is too high then target detection is missed as observed from Figure 4.2 (b). Due to high threshold value obtained using Otsu algorithm, Teflon target is missing. Maximum entropy based thresholding performs better than statistics based (mean+std) method, as it is observed from Figure 4.2 (d) and (e) that number of pixels detected for Teflon target are more in maximum entropy based thresholding than statistics based method. Detection of pixels representing Teflon as well as false alarm is better in maximum entropy than all other methods as observed from results. It is observed that all the methods discussed above have some limitation due to either higher or lower threshold values. Therefore, a statistical thresholding model is proposed to detect the target while computing the user defined threshold values.

4.4 Development of adaptive thresholding model

An image statistics based thresholding technique is modified for detection of target, particularly for non metallic target. As an example, B-scan image obtained after thresholding according to equation (4.16) is shown in Figure 4.2 (e). From results it can be seen that the number of pixels detected corresponding to Teflon is lower than the metal pixels. In order to achieve more accurate Teflon detection, threshold value should be set accordingly. It is also observed that all the intensity values corresponding to Teflon (low dielectric constant) are not greater than background pixels. If detection of low dielectric constant is improved then false alarm rate will also increase. Thus difficulty is in detection of target pixels representing low dielectric constant and not in high dielectric constant. Therefore, optimum threshold value should be selected to increase detection and reduce false alarm. To segment the image, thresholding technique is modified as:

Table 4.1 Comparison of the performances of all five thresholding techniques in terms of sensitivity and specificity for detecting metal and non metal target at different heights.

Height No.	Mean+std				Maximum Entropy				Iterative method Cross entropy				Otsu				Cluster based			
	Metal		Teflon		Metal		Teflon		Metal		Teflon		Metal		Teflon		Metal		Teflon	
	SN	SP	SN	SP	SN	SP	SN	SP	SN	SP	SN	SP	SN	SP	SN	SP	SN	SP	SN	SP
10	0.8182	0.9979	0.1818	0.9979	0.9910	0.9888	0.3636	0.9888	0.991	0.4532	0.4545	0.9532	0.8182	0.9995	0	0.9995	0.9091	0.9548	0.4545	0.9548
11	0.7272	0.9968	0.3636	0.9968	0.7272	0.9968	0.3636	0.9968	0.7273	0.9005	0.4545	0.9005	0.5455	0.9995	0	0.9995	0.7273	0.9026	0.4545	0.9026
12	0.8182	0.9963	0.1818	0.9963	0.8182	0.9936	0.1818	0.9936	0.8182	0.9782	0.2727	0.9782	0.5455	1	0	1	0.8172	0.9787	0.2727	0.9787
13	1	0.9984	0.0909	0.9984	1	0.9952	0.1818	0.9952	1	0.892	0.2727	0.892	0.7273	1	0	1	1	0.8941	0.2727	0.8941
14	1	0.9984	0.0909	0.9984	1	0.9888	0.1818	0.9888	1	0.9255	0.1818	0.9255	0.8182	1	0	1	1	0.9303	0.1818	0.9303
15	1	0.9979	0	0.9979	1	0.9915	0	0.9915	1	0.9095	0.0909	0.9095	0.6364	1	0	1	1	0.9143	0.0909	0.9143
16	1	0.9952	0.0909	0.9952	1	0.9713	0.1818	0.9713	1	0.9415	0.1818	0.9415	1	1	0	1	1	0.9447	0.1818	0.9447
17	1	0.9968	0	0.9968	1	0.9659	0	0.9659	1	0.8792	0	0.8792	0.9091	1	0	1	1	0.8893	0	0.8893
18	1	0.9963	0	0.9963	1	0.9798	0	0.9798	1	0.9718	0	0.9718	1	1	0	1	1	0.9798	0	0.9798
19	1	0.9947	0	0.9947	1	0.9622	0	0.9622	1	0.9526	0	0.9526	0.8182	1	0	1	1	0.9542	0	0.9542

$$t = \mu - (n-1)\sigma \tag{4.20}$$

Value of n is constant and chosen suitably. For lower value of n all the pixels representing higher dielectric constant target are detected whereas if high value of n is chosen then pixels representing low dielectric constant target are detected.

For example when n value is 0.05, then threshold value is 0.2670 whereas when n=1, threshold is 0.2336. The B-scan images after applying different threshold values obtaind by varying n are shown in Figure 4.3 (a), (b) and (c) for n=0, 0.05, and 1 respectively where dependence of n is clearly observed.

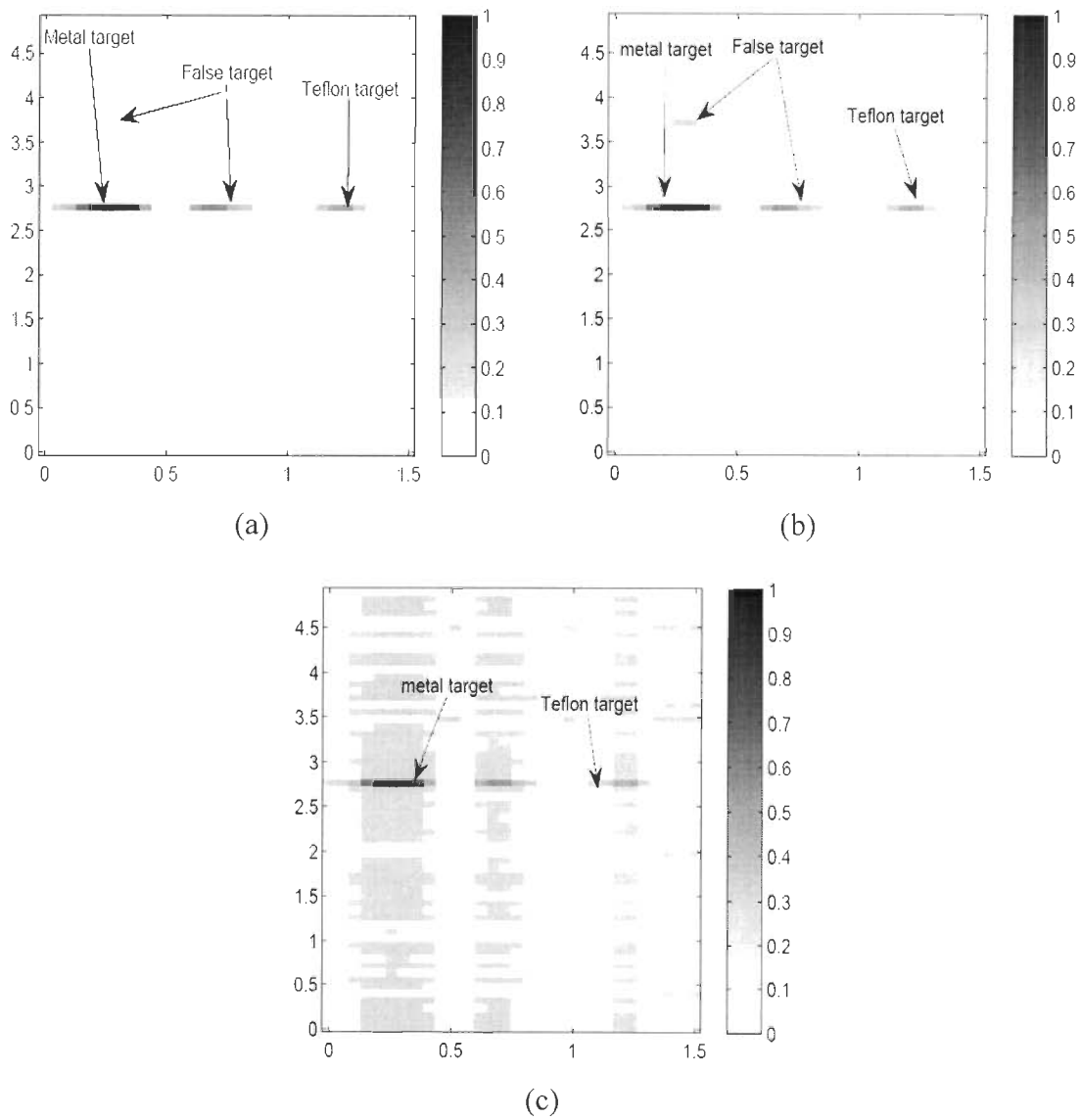

Figure 4.3 B-scan images after different n values (a) n=0, (b) n=0.05, and (c) n=1

To optimize the performance of proposed algorithm for optimum detection for both metallic and non metallic targets with low false alarm rate (FAR), it is important to select the value of n carefully. The algorithm should behave in such a manner that it should give the highest sensitivity (SN) while maintaining an upper bound on FAR. In order to get the desired performance, the performance of the algorithm is computed terms of sensitivity and specificity. The performance parameters, sensitivity and specificity for metallic target pixels as well as non-metallic target pixels were observed with changes in value of n.

It is observed that the sensitivity of metallic target remains almost constant for all values of n where as for non metallic target; the sensitivity varies with n. So concentration on analysis of non metallic target having low dielectric constant (i.e. Teflon) is done. When the value of n reaches to say n_1, the total number of pixels representing low dielectric constant target becomes zero while when the value of n increases to n_2, the number of correctly detected pixels of target with low dielectric constant becomes constant. If the value of n increases then the false alarm rate increases. Thus the optimum value of n should be such that detection of low dielectric constant target is maximized and the false alarm rate is minimized.

To obtain the optimum value of 'n', the plot of sensitivity and specificity with respect to n is analyzed as shown in Figure 4.4. It is observed that the behavior of these performance parameters is similar to exponential function. Thus an empirical relationship can be developed. Sensitivity and specificity can be easily described in mathematical form using curve fitting technique with very high value of R^2 (coefficient of determination). i.e. 0.999 and 0.925 respectively as given in equations (4.21) and (4.22)

$$sensitivity(n) = a_1 e^{b_1 n} + c_1 e^{d_1 n} \tag{4.21}$$

$$specificity(n) = a_2 e^{b_2 n} + c_2 e^{d_2 n} \tag{4.22}$$

where a_1, b_1, c_1, d_1, a_2, b_2, c_2 and d_2 are constants and values of these constants are obtained from the curve fitting method. The mathematical functions of sensitivity and specificity obtained for heights with their corresponding R^2 values are given in Table 4.2. The level of confidence is 95%. It is observed that the R^2 value obtained for each

image at different height is throughout greater than 0.75 leading to conclusion that proposed relationship is quite acceptable.

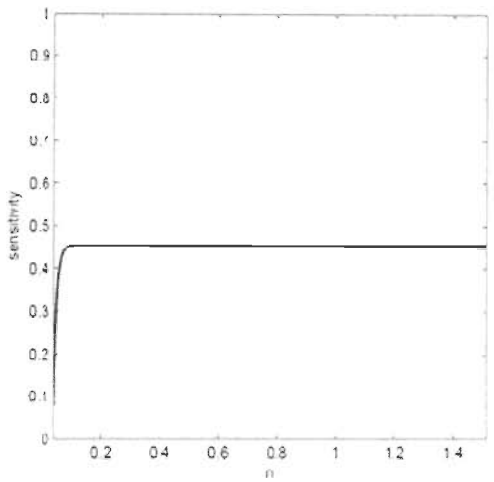

(a)

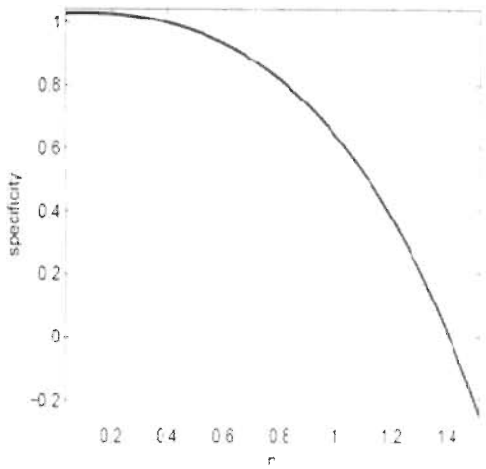

(b)

Figure 4.4 Analysis of Teflon target for different values of n a) Sensitivity b) Specificity

Table 4.2 Empirical function of specificity and sensitivity with corresponding R^2 values

Height No	**Sensitivity** $f(x)=a_1\times\exp(b_1\times x)+c_1\times\exp(d_1\times x)$					**Specificity** $f(x)=a_2\times\exp(b_2\times x)+c_2\times\exp(d_2\times x)$				
	a_1	b_1	c_1	d_1	R^2	a_2	b_2	c_2	d_2	R^2
12	7170	0.7973	-7169	0.7974	0.8658	4.57E-07	7.132	0.1662	0.5079	0.8332
13	6118	0.7887	-6117	0.7889	0.8985	-.1727	-22.39	0.1356	0.7183	0.9016
14	1599	0.795	-1558	0.7955	0.8941	0.1229	0.4518	-0.0601	-2.589	0.7589
15	-2797	0.8225	2798	0.8222	0.9088	-29.31	3.806	29.32	3.805	0.8476
16	2822	0.8241	-2821	0.8243	0.8971	0.08422	0.816	0.0003	4.62	0.9407
17	-1180	0.8265	1181	0.8259	0.9210	163.2	0.9834	-163.3	0.9829	0.8954
18	2575	0.7967	-2874	0.7969	0.8582	886	0.0802	-886.1	0.0798	0.8296
19	1.88E+04	0.7833	1.88E+04	0.7832	0.8869	169.4	0.54	-169.4	0.5395	0.8051

4.4.1 Mathematical formulation to obtain the optimum value of *n*

There is need to maximize sensitivity to increase the detection of target and minimize false alarm rate. The optimum value particularly for target having low dielectric constant, should satisfy user specified constraint. Two constraints are required to be satisfied. These are: 1. sensitivity should be greater than user specified lower bound and 2. FAR should always be lesser than user specified upper bound. It is observed that for detection of metal target, even high value of threshold is able to detect it. But detection of non metallic target having low dielectric constant material, target will be missed due to high threshold value. So threshold value should be low enough to detect low dielectric constant target. On the contrary, it should not be too low as it will increase FAR. The performance of algorithm is analyzed in terms of sensitivity and specificity for different values of *n* in case of low dielectric constant target as shown in Figure 4.4. Mathematical formulation to obtain value of '*n*' is carried out after user has fixed the lower bound of sensitivity and upper bound of FAR. FAR is equal to (1–specificity). It is described mathematically as nonlinear constraint multiobjective optimization problem and is written as equation (4.23).

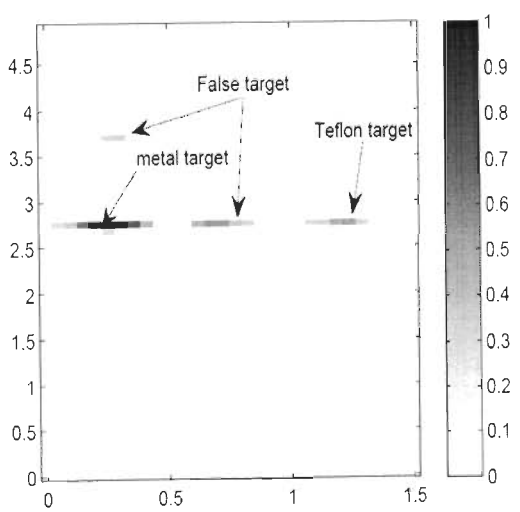

Figure 4.5 B-Scan image for n=0.1

$$\left.\begin{aligned} &\min F(n) = \frac{f_1(n)}{f_2(n)} \\ &where,\ f_1(n) = -sensitivity(n) \\ &f_2(n) = FAR(n) \\ &subject\ to\ f_1(n) \geq lb_{sensitivity}, f_2(n) \leq ub_{FAR}, \quad 0 < n \leq 1 \end{aligned}\right\} \tag{4.23}$$

For example to get the value of n, equations 4.21 and 4.22 is used, where user fixes the value of sensitivity and specificity. In this case, lower bound on sensitivity for Teflon is set as 0.4545 and lower bound set on specificity as 0.9947. Because for low dielectric target behind the wall the reflected signal is generally in the range of clutter, lower and upper bound are fixed. Once user provides the value of sensitivity and specificity, n value can be obtained from equation 4.21 and 4.22. The obtained optimum value of n is found to be 0.1. For this value of n, the threshold value is equal to 0.2653. The B-Scan image after applying this threshold value is shown in Figure 4.5. Number of detected pixels for Teflon targets are increased in Figure 4.5 compared to Figure 4.3 (a).

4.5 Classification based on probability distribution function

Statistical model that will characterize TWI data can be used to get the information about targets. It is therefore important to investigate the distribution of all the targets in order to detect and differentiate them more accurately. Generally statistics of TWI image is examined to obtain probability distribution functions for modelling background noise and all other objects which significantly deviate from this model are detected as targets. The target image statistics at wide bandwidth frequency range will be more helpful for classification [40]. But use of probability distribution to differentiate targets or classify targets is given less attention. Therefore, in this section, TWI image statistics have been evaluated and based on these results, targets are classified.

B-scan image shown in Figure 4.1, is used for analysis after thresholding by the technique described in earlier section to get the information about presence of targets. Then the probability distribution function of image is obtained. Image data is grouped

into parts in case of multiple targets i.e. after thresholding, pixels representing different targets are separated. These set of pixels are used for analyzing distribution of pixels corresponding to each class. *Apriory* information like size of target, location of target in image and distance between two targets is used to decide number of pixels representing metal and Teflon target. There are thirty pixels in one row in which pixel position 3 to 13 represent metal target and 20 to 30 represent Teflon target. Out of 11 pixels, most of them are detected in case of metal target, whereas in case of Teflon few are detected.

This procedure is applied to all ten B-scan images (images obtained at different heights). When image is obtained by illuminating the scene of interest from multiple heights, target appears at same location in all images. A reliable set of pixels of metal and Teflon target are obtained from all images at different heights. These set of pixels are used for analyzing distribution of pixels corresponding to each class. The probability density function of TWI data is obtained from 110 pixels values for metal and 50 pixels for Teflon targets. Four common distribution models i.e. Normal, Rayleigh, Cauchy and Weibull are applied on the obtained image data and best fit has been checked. The respective pdfs of these distributions for x as pixel intensity have been given below [25, 171, 178, 191]:

$$f(x) = \frac{\exp(-\frac{(x-\mu)^2}{2\sigma^2})}{\sigma\sqrt{2\pi}} \tag{4.24}$$

Where, σ is continuous scale parameter ($\sigma>0$) and μ is continuous location parameter.

$$f(x) = \frac{x-\gamma}{\sigma^2}\exp(-\frac{1}{2}(\frac{x-\gamma}{\sigma})^2) \tag{4.25}$$

Where, σ is continuous scale parameter ($\sigma>0$) and γ is continuous location parameter.

$$f(x) = \frac{1}{\pi\sigma(1+(\frac{x-\mu}{\sigma})^2)} \tag{4.26}$$

Where, σ is continuous scale parameter (σ>0) and μ is continuous location parameter.

$$f(x) = \frac{\alpha}{\beta}\left(\frac{x}{\beta}\right)^{\alpha-1} \exp\left(-\left(\frac{x}{\beta}\right)^{\alpha}\right) \tag{4.27}$$

where, α is shape parameter and β is scale parameters. Both α and β must be greater than zero.

In TWI, numbers of target pixels are limited so Normal distribution cannot be assumed. An empirical study of target statistics is required to be carried out for target classification. Researchers have used distributions either to represent noise or target for detection purposes. Probability distribution to differentiate different targets is still given less attention.

Probability distribution function is then obtained on the basis of Chi-squared goodness of fit test. The Chi-squared goodness of fit test has been largely used to determine which distribution best fits the data. The Chi-squared statistics is given by Peck et al. [171].

$$\chi^2 = \sum_{i=1}^{k} \frac{(O_i - E_i)^2}{E_i} \tag{4.28}$$

where O is observed frequency for bin i, E is expected frequency for bin i and k is total number of bins.

Chi-squared test is used to determine whether the sample comes from the population with specific distribution. Chi-squared statistics is compared with all distributions and the distribution which has lesser chi-square statistics is chosen. Thus chi-squared statistics, which is a function of data value, reflects in some way the level of agreement between the data and the hypothesis. The goodness of fit is quantified by giving p-value. If the hypothesis used to compute the p-value is true, then for continuous data, p will be uniformly distributed between zero and one, with a value closer to one indicating better fit. Figure 4.6 shows comparison of pdf curves (Weibull, Cauchy, Rayleigh and Normal) for Teflon and metal respectively. It shows

appearance of pdf of Teflon and metal when plotted on same graph. It is observed that metal pdf is significantly separated from Teflon and Teflon pdf is spikier than metal pdf.

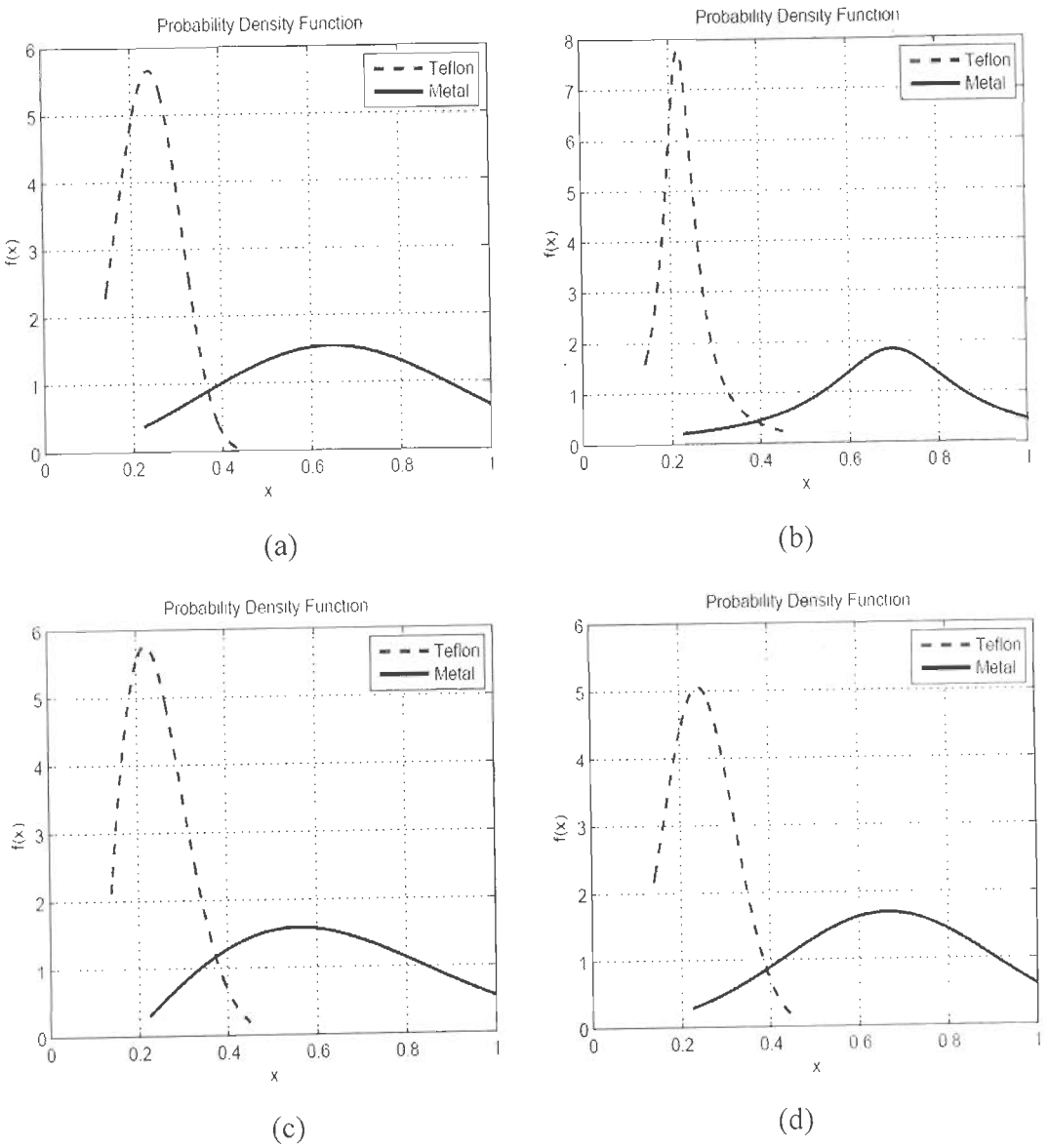

Figure 4.6 Pdf for metal and Teflon data for different distributions (a) Teflon and metal Weibull pdf (b) Teflon and metal Cauchy pdf (c) Teflon and Metal Rayleigh pdf (d) Teflon and metal Normal pdf

Table 4.3 Chi-squared statistics for various distributions

S. No	Data	Distribution	Chi-squared statistics with 5 % significance level		
			Chi square-Statistics	p-value	Critical value
1	Teflon	Normal	2.9591	0.3979	7.81
		Rayleigh(2p)	2.081	0.555	7.81
		Cauchy	1.7379	0.6285	7.81
		Weibull	0.5910	0.9640	9.48
2	Metal	Normal	8.83	0.1826	12.59
		Rayleigh (2p)	5.87	0.1649	12.59
		Cauchy	4.52	0.6065	12.59
		Weibull	3.84	0.7031	12.59

Table 4.4 Parameters for Weibull distribution fitting

Distribution	Teflon		Metal	
Weibull	α	β	α	B
	3.207	0.2708	3.256	0.7446

Table 4.3 shows chi-squared statistics for various distributions applied on Teflon and metal target data. This test is used to determine which distribution provides the best fit to the data. It is observed from Table 4.3 that Weibull distribution fits both targets (Teflon and metal) more accurately than other three distributions. The statistics value and p-value for Teflon data and metal data are 0.5910, 0.9640 and 3.84, 0.7031 respectively.

The observed values of Weibull distribution parameters are given in Table 4.4. It is inferred that probability distribution function appears to consistently follow a Weibull distribution for target like Teflon and metal. The Weibull function [17] is a probability distribution function that takes a number of different shapes depending on its parameters. It is important to see the effect of shape and scale parameter on the distribution curve. The shape parameter is also called as slope parameter. Different values of shape parameter will change pdf distribution and indicate whether the function increases with x, remains constant or decreasing. If α is less than one then function decreases with x and if α is greater than one then, function increases with x.

If α =1, then Weibull distribution becomes exponential distribution function. The scale parameter β is a measure of spread in the distribution of data, i.e. where the bulk of distribution lies. The scale parameter has the same effect on distribution as change in abscissa scale. If α is kept constant and β is increased then pdf is stretched out. Since the area under pdf curve remains constant, the peak of curve decreases. The scale parameter β has significant difference for Teflon and metal with values 0.2708 and 0.7446 respectively. The scale parameter β for metal is increased so its height is reduced and plot is stretched to the right. Thus β may be used to distinguish between Teflon and metal.

4.5.1 Parameter estimation

Once the distribution is known, parameters are estimated using maximum likelihood estimator and then from this parameter, the groups of pixels are labeled as Teflon or metal. Maximum likelihood decision rule is used to discriminate the targets. Thus after target detection, pixels are classified as metal or low dielectric material based on the estimated parameters. Group of pixels which gives sufficient statistics are chosen for classification. Estimation of parameter of each image formed at each height is carried out and results are shown in Table 4.5. The average values of scale and shape parameter for metal and Teflon are 0.5995, 2.06 and 0.16, 4.5 respectively. The standard deviation values of scale and shape parameter for metal and Teflon are 0.069, 0.26 and 0.060, 3.65 respectively. Based on this, the scale parameter can be set to either 0.5995+0.069=0.7595 or 0.5995-0.069=0.5305 for Metal and 0.16+0.069=0.229 or 0.16-0.069=0.091 for Teflon. If the value of β is less than 0.5305 then it will represent Teflon and if value is greater than 0.5305 then it represents metal.

4.5.2 Validation

Once the statistical distribution of the target signature is known, the discrimination between targets can be examined from the output of maximum likelihood method. Data from different experimental setup is chosen for validation. Here the frequency range is kept same. The distance between wall and target is increased to 1 m and distance between antenna and wall is reduced to 0.8 m. Cross range distance between

two targets is kept same. Orientation of target is not changed. Figure 4.7 shows the resultant image obtained after applying clutter reduction technique. Normalization as described in Section 4.3.2 equation (4.17) is applied. Normalization is done to remove dependence on target dimension and distance between antenna and target. Thus actual amplitude information is lost and classification process will rely on targets dielectric characteristics. After thresholding is applied on the normalize image, the group of pixels representing targets are used to estimate parameter. Care should be taken while selecting group of pixels representing target, i.e. non zero pixel values should be used for estimating parameter. Even after optimum thresholding some unknown reflections of same magnitude as of Teflon target are observed in resultant images. The remaining unwanted signal can also be taken for classification and may be classified as target which will be false information. In Table 4.6, the maximum likelihood estimates for Teflon data and metal data are shown. Thus the pixels for which the scale parameter value is obtained as β=0.08 is classified as Teflon and pixels for which scale parameter is 0.82 is classified as metal. The entire testing was repeated in order to evaluate classification to the variation of number of pixels representing targets. Thus Weibull distribution parameters are used to differentiate between Teflon and metal target.

Table 4.5 Parameters for Weibull distribution fitting estimated at each height

Height No.	Metal		Teflon	
	α	β	α	β
10	2.09	0.57	1.68	0.21
11	1.94	0.53	2.68	0.29
12	1.71	0.51	2.73	0.19
13	1.76	0.52	2.71	0.17
14	1.81	0.55	1.87	0.13
15	2.03	0.58	1.58	0.12
16	2.27	0.68	13.7	0.15
17	2.28	0.68	3.21	0.10
18	2.48	0.65	5.75	0.11
19	2.28	0.67	5.21	0.10

Table 4.6 Validation of metal and Teflon discrimination based on Weibull distribution

Distribution	Teflon		Metal	
Weibull	α	β	α	β
	7.31	0.08	4.7	0.82

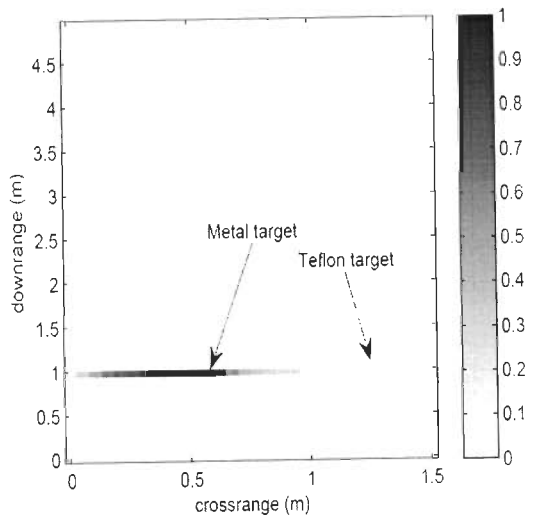

Figure 4.7 B-scan image after thresholding used for validation

4.6 Concluding remarks

The task of reliable, efficient and robust target parameter extraction for TWI is of great importance in order to enable discrimination between different targets. Optimum threshold to separate objects from background is still a challenge in segmentation. Different techniques based on entropy, cluster analysis, spatial information and statistics are studied and compared for computing the threshold values. There are some constraints to obtain the threshold values with these methods. So, a modified statistical based threshold method is proposed and it is found that it performs quite well from point of view of detection of pixels representing Teflon as well as false alarm rate. After detection, model based on pdf is proposed for target classification (i.e. metallic and non metallic targets). Weibull distribution is quite suitable to classify the targets as metallic and non-metallic.

Chapter 5

Study of prevalent imaging techniques for through wall target detection

5.1 Introduction

Researchers in TWI are interested in surveillance as well as in imaging applications. Imaging is required to acquire more information about target which will be useful for recognition of targets whereas, in surveillance, detection of target is sufficient. Imaging describes the process of obtaining an image of the spatial distribution of reflectivity of target from TWI system scattered field. For these purposes, different scanning techniques have been used such as A, B and C scanning as described earlier in Chapter 1, Section 1.3.1. Normal unfocused B-scan image is sufficient when only detection of target and its approximate position is required. But for highly accurate information about target location and its shape, high resolution image is required. Thus, one of the major thrust in TWI involves development of more efficient imaging algorithms which give maximum information about obscured target [14]. Many imaging algorithms are reported in literature and it is important to explore the use of

these algorithms with TWI data [6, 43, 90]. The most commonly used techniques in TWI for image formations are back projection and delay sum (DS). Several migration algorithms have been reported in GPR [244]. Migration techniques were developed for seismic applications [65]. Synthetic aperture system based focusing technique has been applied to GPR data [162]. Because of similarity of data collection scheme between GPR and TWI, SAR based focusing technique can also be applied on TWI data. Till now very limited work has been reported on the considered popular imaging techniques i.e., back projection, delay sum and ω-k. Therefore, these techniques were evaluated for the same experimental data and their performance is critically analyzed in this chapter. Section 5.2 describes need of B-scan imaging and different imaging techniques commonly used in TWI. Comparisons of different techniques are given in Section 5.3. Section 5.4 shows results obtained from different imaging algorithms which is followed by conclusions in Section 5.5.

5.2 Need for B-scan imaging

5.2.1 Back projection

In this section, comparison of the results when different imaging techniques are applied on A-scan data (data at single position) and on B-scan data is carried out. The general idea behind imaging is that grid is assumed according to antenna swath. The grid chosen may be horizontal or vertical. Then for various pixel values on the grid, intensity values are calculated using various imaging algorithms.

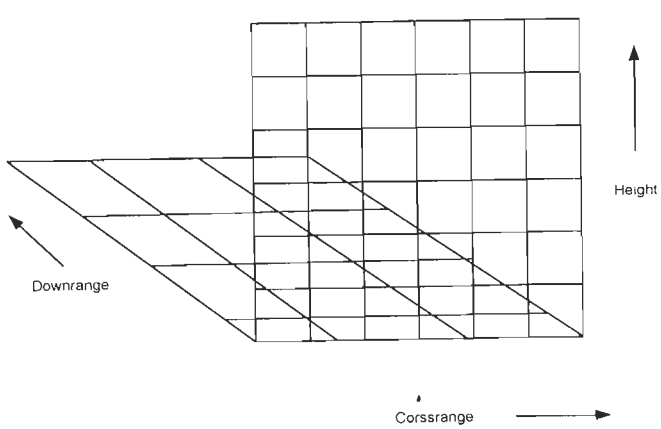

Figure 5.1 Horizontal and vertical grid

Figure 5.1explains the concept of a vertical and horizontal grid. The horizontal grid is created in the cross range - down range plane and the vertical grid is created in the cross range - height plane. The concept and the use of imaging using different types of data (A-scan, B-scan and C-scan) will be explained in this section.

Figure 5.2 shows the back projected A-scans for TWI system locations 3, 4, 15 and 25 along the horizontal direction on the scanner. Reflections due to weak isolation can be observed in all the four images. The second reflection observed can be attributed to the plywood wall. For the target, a locus is formed which confirms the presence of the target behind the wall.

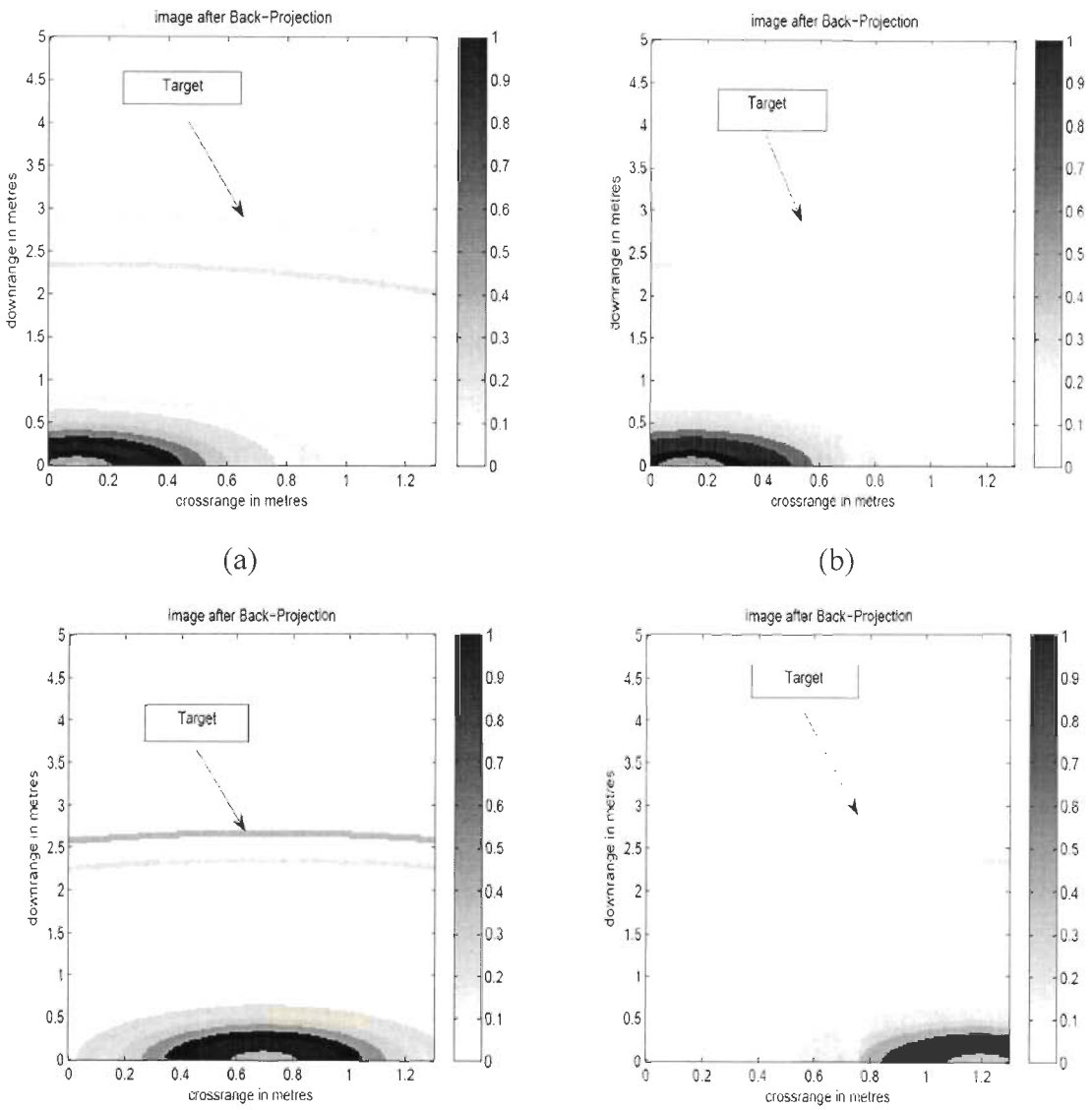

Figure 5.2 Back projected A-scans at locations (a) 3, (b) 4, (c) 15, (d) 25

Hence, detection can be achieved using A-scan data. However, the precise location of the target behind the wall cannot be ascertained as a locus is formed and the target can lie on any point on that locus. It is observed that the orientation of the locus changes as the TWI system is placed at locations 3, 4, 15 and 25 along the horizontal direction on the scanner. This is expected as the distance of the target from the TWI system will change when it is kept at different locations.

So it is observed that using the information of a single A-scan, it is not possible to precisely localize the target behind the wall. Hence, a B-scan is required for this task, which is a combination of A-scans taken at different locations in the azimuth (horizontal) direction. Back projected image is obtained, but now a number of A-scans are used instead of a single A-scan. Extra information is added when more A-scans are used and the target locus decreases in its extent as well as the target location gets more precise. To study this, first A-scans obtained at locations 13 to 16 were used to generate the back projected image. As can be observed from Figure 5.3(a) that the locus of the target gets smaller and tails appear at the ends. The tails appear due to inherent properties of the back projection algorithm [15]. When complete B-scan data is used, as is shown in Figure 5.3(b) which comprises of 26 A-scans along the azimuth, the complete back projected image is generated. The precise location of the target can be found out using this image. The lateral extent of the target can also be obtained using this image.

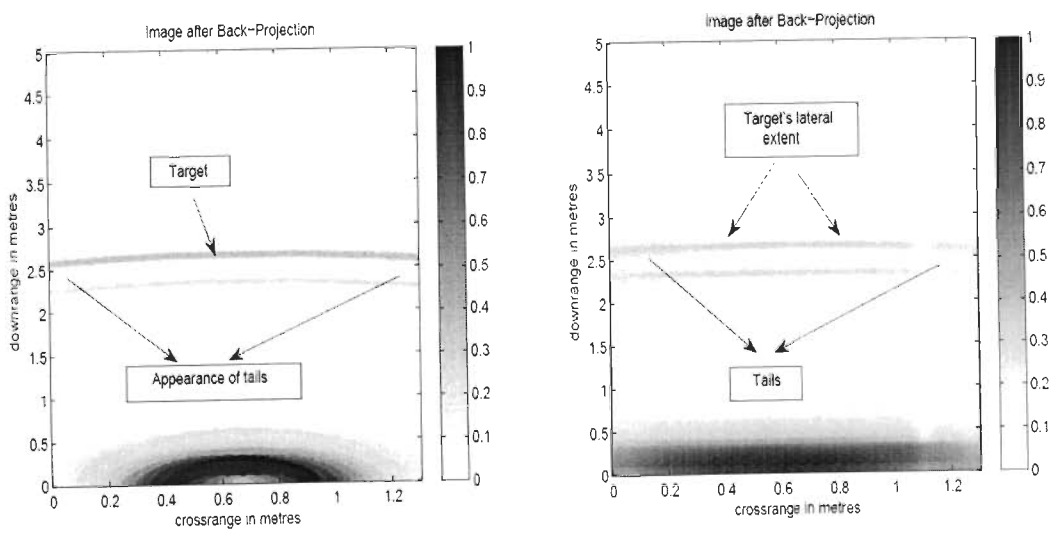

(a) (b)

Figure 5.3 Back projected B-scan from A-scan locations (a) 13-16 (b) 1-26

Therefore only for rough detection, A-scan image may be useful otherwise B-scan image will certainly provide better target information. Thus B-scan data is used or if even more information i.e. the height of the target is required then C-scan is required.

5.2.2 Delay sum algorithm

It is observed from Figure 5.4, target locus is generated for A-scan images when the TWI system is kept at different locations along the azimuth. This has been illustrated using A-scans for locations 5, 8, 17 and 18. The results are as expected, and similar to back projected image results.

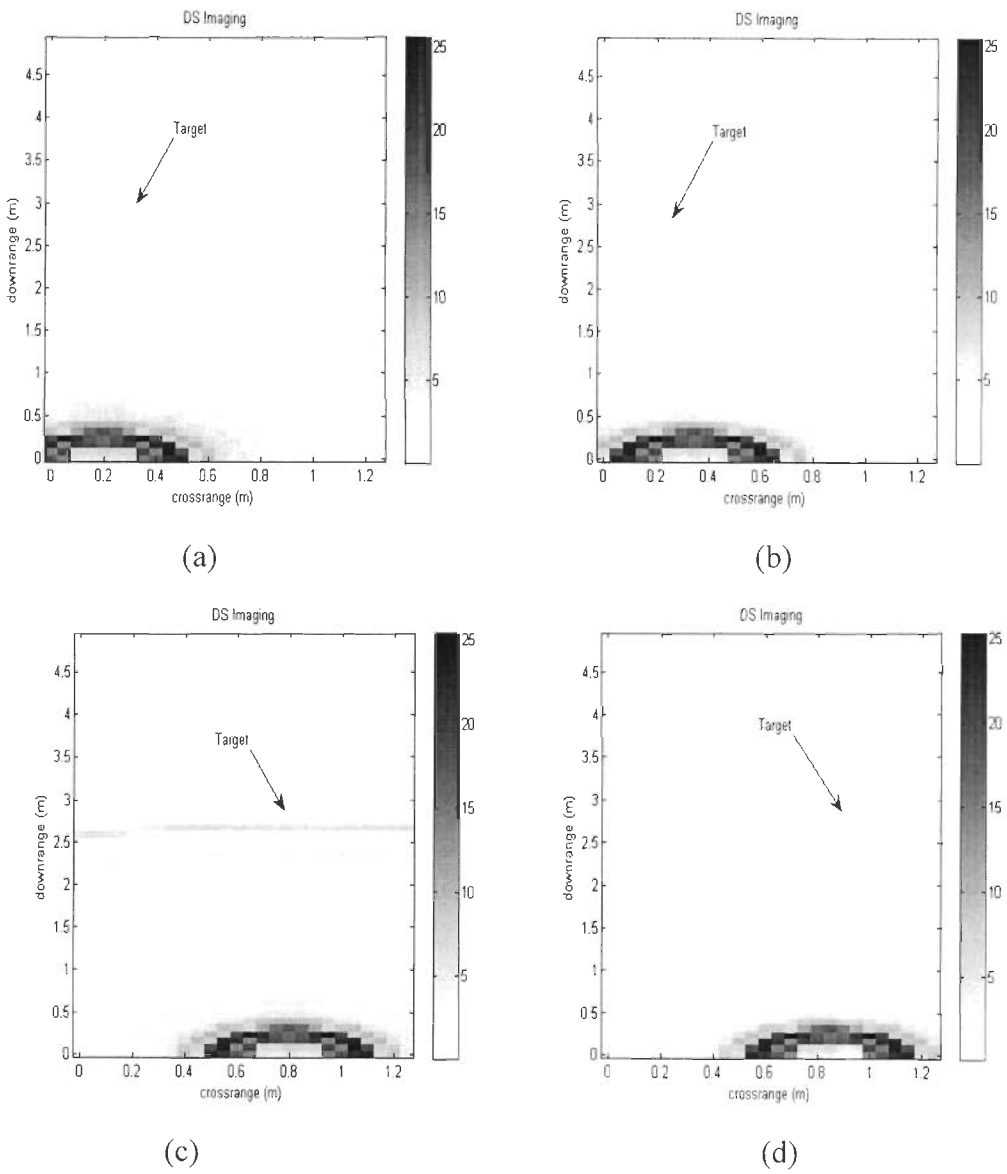

Figure 5.4 Delay sum A-scans at locations (a) 5, (b) 8, (c) 17, (d) 18

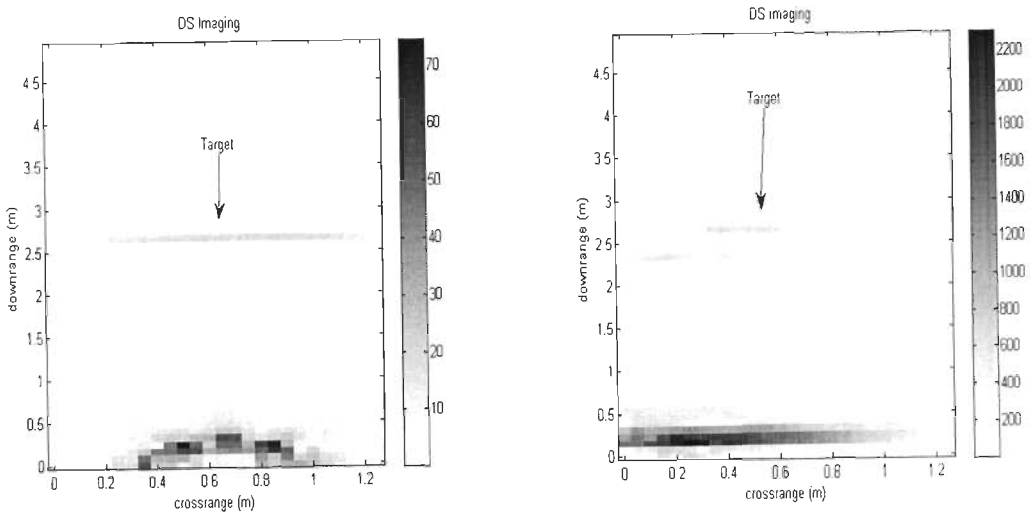

(a) (b)

Figure 5.5 Delay sum B-scan from A-scan locations (a) 14-15 (b) 1-26

From Figure 5.5(a), it can be observed that the target locus extent reduces when more than a single A-scan is used, similar to the back projection case. The target location also gets more precise. From the final image Figure 5.5(b), it is observed that using the complete B-scan, the target is localized more precisely behind the wall. The lateral extent of the target can also be obtained.

(a) *Explanation using a vertical grid along height using back projection*

To illustrate the concept of imaging, and the need for C-scan, a vertical grid has been taken as the scene to be imaged. The distance of the grid in the downrange direction has been taken to be equal to distance of the target from the TWI system. First, only A-scans have been 'back projected' on the grid. A-scans at target locations 2,5,10 and 25 are chosen for illustration purpose as they cover the entire range on the scanner along the azimuth direction. For Figure 5.6(a) and 5.6(d), the images formed are similar but the orientation of the high intensity area strip is changed, which is as expected because they correspond to TWI system locations 2 and 25, and the target lies to the right of the TWI system when it is at 2nd position and to the left of the TWI system when it is at 25th position. For Figure 5.6(b) and 5.6(c), the area which has high intensity is circular, as the TWI system and the target are almost in front of each other in the azimuth direction.

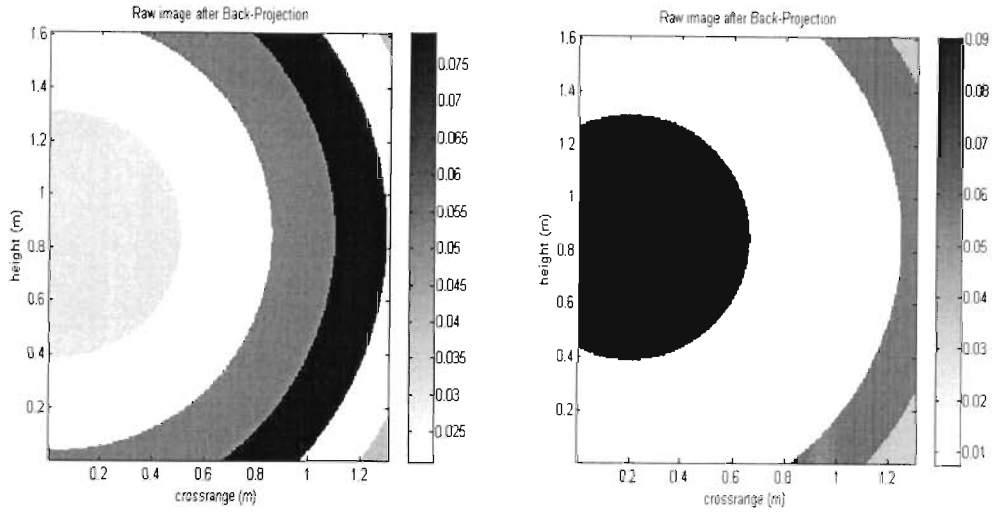

(a)

(b)

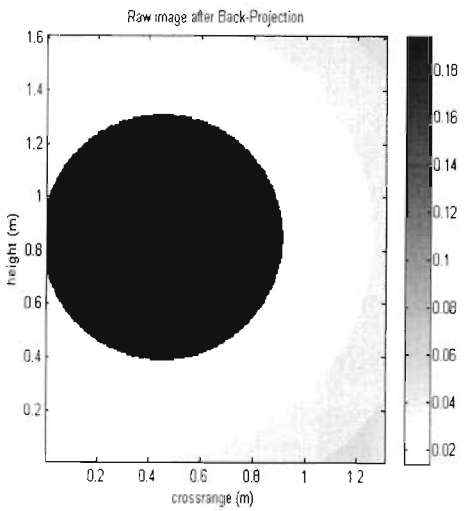

(c)

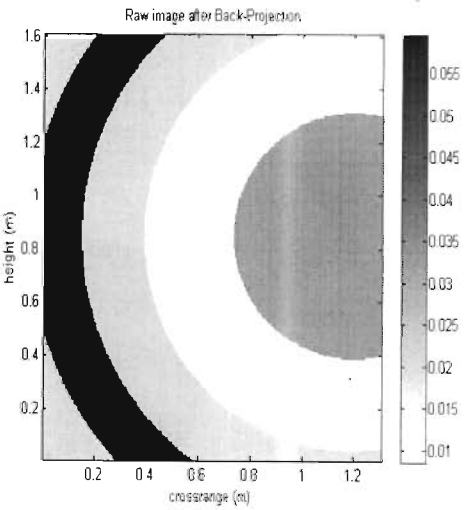

(d)

Figure 5.6 Images obtained using A-scan data for positions (a) 2, (b) 5, (c) 10, (d) 25

It was observed using a horizontal grid in the downrange-crossrange direction earlier, in Figures 5.1 through Figure 5.3, that using A-scan information, only detection of the target is possible, but the target cannot be localized precisely.

Figure 5.7 shows the B-scan image back projected on the vertical grid. The image has been generated using the complete B-scan data, comprising of 26 A-scans in the azimuth direction. The target's precise location in the azimuth direction as well as the lateral extent of the target can be obtained using this image.

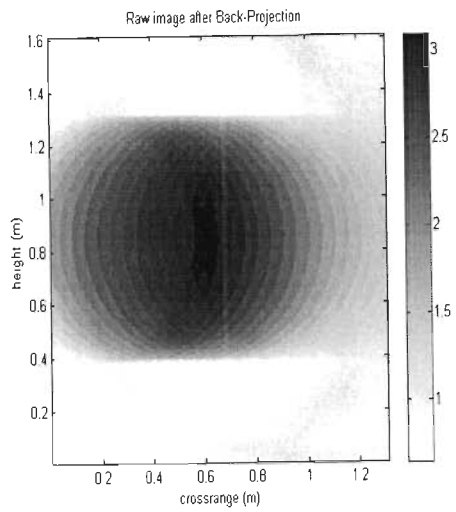

Figure 5.7 B-scan image on vertical grid

This is the same observation as was obtained for the case of horizontal grid in Figure 5.2. It should be noted that the vertical grid was created at the downrange distance corresponding to the target location since the information regarding the target position is available. The vertical grid was constructed to illustrate how imaging takes place and the target information is added as data is increased for imaging. If the target's exact extent along the height and shape of the 2-D target is desired, more data will be required. B-scans taken at different heights will be required, that is called as C-scan.

(b) *Explanation using a vertical grid along height using delay sum*

Vertical grid was constructed at the target's location in the down range similar to the back projection case. As can be seen from Figure 5.8 and Figure 5.9, the results obtained are similar to the back projection case. B-scan helps to localize the target in the azimuth direction and the target's lateral extent in the azimuth can be obtained. For determination of target's exact extent along the height and the target's shape, C-scan data may be more appropriate.

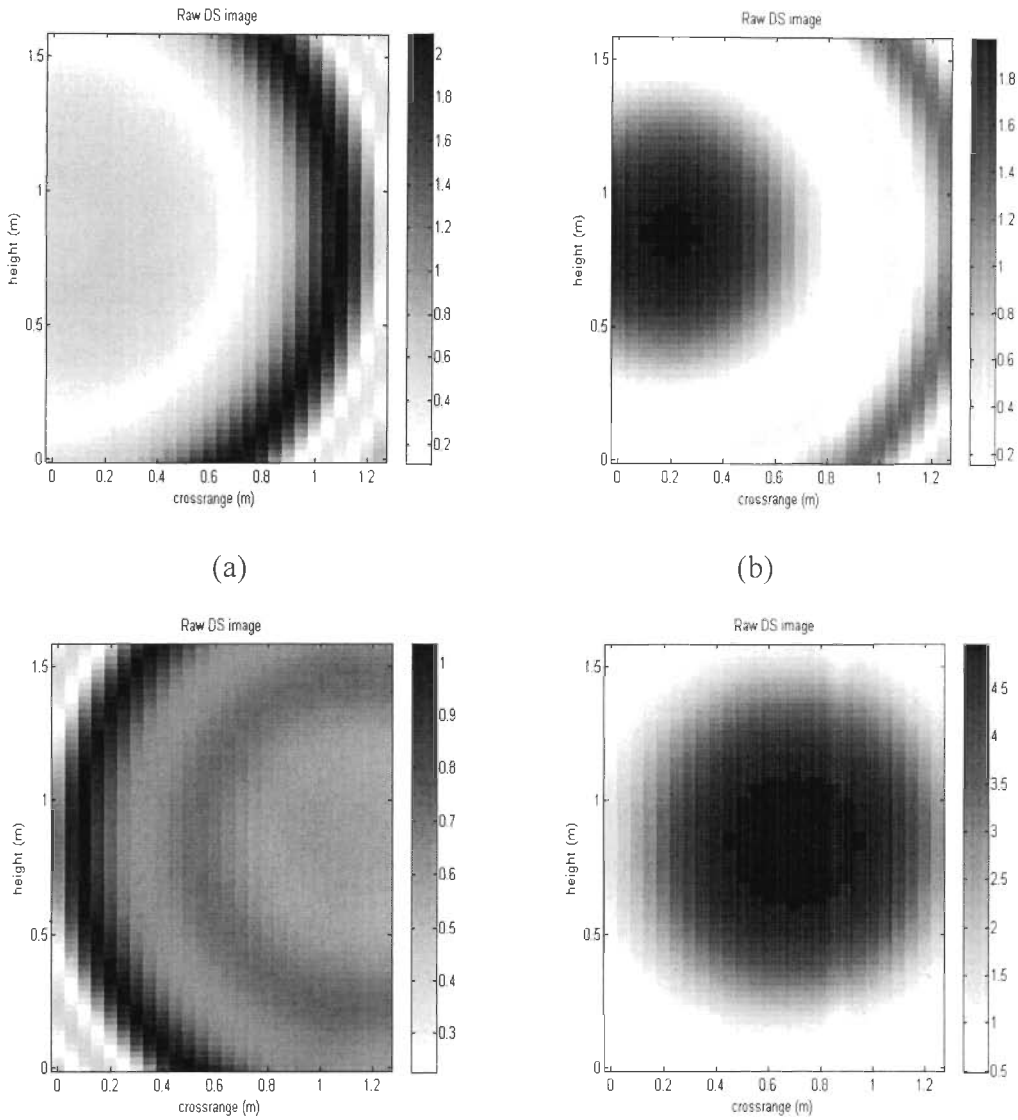

Figure 5.8 Delay sum (DS) images obtained using A-scan data for positions (a) 1 (b) 5, (c) 24, (d) 15

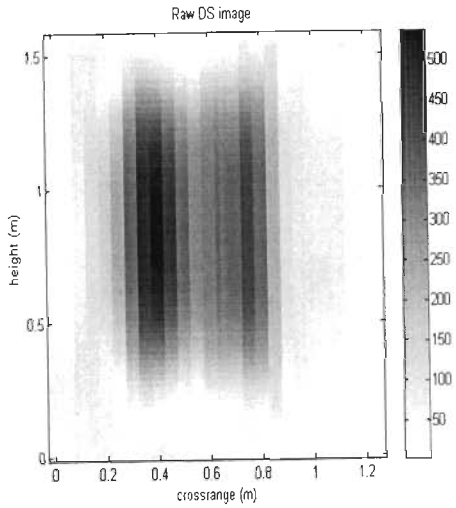

Figure 5.9 Delay sum images obtained using A-scan data for total positions

5.3 Different image formation techniques

Imaging algorithms are applied on TWI data after the data collection has been carried out. A synthetic aperture TWI system (SAR) model is used for data collection in monostatic mode in which single antenna at one location transmits and receives the signal and then moves to next location as shown in Figure 5.10. The data collected at different positions can be combined to produce image of target using different imaging techniques. The most widely used methods are ω-k, back projection and delay sum which are briefly discussed. Only B-scan data is considered for applying different imaging techniques.

Figure 5.10 illustrates the SAR model of data collection. Here x denotes the different positions of antenna. In SFCW TWI system, wideband signal is generated using step frequency approach in which system sweeps through the allocated signal bandwidth via a series of narrowband signals of uniformly spaced centre frequencies. Let Q be the number of narrow band signals and N be the number of antenna locations for data collection. TWI system measures the magnitude and phase of the received field for various frequencies at each spatial point. Assuming that the first starting frequency in SFCW TWI system is f_0 with a constant increment of Δf, the frequency of the q^{th} sample in the received sequence is given by equation (5.1).

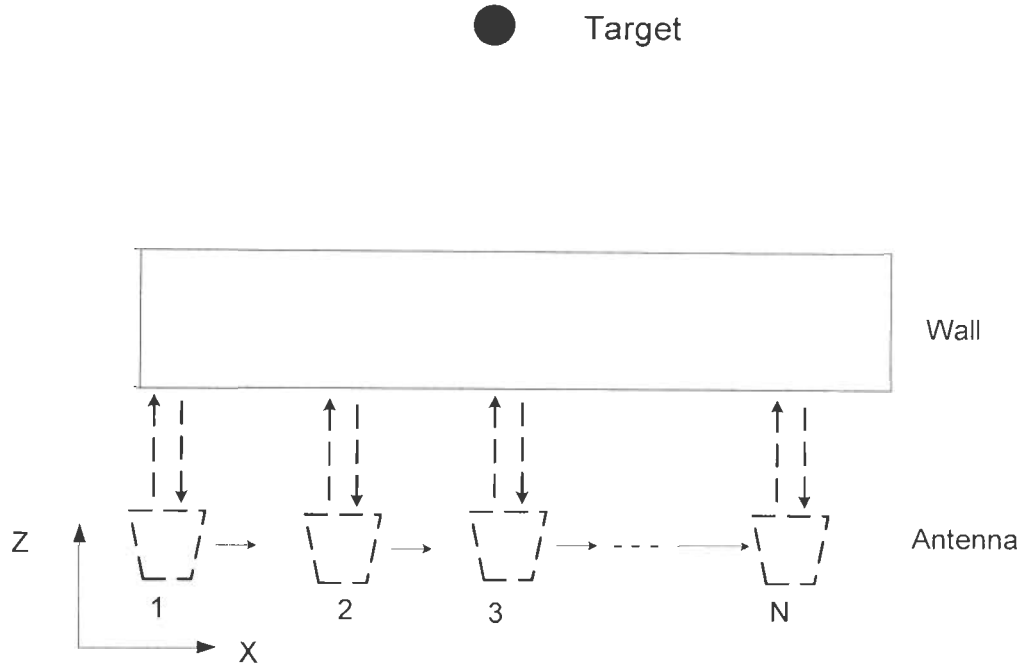

Figure 5.10 SAR model to collect data

$$f = f_0 + (q-1)\Delta f \quad q = 1,2,...Q \tag{5.1}$$

The signal received in frequency domain backscattered from the p^{th} point scatterer at distance d from the nth antenna location will have the form of

$$S(f) = \rho \exp(-j4\pi \frac{fd}{c}) \tag{5.2}$$

where ρ is strength of scattered electric field from the point target and c is the velocity of the electromagnetic wave in the propagation medium. Depending on the type of imaging technique, received signal is either converted into time domain or kept as it is in frequency domain. In B-scan, the signal is recorded at each synthetic aperture position to obtain image in space frequency matrix. After Fourier transformation this space frequency B-scan data is transformed to space time image. If the single point scatterer is present in imaging scene then hyperbolic curve is produced in resultant image. This low resolution feature may be corrected using different imaging techniques.

5.3.1 Frequency-wave number (ω-k) migration technique

Image formation using ω-k, which is modeled as convolution in spatial domain, is explained here. The signal received is represented in terms of wavenumber as [162, 244]

$$S(f) = \rho.\exp(-j2kd) \tag{5.3}$$

where $k = 2\pi f/c$ is the wave number vector of Q points. This static measurement at single spatial point is nothing but an A-scan measurement. B-scan data are obtained by collecting a series of A-scan measurement along X axis as shown in Figure 5.1. The scattered signal is summed for each discrete point as the TWI system antenna moves along a straight path. For a measurement point x_j on the X axis, the distance d from the point target at (x_0, z_0) to the TWI system is equal to

$$d = \sqrt{z_o + (x_j - x_o)} \quad j = 1,2...N \tag{5.4}$$

where N is total number of antenna position in B-scan.

So, the total received field can be given as below for point targets located at different (x_i, z_i) positions by assuming homogeneous wall, and is represented as equation (5.5)

$$S(x,f) = \sum_{i=1}^{P} \rho_i.\exp(-jk(2\sqrt{z_i^2 + (x - x_i)^2}) \tag{5.5}$$

Taking one-dimensional (1D) Fourier transform (FFT) of equation (5.5) along the x-direction, which will give the field in the spatial frequency k_x domain as

$$S(k_x,f) = \sum_{i=1}^{P} \rho_i.\int_{-\infty}^{\infty} \exp(-jk(2\sqrt{z_i^2 + (x - x_i)^2})).\exp(jk_x x)dx \tag{5.6}$$

By utilizing the principle of stationary phase, above integral can be solved as

$$S(k_x,f) = \frac{e^{-j\pi/4}}{\sqrt{4k^2 - k_x^2}} \sum_{i=1}^{P} \rho_i.\exp(-jk_x.x_i - j\sqrt{4k^2 - k_x^2}.z_i) \tag{5.7}$$

Here the ratio $e^{-j\pi/4}/\sqrt{4k^2-k_x^2}$ is the complex amplitude term and has a constant phase. Therefore, it can be neglected for image displaying purposes. Thus, equation (5.7) can be normalized as

$$\bar{S}(k_x,f)=\sum_{i=1}^{P}\rho_i.\exp(-jk_x.x_i-j\sqrt{4k^2-k_x^2}.z_i) \tag{5.8}$$

This is the received signal data in two dimension k_x-f domain and has a linear phase term in x and z. However, it is obvious that a total of P point scatterers should be ideally imaged in real coordinates as

$$s(x,z)=\sum_{i=1}^{P}\rho_i.\,\delta(x-x_i,z-z_i) \tag{5.9}$$

where $\delta(x,z)$ is the two dimensional impulse function. Now, taking the two dimensional Fourier transform of this image data with respect to x and z, following scattered field value in two dimensional spatial-frequency domain is obtained as

$$\bar{S}(k_x,k_z)=\sum_{i=1}^{P}\rho_i.\exp(-jk_xx_i-jk_zz_i) \tag{5.10}$$

Thus if the received data is transformed to k_x-k_z domain as in the form of equation (5.10), then focused-image data is obtained by taking two dimensional inverse Fourier transform of the data in k_x-k_z domain. It follows that when equations (5. 8) and (5.10) are compared with each other for accommodation, the transformation or spatial frequency mapping of $k_z=\sqrt{4k^2-k_x^2}$ must be done. Applying this critical mapping, one can get the equality

$$\bar{S}(k_x,k_z)=S(k_x,f) \tag{5.11}$$

This implies that one must relate values of $\bar{S}(k_x, f)$ at each f point to the values of $\bar{S}(k_x, k_z)$ at k_z points with the help of the frequency mapping equation of $k_z = \sqrt{4k^2 - k_x^2}$. On the other hand, when the field data in the $k_x - f$ domain is being transferred to the $k_x - k_z$ domain, the points that are evenly spaced in the f domain will be mapped to unevenly spaced points in the k_z domain due to the nonlinear behavior of the mapping equation. To exploit the fast computation opportunity using FFT, $\bar{S}(k_x, k_z)$ should lie on a uniform cartesian grid. Therefore, an interpolation procedure has to be applied in k_z domain to distribute data into a rectangular grid in k_x–k_z domain. Consequently, the final focused two dimensional B-scan image spotting the true locations of the target can be obtained by taking the two dimensional IFFT of equation (5.11) as

$$s(x,z) = \frac{1}{(2\pi)^2} \int_{-\infty}^{\infty} \int_{-\infty}^{\infty} \bar{S}(k_x, k_z).\exp(jk_x.x + jk_z.z))dk_x dk_z \qquad (5.12)$$

After summarizing B-scan algorithm, the flowchart for implementation of the algorithm as given in Figure 5.11 is discussed below:

i. Collect the B-scan back-scattered electric field $S(x, f)$ in the frequency domain

ii. Take one dimensional Fourier transform of $S(x, f)$ along x to get $S(K_x, f)$ and normalize it. (equation 5.7)

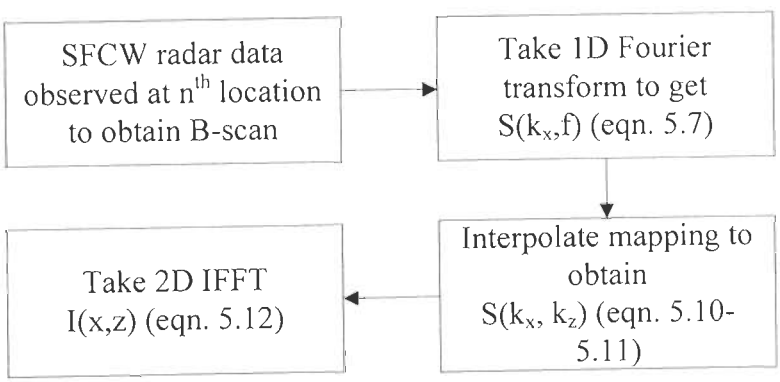

Figure 5.11 Flowchart for implementation of ω-k imaging

iii. Interpolate $S(x, f)$ on to a rectangular mesh in $k_x - k_z$ domain to obtain $\bar{S}(k_x, k_z)$. (equation 5.10- 5.11)

iv. Take two dimensional IFFT $\bar{S}(k_x, k_z)$ to form the final focused two dimension image; $s(x, z)$ in Cartesian coordinates. (equation 5.12)

Thus image formation, modelled as a convolution in the spatial domain, is performed in the wave number (k) domain. The k-domain inversion methods have the main advantage of exploiting fast Fourier transform (FFT) which provides significant computational savings.

5.3.2 Back projection

Back projection imaging algorithm is widely used in through wall imaging for image generation [91]. The back projection algorithm forms an image of target reflectivity as a function of position on a two dimensional map. Calculations are carried out in the space time domain, contrasting with the previous ω-k techniques employing Fourier transforms at the expense of processing time. Artifacts are localized; with noise levels lower than that of Fourier transform methods. Since FFTs require equally spaced data, any variation via off-track motion or changes in velocity will result in degraded images. Also, transmission through differing media such as an air wall dielectric result in propagation velocity differences, again difficult to handle in FFT based techniques. These can be compensated with back projection methods by a time shift. This method correlates the spatial coordinates of the transmit antenna, receive antennas and the pixels of the images to the range profiles of the receivers. The idea is to correlate data collected at each position as a function of round-trip delay time. Back projection coherently sums the sampled TWI system returns for each antenna position. Phase coherent summation is a process whereby the signal obtained at each aperture position is time shifted to match, or align, it to a particular pixel element in the image map. Following this, the responses across all aperture positions are combined.

To facilitate further, first define three related coordinate systems. These are object, data and image spaces, as shown in Figure 5.12. The object space $g(x, z)$ is the actual physical space illuminated by the TWI system. Although $g(x, z)$, the object space is

illustrated, this is essentially unknown from the perspective of the collected TWI system data. Here x denotes cross range, or azimuth, and z the range coordinates (Figure 5.12a). By collecting and processing TWI system data, one attempts to reconstruct an image of the objects contained within this area. Back projection can be explained as: consider a discrete set of P point-reflectors with reflectivity σ_p, (p = 1, 2 ...P). The location of each point is given by the spatial coordinates (x_i, y_j). Next consider a short-time (broadband) pulse $s(t)$ transmitted from a TWI system located at (u_n, 0), where n is the system platform position index (n = 1, ..., N) with a total of N positions in the array. Spatial separation between the nth system position and the pth point target is [15]

$$R_p(u_n) = \sqrt{z_p^2 + (u_n - x_p)^2} \tag{5.13}$$

In turn the round trip delay becomes

$$t_p(u_n) = \frac{2}{c} R_p(u_n) \tag{5.14}$$

$$t_p(u_n) = \frac{2}{c} \sqrt{z_p + (u_n - x_p)^2} \tag{5.15}$$

The return from a target located at distance $R_p(u_n)$ is therefore proportional to $s(t-t_p(u_n))$. Therefore the echo from the pth target is

$$s(u_n, t) = \sum_p \sigma_p s(t - \frac{2}{c}\sqrt{z_p^2 + (u_n - x_p)^2}) \tag{5.16}$$

Since a single TWI system receive antenna at position u_i cannot distinguish angle of arrival, the scattering center could be located anywhere on a cylinder surrounding u_i with radius

$$R_i = \frac{c}{2} t_i \tag{5.17}$$

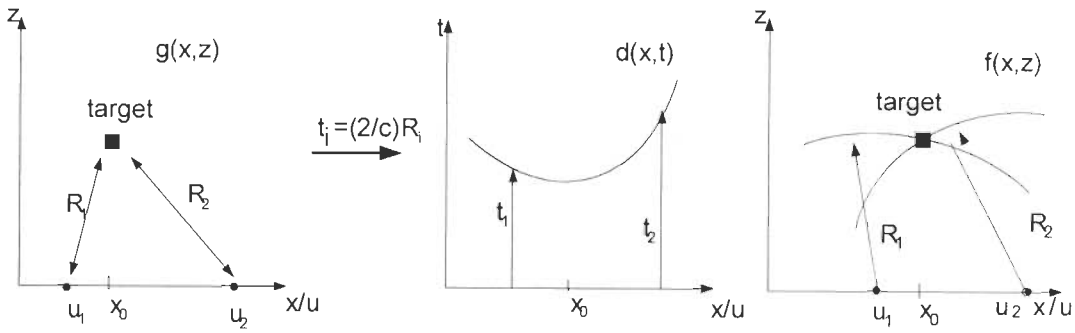

(a) (b) (c)

Figure 5.12 Coordinate systems used in imaging (a) Object space: $g(x, z)$ (b) data space: $d(x, t)$ (c) Image space $f(x, z)$

corresponding to time delay t_i. As the TWI system platform traverses, signals containing combined echoes from all targets are received at each x position. The collection of data over all element positions defines the data space,

$$d(u,t) = \sum_{n}^{N} s(u_n, t) \tag{5.18}$$

This is the data used to construct the image map $f(x, z)$. At this point it must be understood that $d(u, t)$ is not sampled directly. Instead, it represents the first step in image formation where individual data sets $s(u_n\ t)$, collected at each element are combined over the entire region of support forming the $x - t$ plane. In other words, each data set is sampled sequentially $s(u_n\ t)$, $s(u_{n+1},\ t)$, $s(u_{n+2},\ t)$ ....but they are aligned in data space based on return-time delay. In data space, the echoes for a given point target trace out a hyperbola due to the motion of the TWI system. The two-dimensional function representing this "spreading" of signal energy is called the point spread response (PSR). Figure 5.12(b) is a very simple representation of how a single target forms a PSR. The PSR acts as an impulse response in data space with respect to a point target in object space. For this reason, the curve is often denoted h (u, t). Energy contained within the PSR must be collected, or focused back to the original point function (Figure 5.12(c)). The "optimum" focusing of data is obtained by

correlating $d\ (u,\ t)$ with the PSR. In effect, a space-time domain matched filter is required with respect to $h\ (u,\ t)$. Obviously, coordinates of individual targets are unknown to form an image map; consider the set of 2D grid points (x_i,z_j). The impulse response is correlated with measured data to compute a measure of the reflectivity at that point:

$$f(x_i,z_j)=\int_u\int_t d(u,t)h^*[t-\frac{2}{c}\sqrt{z_j+(u-x_i)^2}\,dudt \tag{5.19}$$

The PSR is expressed here as a complex conjugate h^*, although for real quantities, this notation makes no difference. In practice, the correlation integral is not computed directly. Due to the incremental nature of both aperture positions and time samples, a two-dimensional discrete summation is performed. Further, a portion of the calculation requires interpolation since the recorded time samples do not correspond exactly to grid locations. There are N points along cross-range, and M points in the range dimension. This will produce an $N\times M$ pixel image of reflectivity. In short, a separate image map is constructed for each aperture position. As successive images (corresponding to individual element positions) are added, points where the arcs overlap tend to reinforce while the other regions fade into background noise and shadowing. Coherent summation then, is simply an instance of constructive interference. To obtain a focused image, each of the arrays is added pixel-by-pixel. In each step of summation the magnitude of signal increases. The overall behavior is that points corresponding to target locations are continually reinforced while other areas display low-value intensity, or shadowing.

(a) *Implementation of back projection on SFCW TWI system data*

Inverse Fourier Transform has been carried out on data obtained at each antenna position to produce range profile. For each pixel in the desired image-map the propagation range from TWI system to the pixel and then back to the TWI system is calculated and used to index into the range profile to find value of the in phase and quadrature components of the scattered field from that range. The values of the scattered fields from all the TWI system positions are summed for each pixel in the image- map. Where there are objects in the image that result in scattering, the

individual observations from the TWI system will be in phase and sum to a large value. If there is no target, the individual observations will be out of phase and tend to sum toward zero. The magnitude of summation depends on TWI system cross section of scattering objects and the distance from TWI system.

In short the flowchart of back projection algorithm is given in Figure 5.13 and the steps are as follows,

1. Divide the whole region into small pixels.
2. For each pixel, calculate the flight time from TWI system to pixel and pixel to TWI system.
3. Record the corresponding received time bin amplitude for each pixel after converting received frequency domain data of SFCW TWI system into time domain using IFFT.
4. Repeat step 2 and 3 for all position of TWI system. Sum the recorded amplitudes on the spatial grid.

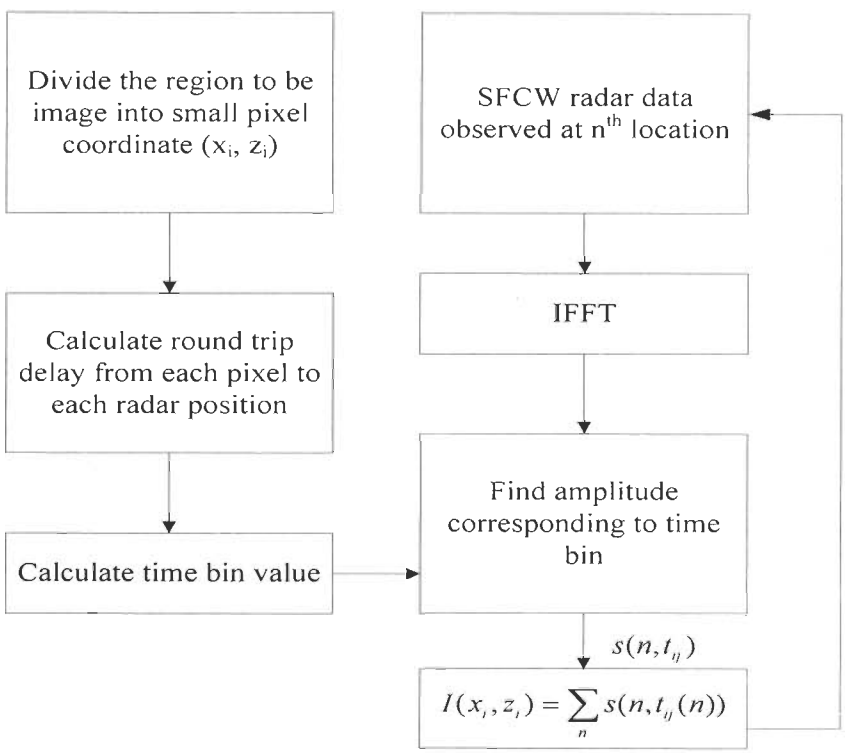

Figure 5.13 Flow chart of Back projection algorithm

5.3.3 Delay sum

Imaging technique is applied on frequency domain data received through SFCW TWI system. The signal received at one of the antenna location is given by

$$s(n,t) = \sum_{p=0}^{P-1} \sigma_p s(t - \tau_{n,p}) \tag{5.20}$$

where $s(t)$ is the transmitted signal, σ_p is the reflection coefficient of pth target and $\tau_{n,p}$ is the two way travelling time between the nth antenna and the pth target.

If there is no wall, the signal path between the antenna and the target will constitute the line of sight. In this case

$$\tau_{n,p} = \frac{2}{c}\sqrt{(x_p - x_n)^2 + (z_p - z_n)^2} \tag{5.21}$$

where c is speed of wave propagation and (x_p, z_p) and (x_n, z_n) are the location of the pth target and nth antenna respectively. When a solid homogeneous wall is present the signal path can be computed using both dielectric constant and the thickness of the wall [4]. The delay sum (DS) imaging is relatively simple and robust image formation method for TWI. The value for the pixel located at (x, z) is given by:

$$I(x,z) = \frac{1}{N}\sum_{n=0}^{N-1} s(n, t + \tau_{n,(x,z)}) \tag{5.22}$$

where $\tau_{n,(x,z)}$ is the two way travelling time through the air and wall between the nth antenna and the (x, z) pixel position. With the transmitted signal chosen as stepped frequency waveform consisting of Q narrowband signals, equation 5.22 becomes,

$$I(x,z) = \frac{1}{N}\sum_{n=1}^{N}\sum_{q=1}^{Q} S(n, f_q)\exp\{-j2\pi f_q \tau_n(x,z)\} \tag{5.23}$$

where $S(n, f_q)$ is the signal received at the nth antenna at frequency f_q. Various steps for implementation of algorithm are given in flowchart shown in Figure 5.14.

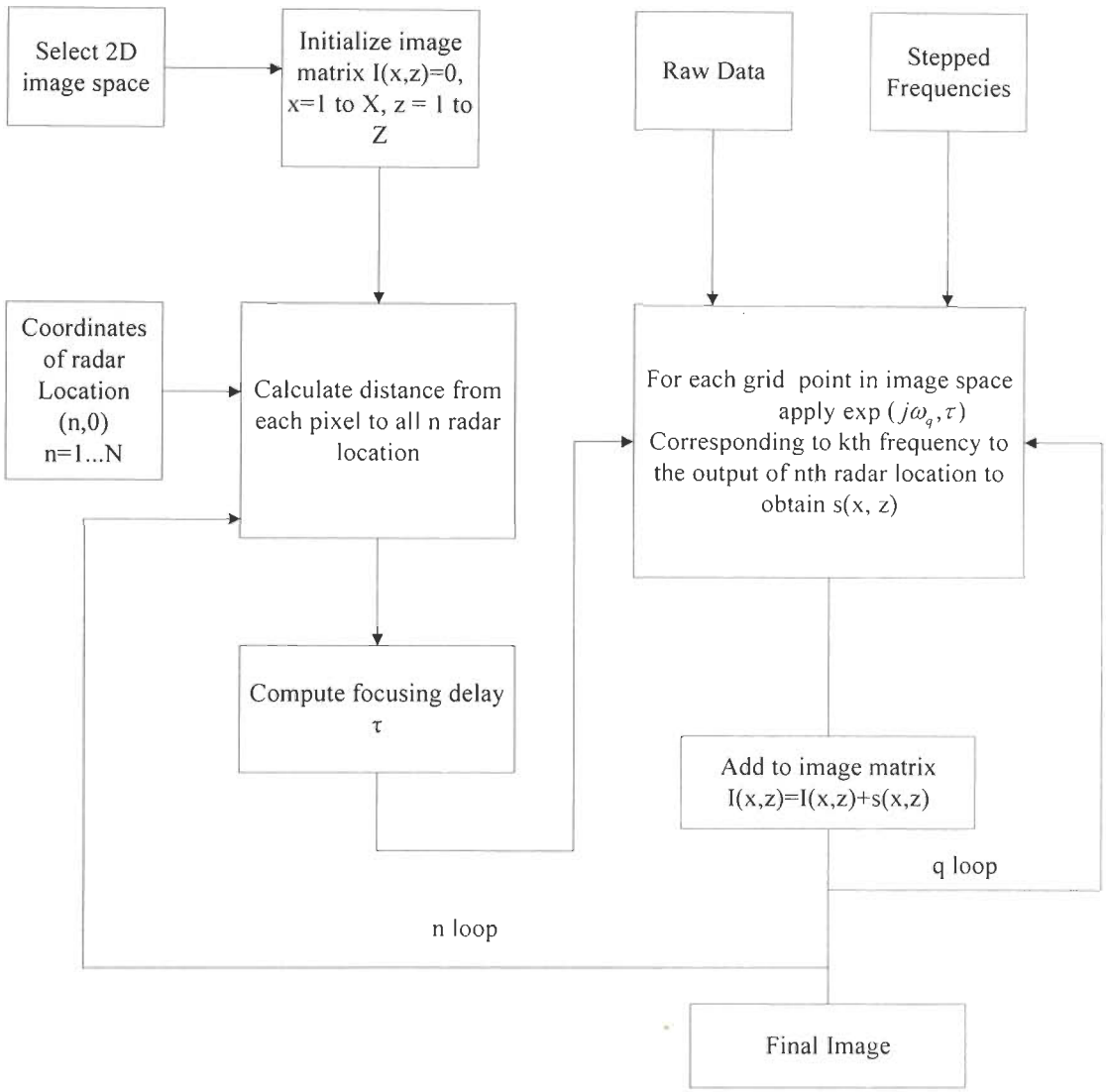

Figure 5.14 Flowchart of delay sum

Steps for implementation of the delay sum algorithm as given in Figure 5.14 are:

- Select the 2D image space and divide the region to be imaged into pixels.
- Calculate the distance from TWI system locations to each pixel location.
- Calculate the focusing delays using the calculated distance values. (equation. 5.21)
- For each pixel value, apply the focusing delay to the raw SFCW data for each frequency point obtained at a particular TWI system locations.
- Sum the terms for individual point for all frequency points.

- Add the summation of terms corresponding to different frequency points to the image matrix. (equation 5.23)
- Repeat the above three steps for all the TWI system locations to obtain the final image matrix.

5.4 Comparison of different imaging techniques

The quality of image formation technique is checked by measuring metrics as given below. If the process of formation of image is not coherent, distortion occurs. Several criteria have been used to measure image quality in the literature [7]. Following two metrics are used to measure quality for TWI. Both the metrics used are contrast based metrics. Contrast based metrics have been chosen because for TWI images, if good contrast is present between the pixels corresponding to the target and the background pixels not corresponding to the target, the target detection becomes easier. If the contrast is not good, target detection becomes difficult and the exact extent of the target might not be clearly visible.

5.4.1 Metric 1: Negative of image entropy

The negative of the entropy of the image is defined as [7]

$$Metric1 = \sum_{q=1}^{Q} ss(x_q, z_q)\log(ss(x_q, z_q)) \tag{5.24}$$

where

$$ss(x_q, z_q) = \frac{\left|I(x_q, z_q)\right|^2}{\sum_{q=1}^{Q}\left|I(x_q, z_q)\right|^2} \tag{5.25}$$

where $I(x_q, z_q)$ represents q^{th} image pixel value and Q is total number of pixels in image. It can be seen that the value of this metric will vary from 0 to – (log (Q)). The upper bound (–(log (Q))) is achieved when all the pixels have the same intensity value. The lower bound of zero will be achieved when only one pixel value is non zero. The closer the value is to zero, the higher will be the contrast in the image.

5.4.2 Metric 2: Ratio of standard deviation to mean

This metric is defined as [7]

$$Metric\,2 = \frac{\sqrt{\sum_{q=1}^{Q}\left(\left|I(x_q,z_q)\right| - \frac{1}{Q}\sum_{q=1}^{Q}\left|I(x_q,z_q)\right|\right)}}{\sum_{q=1}^{Q}\left|I(x_q,z_q)\right|} \tag{5.26}$$

As this metric is the ratio of standard deviation to mean, the higher value it achieves, the better will be the contrast in the image which is desirable.

Both the metrics defined above measure the contrast of the image. A good measure of the contrast would be one for which the contrast reaches a maximum value only for undistorted image. Maximization of metric 2 will ensure good image quality.

5.5 Results and discussion

In order to test the image formation algorithms, B-scan data is used to generate the images. In this section, three different B-scan observation data are selected to see the performance of imaging algorithms. In the first observation, plywood wall is used for analysis (Table 1.2, S. No. 1). In second analysis, instead of plywood wall, brick wall data is used to see its effect on imaging (Table 1.2, S. No. 4). In the last, detection of two targets is checked using different imaging techniques using data described in Table 1.3, S. No. 3 and the results are compared using the contrast measures described above using equations 5.24 and 5.26.

5.5.1 Single target behind plywood

In the first observation a metal plate of 0.55 m × 0.60 m with thickness of 2mm is placed behind plywood wall. The B Scan data used for application of various imaging algorithms is collected as explained in Chapter 1.

Then by taking the 1D IFFT of this measured frequency data 1D range profile is obtained. Then one can easily construct a 2D B-scan image in spatial time domain by

putting all range profiles side by side. After applying preprocessing techniques as described in Section 1.3.4, B-scan image as shown in Figure 5.15 (a) is obtained. This type of formation of image is not coherent. Instead of this different focusing methods as presented above are applied on measured B-scan data. It is seen from all B-scan images obtained through imaging reasonable focusing is achieved compared to normal B-scan image (Figure 5.15). After applying ω-k algorithm, back projection and delay sum, the focused images as depicted in Figure 5.15 are obtained.

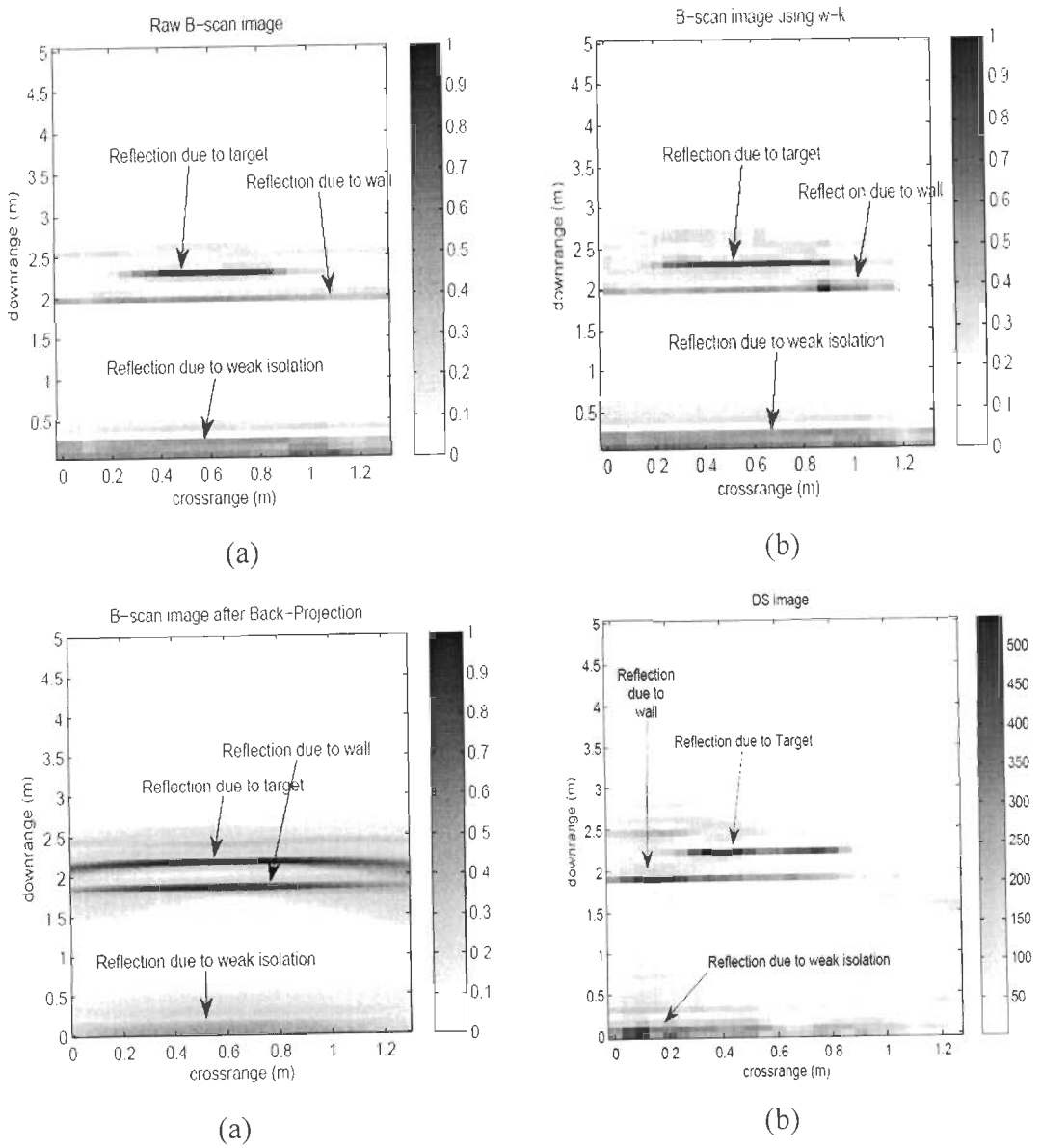

Figure 5.15 (a) Raw B-scan image and image after implementation of (b) ω-k (c) back projection (d) delay sum

Table 5.1 Plywood wall single target

Sr. No.	Measure	ω-k	BP	DS
1	Metric 1	-5.8221	-9.8823	-5.6017
2	Metric 2	0.1284	0.0164	0.1363

As discussed in Section 5.4, values obtained for both the metrics are shown in Table 5.1. Both metrics value are the maximum for delay sum that means delay sum is better than all other techniques. The next technique is ω-k as values obtained by delay sum are very close to the values obtained for ω-k algorithm. Figure 5.16 represents B-scan images obtained using different imaging technique after application of ICA clutter reduction technique. Then, the target reflection is well enhanced and concentrated around the exact locations in all images. The image quality of different algorithm can be visibly observed from results. The ω-k domain SAR focusing method and delay sum give more effective results than Back projection as observed from Figures 5.16.

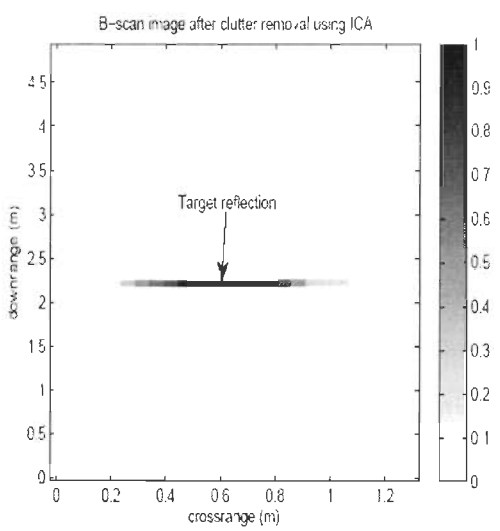

(a)

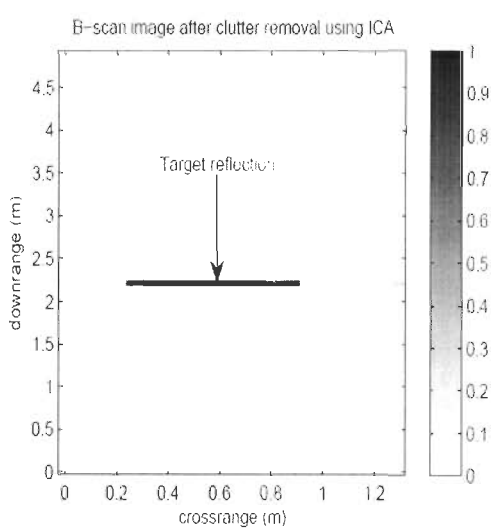

(b)

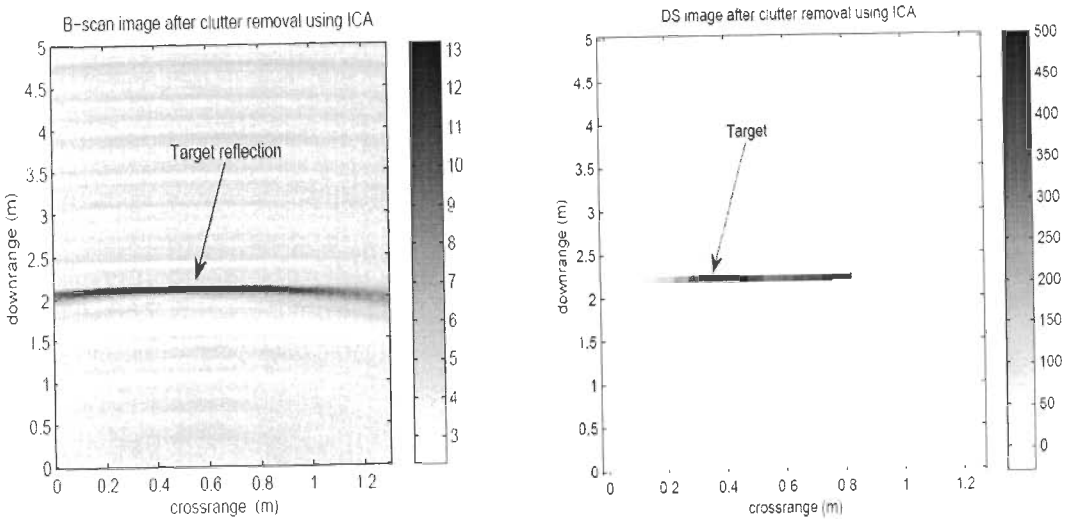

(c) (d)

Figure 5.16 B-scan image after clutter reduction (a) Normal and, after implementation of (b) ω-k (c) back projection (d) delay sum

5.5.2 Single target behind brick wall

Similar observations are taken when instead of plywood wall brick wall is used. A metal plate of 0.55 m × 0.60 m with thickness of 2 mm is placed behind brick wall at a distance of 0.3 m. After applying ω-k algorithm, focusing image as depicted in Figure 5.17 (a) is obtained.

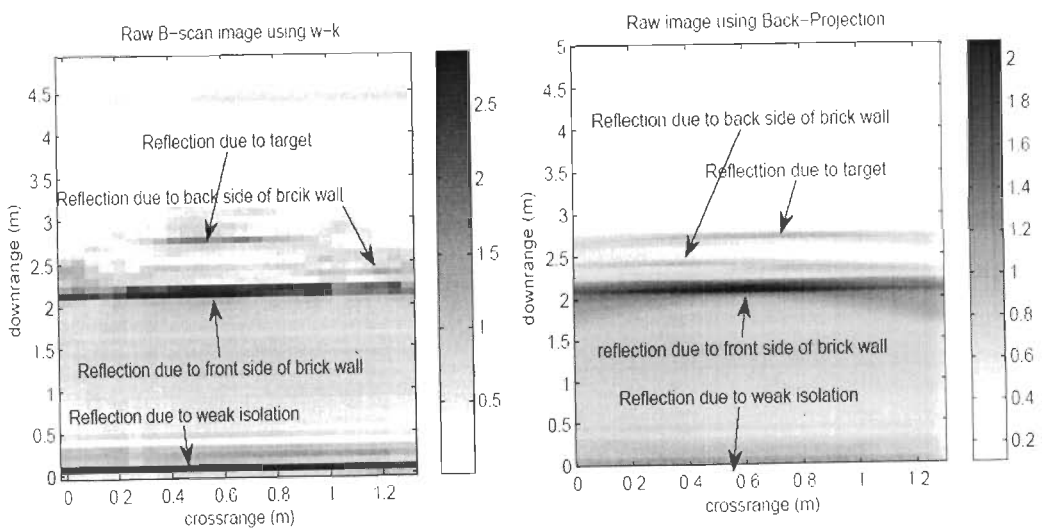

(a) (b)

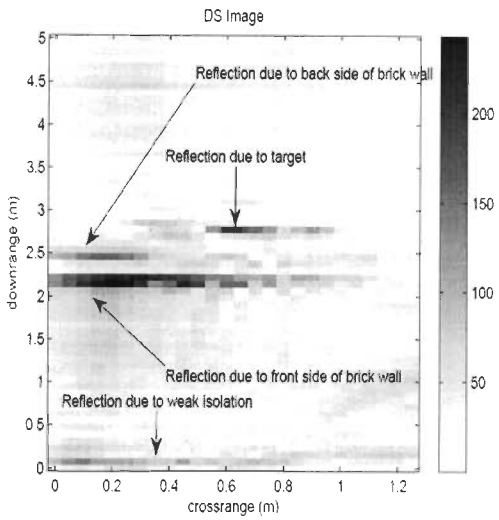

(c)

Figure 5.17 Raw B-scan image after implementation of (a) ω-k (b) back projection (c) delay sum

Table 5.2 Brick wall single target

Sr. No.	Measure	ω-k	BP	DS
1	Metric 1	-6.3764	-10.2280	-6.1976
2	Metric 2	0.0739	0.0134	0.1217

It is observed that the scattered energies are more concentrated around the respective scatterer that is reflection due to weak isolation and reflection from front of wall, reflection from wall and a weak reflection due to target. Similar observations can be made from Figures 5.17 (b) and 5.17 (c).

The values of both the metrics are best for delay sum but are again very close to the values obtained for ω-k as observed from Table 5.2. Figure 5.18 represents B-scan images obtained after applying clutter reduction technique using ICA. The ω-k domain SAR focusing method and delay sum again give more effective results than Back projection as can be visibly observed from Figures 5.18.

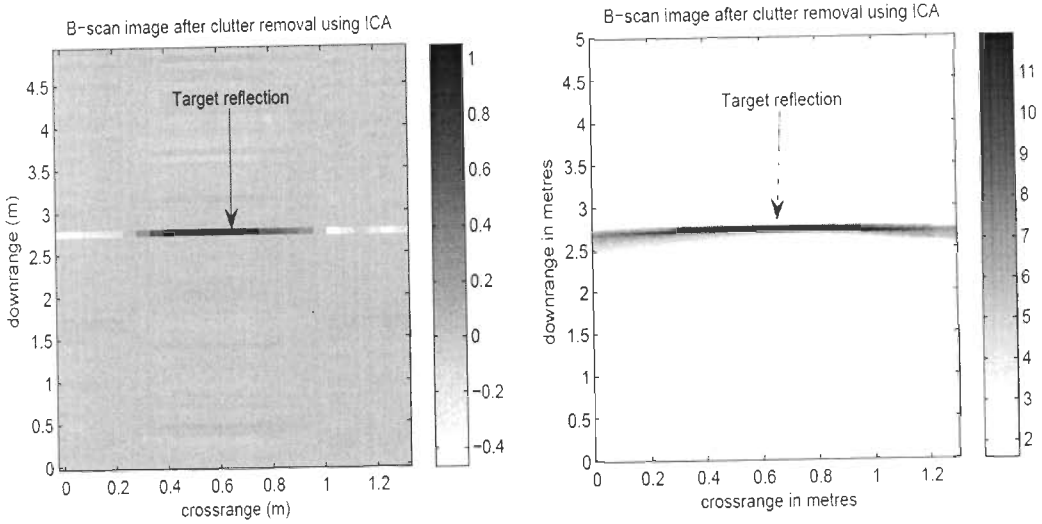

(a) (b)

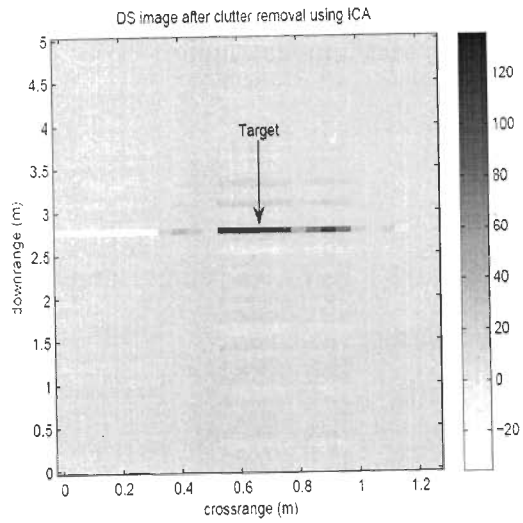

(c)

Figure 5.18 B-scan image after clutter reduction and implementation of (a) ω-k (b) back projection (c) delay sum

5.5.3 Double target behind brick wall

The data corresponding to S. No. 3 in Table 1.3 is used for the case of double targets behind the brick wall. Raw B-scan images are generated using different image formation algorithms, i.e. ω-k , Back projection and delay sum algorithm as shown in Figure 5.19. For the images generated using different imaging algorithms, values for both the metrics described above are calculated and the results are compared.

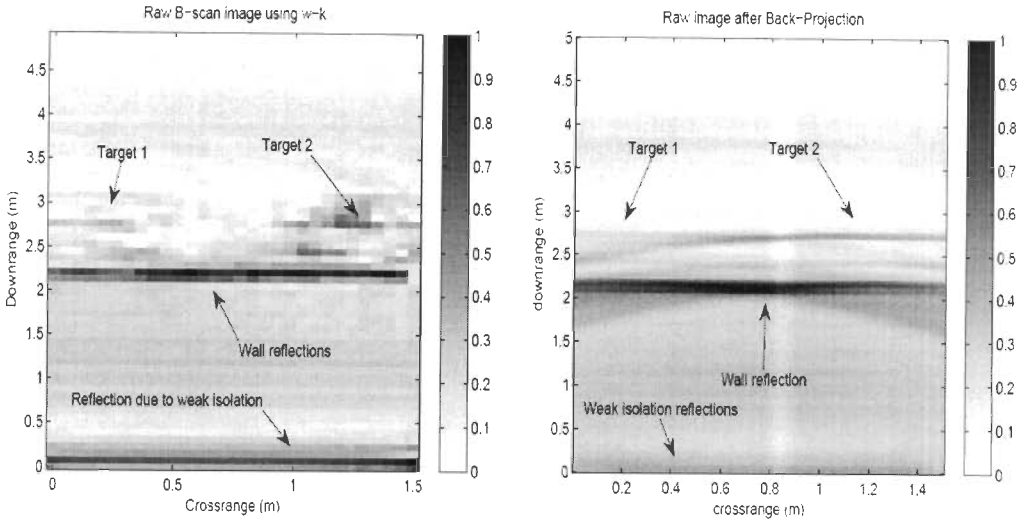

(a) (b)

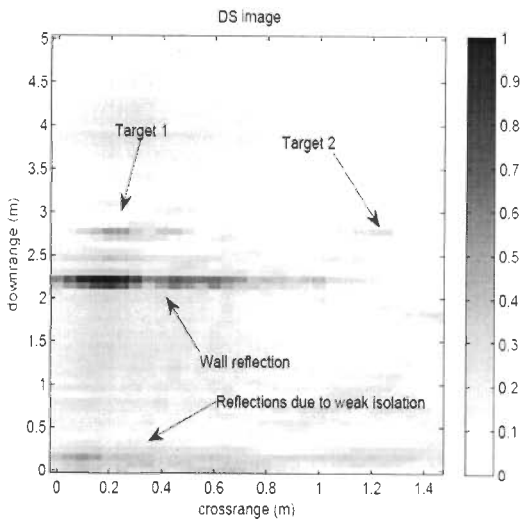

(c)

Figure 5.19 Raw B-scan images for double target case after implementation of (a) ω-k (b) back projection (c) delay sum

Table 5.3 Brick wall double target

Sr. No.	Measure	ω-k	BP	DS
1	Metric 1	-6.6514	-10.45	-6.4691
2	Metric 2	0.0762	0.0113	0.1383

The values obtained for both the metrics are as shown in Table 5.3. The values of both the metrics are best for delay sum but are very close to the values obtained for ω-k for

the double target case also. Clutter reduction is also applied and the values for both the metrics are calculated for images formed using different imaging algorithms. The ω-k domain SAR focusing method and delay sum again give more effective results than Back projection as can be visibly observed from Figures 5.20.

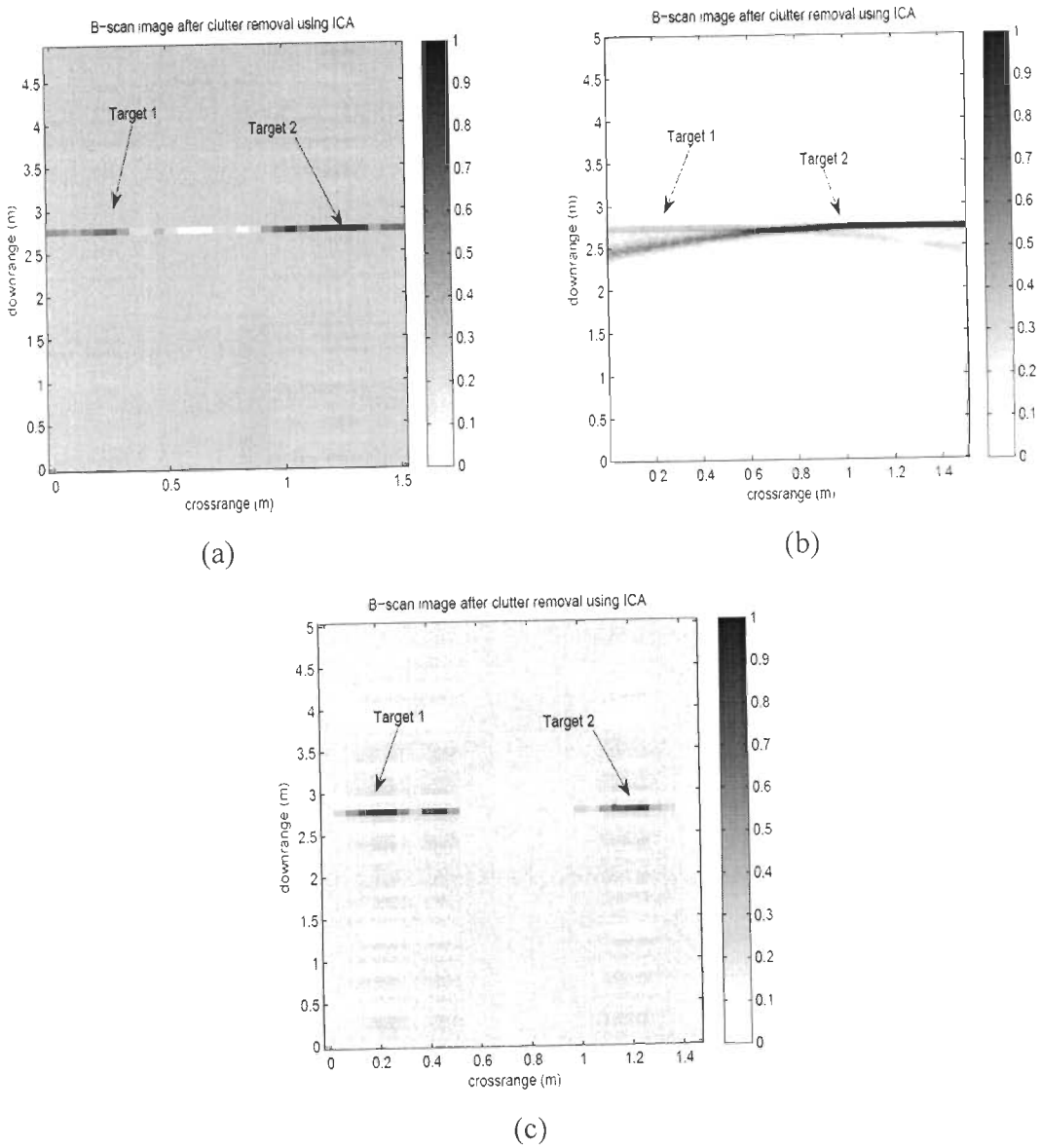

Figure 5.20 B-scan images for double target case after clutter reduction and implementation of (a) ω-k (b) back projection (c) delay sum

5.6 Concluding remarks

Different imaging techniques have been applied on TWI data. A comparison of obtained images has been carried out using different metrics. The algorithms are tested with the experimental data. Measured B–scan images of metallic target after applying the algorithm demonstrate the performance of the methods.

Three different coherent image formation techniques are studied for through wall application. As coherent imaging uses many spatial antenna positions, target information is increased. The image quality of different algorithm can be visibly observed from the obtained results. There is a considerable difference between the output images of algorithms from the focusing point of view. Drawback of back projection method is that it produces ghost tails from the focused point as observed from results. ω-k method better focuses the target signature compared with back projection. Therefore the energy level in final focused image will not correspond to true energy levels of each reflection. This can be seen from the images obtained for double target case. The values of both the metrics, which are a measure of image contrast, are best for delay sum, closely followed by ω-k algorithm for all the cases.

Due to the use of FFT, faster formation of desired image is possible. But when multiple targets are present artifacts are produced. Back projection technique is advantageous when large synthetic aperture and large bandwidth is used compared to ω-k in which problem is faced for mapping and interpolation. In conclusion, delay sum algorithm gives the best results and ω-k closely follows. However, the processing time required for the delay sum algorithm is high as compared to the ω-k algorithm.

Chapter 6

Application of pattern analysis techniques on TWI data for target shape recognition

6.1 Introduction

The aim of this chapter is to explore the possibilities of feature extraction techniques for shape detection. B-scan image provides the information in cross range and down range where hight and size of the target can not be obtained. To recognize target and its complete image, height information of target is very much required. C-scan data can be use to obtain a good three-dimensional (3D) images [8]. Here in this chapter instead of using C–scan data for three dimensional image formations, two dimensional image is obtained from it. This will reduce time complexity of imaging algorithm.

To enable reliable recognition of targets based on shape, the essential information must be extracted from the obtained image. This essential information form features

of the target. Feature extraction is the process of mapping target shape to number of coefficients, which in some sense represents the target shape. Features for two different targets should differ as much as possible. The feature should thus extract the information from the target that is essential for determining the shape of target. It is also desirable that features should have certain invariance properties, such as time shift invariance, invariance to scaling, insensitive to multiple reflections and to noise also. Some of feature extraction techniques which are used in TWI are reviewed in Chapter 2 where researchers have used first order and second order statistics such as mean, standard deviation, entropy, contrast [138]. PCA is used as feature for object recognition [143].

In this chapter feature based algorithm for shape detection is proposed to discriminate the target which will be useful to differentiate the targets. To recognize target shape, features are extracted using region based, contour based and pattern based techniques. From region based methods, moment based descriptor is used to describe shape [139]. Contour shape representation includes global shape descriptor from which Fourier descriptor is selected. Global shape descriptors are very in-accurate shape descriptors. Pattern generation [196] along with Fourier descriptor and moment descriptor are used as features of image. The main purpose of this chapter is to obtain a C-scan image of a target and recognize its shape. The shape may be recognized by two way (i) by visualization, where shape of target can be observed and (ii) Quantitatively, where features of different shape may be obtained and further it use for detection of shape. In this chapter, focused is on feature based shape recognition technique by which regular shapes like circle, rectangle and square may be detected. Orinetation of the regular shape targets were parallel to wall. Rotation of target is not considered.

The chapter is organised in following way. The methodology used in this paper is described in Section 6.2. In Section 6.3, C-scan imaging algorithm has been described with all the different signal processing steps required to enhanced the image. Section 6.4 describes different feature extraction techniques used for recognition of targets. The results are discussed in Section 6.5. Section 6.6 presents conclusions.

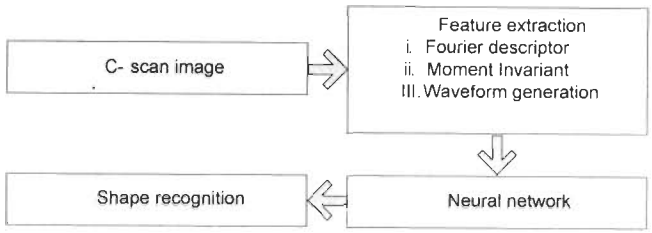

Figure 6.1 Flowchart for target shape recognition

6.2 Methodology

The developed methodology consists of image formation using C–scan data and use of different features with neural network for automatic shape recognition. Figure 6.1 gives the methodology to recognize target. According to flowchart, first the C–scan image is obtained, and then features are extracted using different techniques. The primary aim is formation of 2D image from C-scan data.

Feature extraction reduced the image data to a lower dimensional data space which represents the salient features of images. These features are obtained for different target shapes and used as input to neural network.

6.2.1 C–scan image formation

C-scan image is obtained from the ensemble of B-scans, measured by repeated line scans along the plane as described in Chapter 1 (Figure 1.5). The algorithm to obtain image with different processing steps are described with the help of flow chart in Figure 6.2. The algorithm can be describes as,

- B-scan image according to Equation 3.1 is obtained at each vertical height i.e. after clutter reduction obtained B-scan image is taken as first step.
- After applying thresholding technique all the B-scan images are stacked.
- The spatial grid will consist of number of vertical scanning position × number of horizontal scanning positions.
- At each grid point the region of interest is decided from which peak value at that position will be the placed.

- Since the image formed will have $X \times Y$ pixels, this will be a low resolution image.The image resolution is increased by the interpolation. Shape-preserving (pchip) interpolation is used.

Formation of B-scan image after preprocessing steps and clutter reduction techniques are described earlier in Section 1.3.4 and Chapter 3 and therefore are not discussed here. Thus in other words, the two dimensional image from C-scan data is formed by taking a fixed target plane ($z = z_{target}$) which is selected by observing range profile. The peak data value at target location is selected. Raw two dimensional image obtained from C–scan data is plotted by taking a fixed target plane ($z = z_{target}$) which is expressed by (6.1)

$$I\left(x, y, z = z_{target}\right) = \sum_{k=1}^{K} S(f_k)\exp\{j2\pi f_k(2z/c + 2z_{shift}/c + 2D_{wall}(\sqrt{\varepsilon_{rwall}} - 1)/c)\} \tag{6.1}$$

where x is antenna scan position in horizontal direction and vary from 1 to X and y is antenna scan position in vertical direction and vary from 1 to Y.

C–scan data are highly subjected to degradation due to the fact that antenna beam width is not focused. Due to presence of wall, two dimensional image which is obtained is not optimal from point of view of target recognition. Thus the user or operator will face the problem of proper interpretation of image. Image enhancement techniques are required to improve the raw C-scan image. This will help user to discriminate between different targets.

In processing, filtering, thresholding and edge detection techniques are applied to enhance the detection and visualization [197]. Shape preserving filter is required to remove undesired components from the raw image. Filtering techniques enhances the image and provides the smooth transition across the edges of target. Due to the swath of antenna the illumination area of antenna is not limited to the pixel size of the image so there is significant contribution from the neighbouring pixels [57]. In order to minimize the effect of overlap of the scattered field from neighbouring pixels convolution kernel filter is applied to image. The basis of the method of target detection is thresholding algorithm which is described in Chapter 4. For edge detection simple Sobel operator is used. This process detects outlines of an object and boundaries between objects and the background of the image.

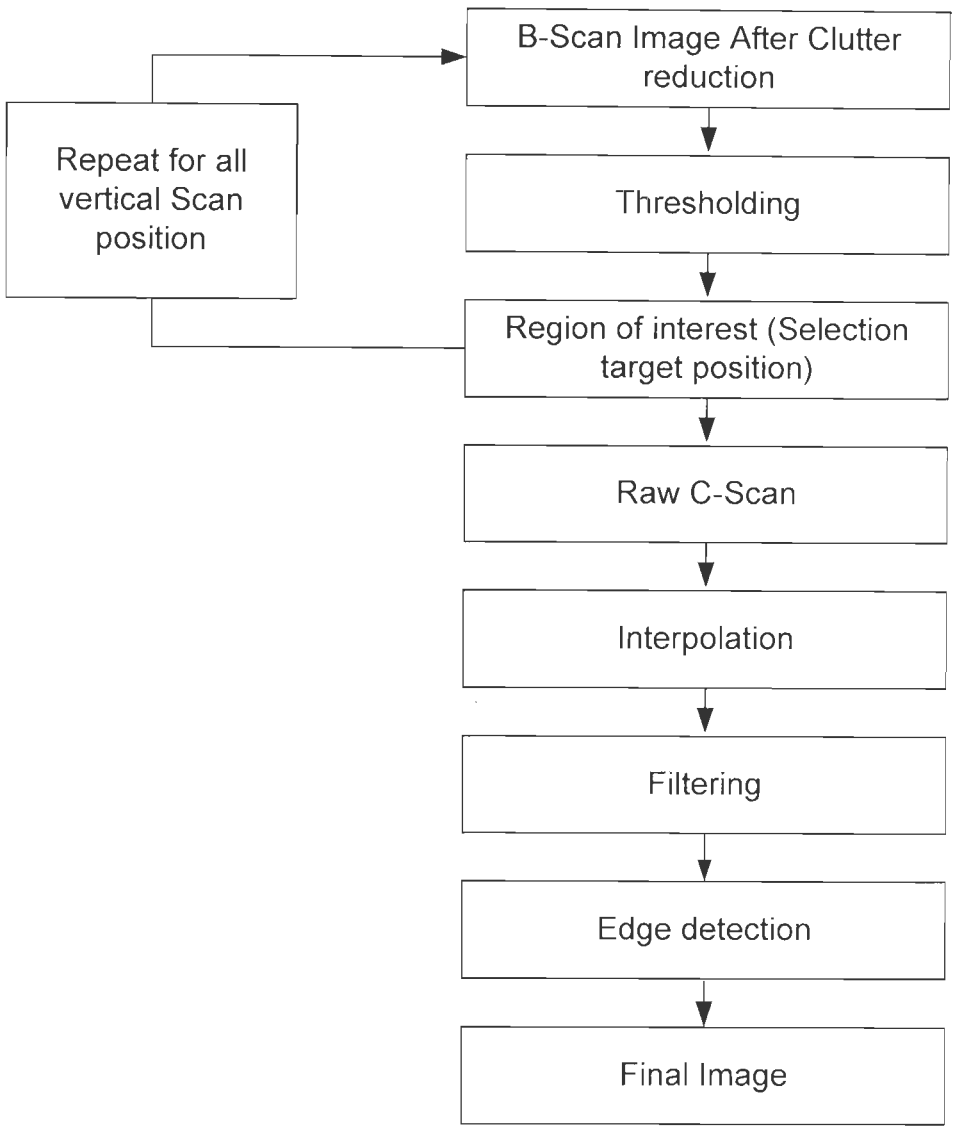

Figure 6.2 Flowchart showing the C-scan imaging algorithm

Sobel operator are used because they are products of multiplication of a one dimensional differential filter and one dimensional low pass filter. Differential filter is required to find edge and low pass filter provides smoothing effect.

6.2.2 Feature extraction techniques

To recognize target shapes, features that gives description of target is required. Since target is a collection of pixels in image, target description will be just numbers known as descriptors. Recognition of target can be achieved by comparing and matching the

descriptors of target in image with descriptors of known image. Descriptors should have four important properties.

- Two targets must have same descriptors if their shape is same.
- If similar descriptors are obtained then it should be recognized it as similar objects.
- Descriptors should have invariant properties w.r.t., scaling, position, rotation and also invariance to affine and perspective changes.
- Descriptors should contain information that makes target unique or different from other objects.

Also number of features which describes objects should be less than the complete information of objects. Unfortunately there are no set of complete and compact descriptors to characterize objects. Since single descriptor for recognition is not efficient, combined features can be used. In this chapter, features of targets are extracted using region and contour based descriptors along with pattern generation techniques. From region based methods, moment based descriptor is selected to describe shape. Contour shape representation includes global shape descriptor from which Fourier descriptor is selected [139]. Brief description about this techniques is given below.

(a) *Fourier descriptor*

In 1972, Granlund introduced the concept of complex Fourier descriptors in which the boundary of a target is defined based on complex Fourier coefficients. This Fourier coefficients are called Fourier descriptor. Fourier descriptor essentially gives set of spatial frequencies that fits the boundary points. With these descriptors one can identify the original image depending upon the number of frequencies being used. Ten percent of the Fourier descriptors are able to generate approximate plot of the image. When very less Fourier descriptors are used, the recognition performance degrades. The obtained Fourier coefficients are translation invariant due to transformation. Further the coefficients are normalized to make them rotation, scaling and start point independent. Fourier descriptors derived for different shapes are significantly different from each other due to which it can be used in shape recognition. The detailed explanation can be obtained from [139]. If the boundary

trace of shape is taken then a pair of one dimensional waveforms *x(t)*, *y(t)* can be generated. If *N* samples of a closed boundary are taken then,

$$u(n) = x(n) + jy(n) \quad n = 0,1,...N-1 \tag{6.3}$$

This will be periodic with a period *N*. Its discrete Fourier transform representation is

$$f(k) = \sum_{n=0}^{N-1} u(n)\exp(\frac{-j2pikn}{N}), \quad 0 \le k \le N-1 \tag{6.4}$$

The complex coefficients *f(k)* are called the Fourier descriptors of the boundary. Only the magnitudes of the Fourier coefficients have been used as features.

(b) *Moment invariants*

Moment in image analysis is defined as a particular weighted average of the image pixels intensities or a function of such moments, usually chosen to have some attractive property or interpretation. These moments of an image are useful for defining some simple properties of an image such as its area, centroid and information about its orientation as well. Upon performing the image analysis and later deriving mathematical equations for the images, seven moments of an image which are invariant to rotation, scaling and translation can be obtained. The seven moment invariant equations given by Hu [139] are used to obtain the seven values of the original images. These values are used as features for shape recognition.

The 2-D moments of order (p, q) of some function $f(x, y)$ are defined by

$$m_{pq} = \iint x^p y^q f(x,y)dxdy \tag{6.5}$$

The first moment μ_{oo} is denoted by m. Setting $\bar{x} = \frac{\mu_{10}}{m}, \bar{y} = \frac{\mu_{01}}{m}$ the central moments of order (p, q) are defined as

$$\mu_{pq} = \sum_x \sum_y (x-\bar{x})^p (y-y)^q f(x,y) \tag{6.6}$$

The normalized central moments is denoted by $\eta_{pq} = \frac{u_{pq}}{(\mu_{00})^{\gamma}}$,

where

$$\gamma = \frac{1}{2}(p+q)+1 \quad for \quad p+q = 2,3,... \tag{6.7}$$

From the second and third order moments, a set of seven invariants moments can be derived. They are given by:

$$\begin{aligned}
m_1 &= (\eta_{20} + \eta_{02}) \\
m_2 &= (\eta_{20} - \eta_{02})^2 + 4\eta^2_{11} \\
m_3 &= (\eta_{30} - \eta_{02})^2 + (3\eta_{21} - \eta_{03})^2 \\
m_4 &= (\eta_{30} + \eta_{12})^2 + (3\eta_{21} + \eta_{03})^2 \\
m_5 &= (\eta_{30} - 3\eta_{12})(\eta_{30} + \eta_{12})\,[(\eta_{30} + \eta_{12})^2 - 3(\eta_{21} + \eta_{03})^2] \\
&+ (3\eta_{21} - \eta_{03})(\eta_{21} + \eta_{03})\,[3(\eta_{30} + \eta_{12})^2 - (\eta_{21} + \eta_{03})^2) \\
m_6 &= (\eta_{20} - \eta_{02})\,[(\eta_{30} + \eta_{12})^2 - (\eta_{21} + \eta_{03})^2] + 4\eta_{11}(\eta_{30} + \eta_{12})(\eta_{21} + \eta_{03}) \\
m_7 &= (3\eta_{21} - \eta_{03})(\eta_{30} + \eta_{12})\,[(\eta_{30} + \eta_{12})^2 - 3(\eta_{21} - \eta_{30})^2] \\
&+ [(3\eta_{12} - 3\eta_{30})(\eta_{21} + \eta_{03})[3(\eta_{30} + \eta_{12})^2 - (\eta_{21} + \eta_{03})^2]
\end{aligned} \tag{6.8}$$

Thus the shape feature vector using moment invariants is $f_m = (m_1, m_2, m_3, \ldots m_7)$. It may be noted that the invariant moments as shape measure have desirable properties [139].

(c) *Pattern generation based feature detection*

The three common shapes viz rectangular, square and circle binary images are generated using Boolean values as shown in Figure 6.3 (a), (c) and (e) respectively. Pattern for each target shape is generated and used as feature. Similar method has been used for GPR but in TWI case it is not yet explored [196]. Each target has different pattern according to its shape. To extract pattern every element in the rows and then columns of the target image are added. After this a waveform is obtained as summed value of elements vs. columns and rows. This waveform will provide identity of the shape of target. Waveforms of standard shapes such as rectangle, square and

circle are shown in Figure 6.3 (b), (d) and (f) respectively. It can be seen that each of these shapes can be distinguished uniquely using their waveforms.

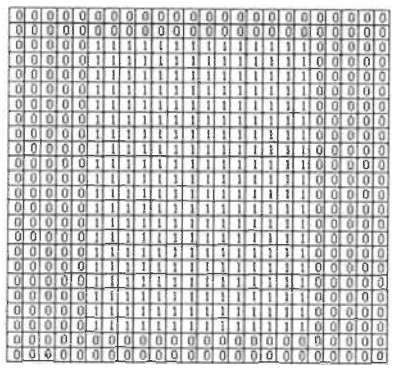

(a)

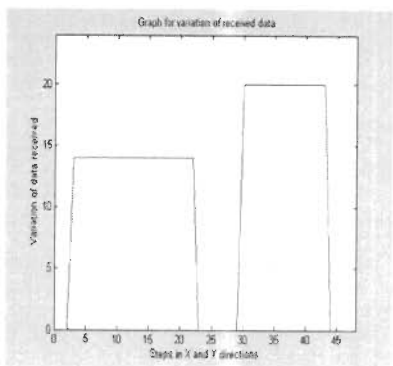

(b)

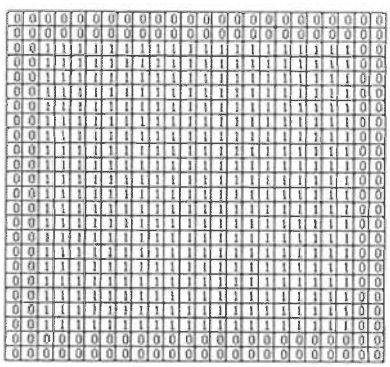

(c)

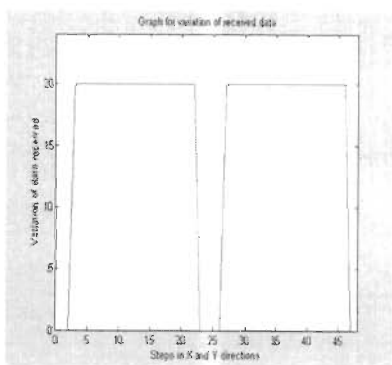

(d)

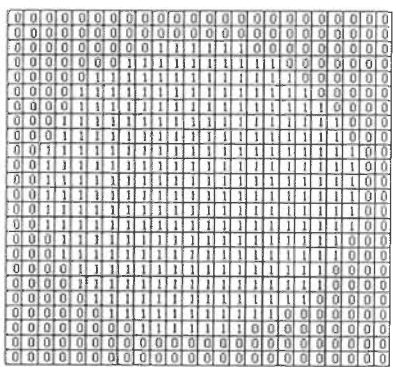

(e)

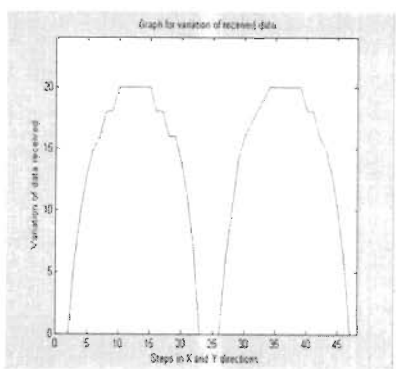

(f)

Figure 6.3 Synthetic data for different shapes with their patterns respectively (a)Data matrix for Rectangle (b) Pattern for rectangle (c) Data matrix for square (d) Pattern for square (e) Data matrix for circle (f) Pattern for circle [196]

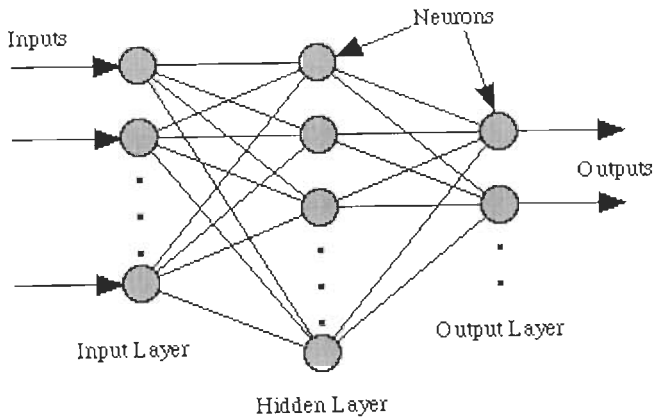

Figure 6.4 General neural network structure

6.2.3 Neural network classifier

After training feature vectors are obtained, classifier is design to identify the target shape. Although many classical pattern recognition algorithms are available for this purpose, neural networks are very promising due to their advantages over conventional pattern classification. It can approximate any target function and can handle even redundant features.

The main reason for the feasibility of neural networks is their ability to generalize after learning from training data. That is, they can identify a test pattern even when that particular pattern is not used for training. Figure 6.4 shows a fully connected three layer perceptron network with one hidden layer having number of neurons. The number of neurons in the input layer is equal to the feature vector dimension l and the number of neurons in the output layer is equal to the number of target classes. The neurons in the network give a nonlinear transform between their inputs and outputs by the use of sigmoidal activation functions. The network in Figure 6.4 is trained until its mean squared error (MSE) between the desired outputs and its actual outputs is less than a certain threshold level. The training strategy is based on the well-known back-propagation learning rule, which is an iterative algorithm updating each neuron's weight by searching the local gradient of the error surface. After a sufficient number of training iterations using training patterns, a classifier having the ability to discriminate all target types can be formed, and it can identify a test feature vector at any aspect of any target among all targets. In order to train the network to achieve the best classification accuracy, a large number of training iterations (i.e. a low MSE) are

required in general. However, a simply low MSE value does not guarantee the best performance of the network. When the network is trained using too many training patterns, it may memorize the training data and therefore be less able to generalize test data, yielding degradation in classification performance. To prevent them from overtraining, the maximum number of iterations is usually defined to stop the training of the network. Therefore, the network should be stopped when the MSE is less than a certain threshold level, or the maximum number of iterations is reached.

6.3 Results and discussion

The experimental data is first used to obtained C-scan image, then feature are extracted and lastly shape recognition technique is applied.

6.3.1 Data used

Metal target with regular shapes behind plywood wall is taken for analysis. The data collection details are given in Section 1.3.2 and Table 1.2 (S.No. 1,2 and 3). To obtain image of target kept behind wall, a full C-scan data was measured manually with the help of scanning system in which both horizontal and vertical scanning spacing was kept as 5 cm. In this experiment, twenty B-scans were measured each containing twenty six A-scans covering an area of 1.3×1 m^2. In the test area that is behind wall, targets having different shapes (circle, square and rectangular) were kept and data was collected. C-scan data is acquired for three different regular shapes that is circular, square and rectangle.. Apart from experimental data synthetic images with binary values for different dimensions were generated for three regular shapes i.e. circle, square and rectangle.

6.3.2 C-scan imaging

C-scan image can be considered as a 2D image in which local contrast in pixel intensity provides information about existence and size of target at a particular location of target. The results of the imaging algorithms described in Section 5.2 for plywood type of wall are observed. From raw C-scan, it is not possible to get the exact shape and dimension of target as shown in Figure 6.5. Results are obtained of

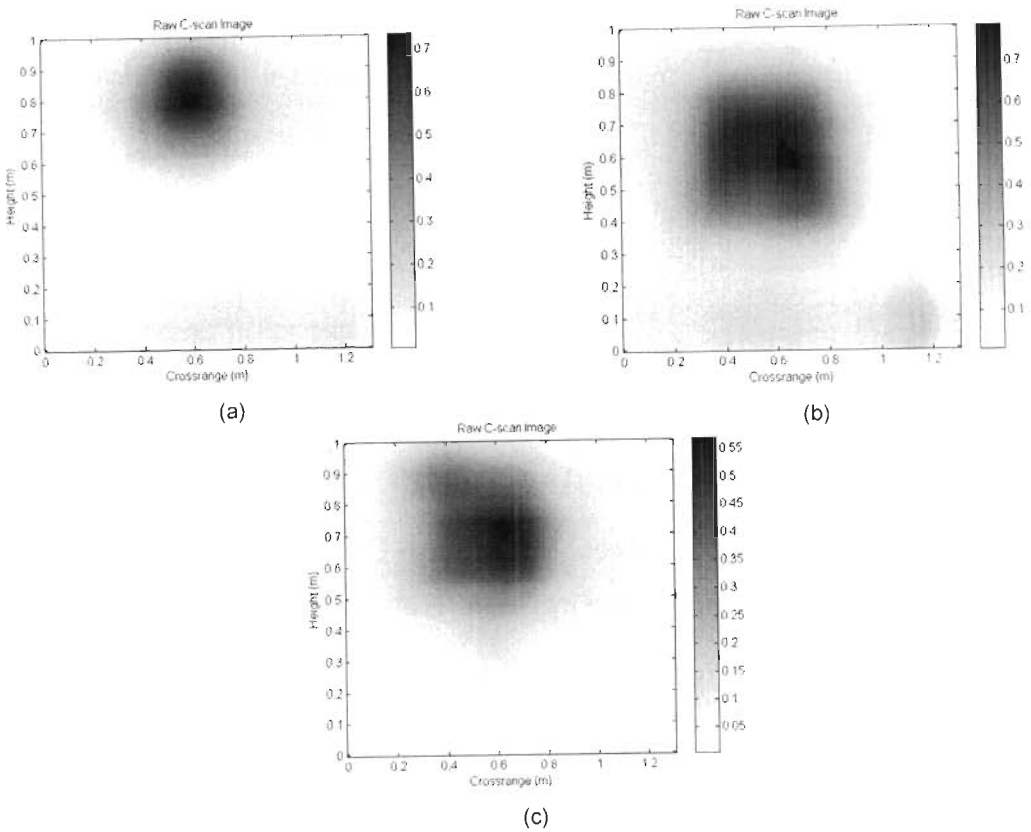

Figure 6.5 Raw C-scan image (a) Circle (b) Square (c) Rectangle

front view of a C-scan image for target having regular shapes such as circular, square and rectangular kept behind plywood wall. The local contrast in the pixel intensity provides a clue for potential existence of target with approximate shape. Observing raw image indicates for the requirement of enhancement using image processing techniques. The reasons for degradation may be due to various factors such as low resolution due to limited performance of TWI system, low contrast due to limited dynamic range of TWI system.

For enhancement thresholding and edge detection techniques are applied so that target detection can be enhanced. For filtering, window size 3 is taken as smaller window size preserved the edges of targets. After filtering, thresholding is applied to detect the shape of target. The thresholded images are shown in Figure 6.6(a), (c) and (e) for circular, square targets and rectangular which gives the basic idea of shape of target. An edge detection technique is also applied to enhance the shape of regular targets.

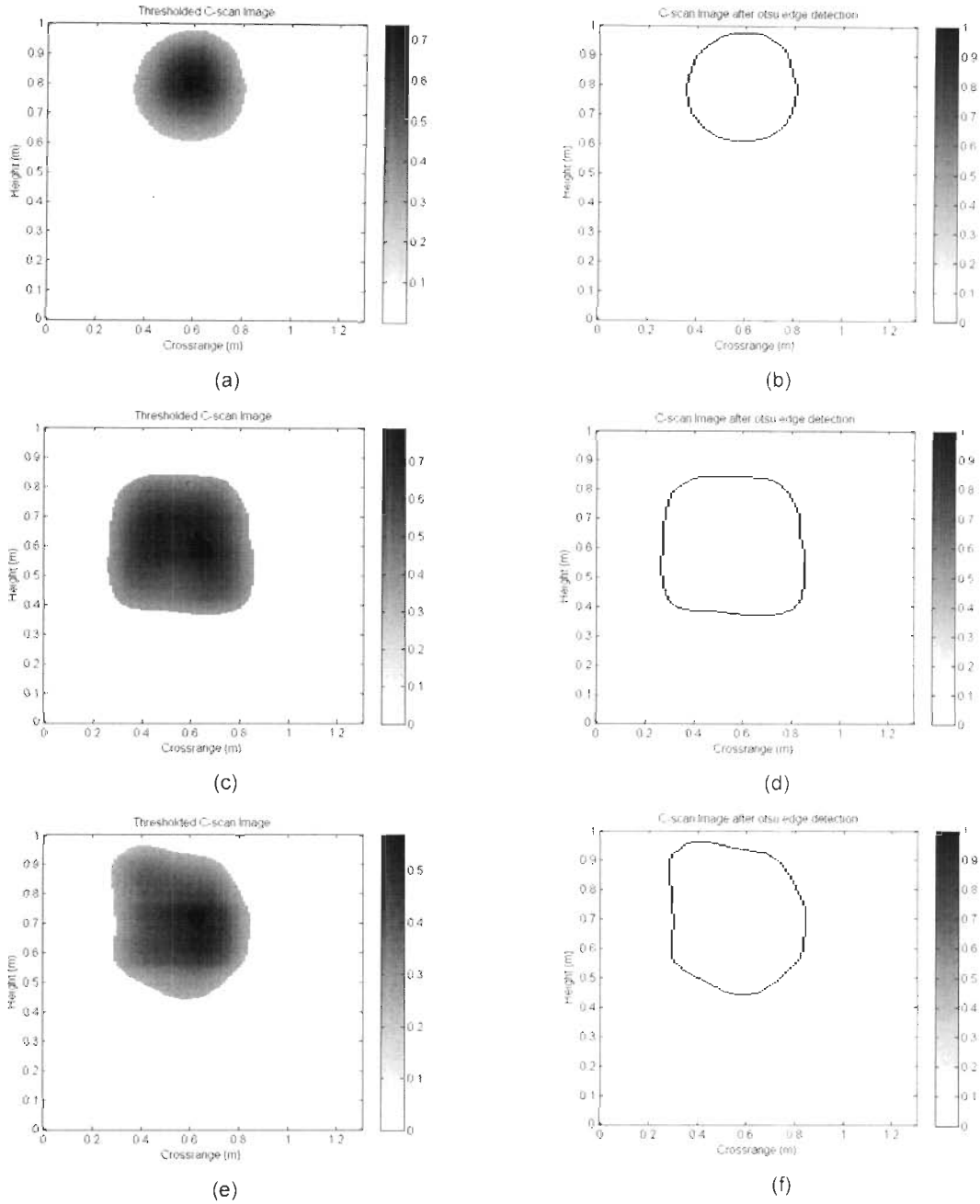

Figure 6.6 C-scan image in case of plywood wall (a) Circular metal plate target after applying thresholding (b) Circular metal plate target after applying edge detection (c) Square metal plate target after applying thresholding (d) Square metal plate after applying edge detection (e) Rectangular metal plate target after applying thresholding (f) Rectangular metal plate after applying edge detection

Figure 6.6 shows the edge extraction after applying Sobel operator where the shape of target is almost observed. The results have been obtained in case of circular target, square target and rectangular target when place behind plywood wall as shown in Figure 6.6 (b), (d) and (f) respectively. Though the target image does not correspond to the actual shape of the target but much vital information about the target can be inferred namely its approximate shape, height and extent along cross range. Instead of applying edge detection, neural network can be used to recognize the shape of target. The applicability of this approach is not restricted to regular target shapes. The features can be obtained for any target shape and neural network can be trained accordingly.

6.3.3 Recognition of shape of targets

(a) *Feature extraction*

For target shape recognition, first step is to obtain features for training data. Features of three standard images (Circle, square and rectangle) are obtained. Instead of selecting only one feature type, all the feature extraction techniques described above are used to obtain single feature vector of particular target shape. It improves robustness of algorithm. After getting all the features of the image, they are arranged in a column vector form for each shape. Dimension must be same for each target shape.

Features are extracted using Fourier descriptor, moment invariants and pattern generation techniques. To generate sufficient target features synthetic images are used to obtained features. After getting all the features of the image, they are arranged in a column vector form for each shape. It is for certain that no two images will always have the same number of Fourier descriptor, thus to take care of this problem the minimum number of Fourier descriptor obtained from image shape is kept same for remaining shapes. For example, in a 191-by-251 size image if 82 Fourier descriptors are obtained for the circle, 90 are obtained for the square and 86 are obtained for the rectangle then only first 82 Fourier descriptors are considered from all target shapes. The number of features obtained from moment invariant are 7 for each target shape. The number of features from the third technique i.e pattern generator will depend on dimension of image. If the dimension of image is 191×251 then number of feature from pattern generator will be 442. Total number of features obtained for a particular

shape of target will be 82+442+7=531. These number of features are obtained for each shape.

(b) *Neural network for training and testing*

A simple two layer feed-forward neural network is trained using standard back propagation algorithm. The network receives 531 feature values as input vector for single target. Each target provides different features according to its shapes.The input layer does not require computing neuron. The neurons in hidden layer detects the features with associated weights of neuron in input patterns. The number of neurons in hidden layer is determined to be 10. Neurons in hidden layer and output layer uses logsig transfer function. The output layer contains three neurons to indicate three target shapes. The output values at each node are coded as (1,0,0), (0,1,0) and (0,0,1) respectively for circular, square and rectangular shapes. These features are then used by output layer in determining output shape. The network is trained for maximum 5000 epochs or until network errors fall below 0.01. The network is trained on seven sets of experimental and synthetic images for each target shape. As soon as the neural network training is successfully completed the neural network is tested on ten sets of images including training sets.

(c) *Validation*

For validation, the real image that of a rectangular metal sheet of dimension 25 cm by 30 cm as shown in Figure 6.7 is used to test the network. It is observed that the neural network recognized the target correctly in most of the cases.

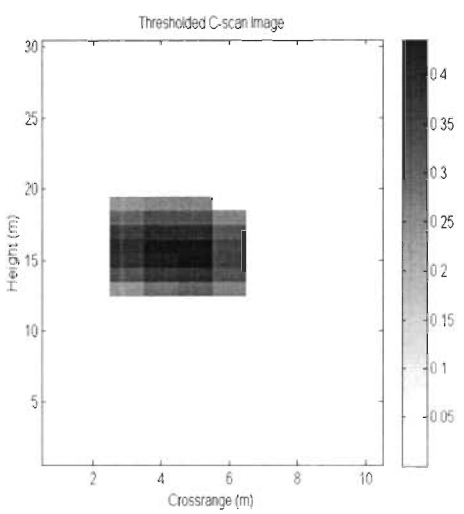

Figure 6.7 C-scan image of rectangular metal plate after applying thresholding

Table 6.1 Recognition Results

Actual shape of Target	Error
Circle	0/10
Square	1/10
Rectangular	2/10

In case if the shape is different then an error is recorded. The results have been tabulated in Table 6.1. The results for each shape have been obtained separately. The numerator shows the number of time an error occurred and denominator shows the number of experiments/ different images. Since number of real images (obtained from experiment are few, synthetic images obtained for different shapes are used. It is observed that for real images, the recognition error is more compared to synthetic images. Image information system where output will be the shape information of a target can be designed.

6.4 Concluding remarks

Results on experimental data show that the proposed imaging algorithm along with recognition exhibits promising performances in terms of detection and recognition. The proposed imaging algorithm will be very meaningful when first hand information about the target approximate shape is required quickly. These results which are obtained do not exactly resemble shape of target. So shape information can be confirmed after using recognition technique.

After using three feature extraction techniques, correct recognition of target shape is obtained. The major limitation of all these techniques is that their performance gets drastically affected by the presence of noise. After using this features, neural network can categorized different targets based on shape in most of the cases. This technique can be extended to discriminate between standing and sitting human or between animal and human in through wall imaging applications. In future the orientation effects as well as targets other than metal can be checked for shape recognition.

Chapter 7

Concluding remarks and Future Work

This section aims to provide a summary of structure, central ideas, results and key contributions of this thesis.

The first focus of the research is to explore the possibility of application of various existing clutter removal techniques for TWI data and to check the possibility of detection of low dielectric targets. After applying clutter reduction techniques like SVD, PCA, FA and ICA clutters are successfully minimized. This implies that the techniques are powerful. Signal strength of target kept behind wall is improved by applying clutter removal techniques. It is found that ICA based technique gives better result in comparison to other clutter removal techniques like SVD, PCA and FA.

SVD, PCA and FA are not able to detect the target having low dielectric constant, like Teflon behind the wall. On the other hand ICA based clutter removal technique has a better potential to detect low dielectric constant target like Teflon behind the wall. Thus ICA based technique may be applied to enhance the target signal detection. Processing using clutter reduction increases target signal strength which increases the probability of correct target detection and hence it is useful for further process of classification and recognition.

The problem of detection and classification of low dielectric and high dielectric constant stationary target are considered and a possible solution is proposed. The concentration is mainly on detecting low dielectric constant material. Modified statistical based threshold method is proposed and it is found that it performs quite well from point of view of detection of pixels representing low dielectric as well as with less false alarm rate. After detection, pdf based model is proposed for target classification (i.e., metallic and non metallic targets). Weibull distribution is quite suitable to classify the targets as metallic and Teflon targets.

The suitable imaging techniques for TWI system is another important problem. Therefore, techniques like ω-k, back projection and delay sum are applied. Different techniques have been compared using different image contrast measure metric like entropy and ratio of standard deviation to mean. Obtained images are evaluated with respect to both the metrics, which are a measure of image contrast. Results are best for *delay sum*, closely followed by *ω-k* algorithm and back projection for all the cases. From computational point of view *ω-k* algorithm technique outperforms other techniques.

The last chapter presents development of target recognition technique based on shape. The shape based features are extracted preserving as much information for classifying targets as possible. The resulting features are passed to classifier stage based on multilayer perceptron neural network. Result shows that the proposed technique has significant potential for target recognition even for slightly noisy images.

7.2 Future work

Present thesis work has scope and possibilities which can be extended further. A few can be listed as following.

Real time analysis for detection and classification is one of the major interests of users. The developed techniques may be explored to be applied for real time analysis. The orientation of targets should be considered in future for identifying different targets.

The effects of wall such as wave refraction, attenuation and multiple reflections on imaging can be studied further. In this study, brick wall is used which is assumed to

be homogeneous. Instead, different complex type of walls like concrete with metal inside can be considered and its effect on imaging can be studied. The accuracy of classification of target can be increased by fusing more discriminant features. An extensive study of different features based on geometrics, parametric models, texture etc., should be investigated. In future emphasis should be given to generate 3D images with less complex operation.

Bibliography

[1] Abujarad, F. and Omar, A., 2006, Comparison of independent component analysis (ICA) algorithms for GPR detection of non-metallic land mines. In *Proceedings of SPIE*, 6365, pp. 636516-1–636516-12.

[2] Abujarad, F., Jostingmeier, A. and Omar, A., 2004, Clutter removal for landmine using different signal processing techniques. In *Proceedings of the Tenth IEEE International Conference on Ground Penetrating Radar, GPR*, 21–24 Jun. 2004, Delft, The Netherlands, pp. 697–700.

[3] Aguasca, A., Broquetas, A., Mallorqui, J.J. and Fabregas, X., 2004, A solid state L to X-band flexible ground-based SAR system for continuous monitoring applications. In *IEEE International Geoscience and Remote Sensing Symposium, IGARSS '04,* 20-24 Sept. 2004, Anchorage Alaska, pp. 757–760.

[4] Ahmad, F. and Amin, M. G., 2006, Noncoherent approach to through the wall radar localization. *IEEE Transactions on Aerospace and Electronic Systems*, 42, pp. 1405–1419.

[5] Ahmad, F. and Amin, M. G., 2008, Multi-location wideband synthetic aperture imaging for urban sensing applications. *Special Issue on Advances in indoor Radar imaging, Journal of the Franklin Institute*, 345, pp. 618–639.

[6] Ahmad, F., Amin, M. G. and Kassam, S. A., 2005, Synthetic aperture beamformer for imaging through a dielectric wall. *IEEE Transactions on Aerospace and Electronic Systems*, 41, pp. 271–283.

[7] Ahmad, F., Amin, M. G. and Mandapati, G., 2007, Auto focusing of through the wall radar imagery under unknown wall characteristics. *IEEE Transaction Image Processing*, 16, pp. 1785–1795.

[8] Ahmad, F., Zhang, Y. and Amin, M. G., 2008, Three-dimensional wideband beamforming for imaging through a single wall. *IEEE Geoscience Remote Sensing Letters*, 5, pp. 176–179.

[9] Akduman, I., Crocco, L. and Soldovieri, F., 2010, Experimental validation of a simple system for through-the-wall inverse scattering. *IEEE Geoscience and Remote Sensing Letters*, 99, pp. 258–262.

[10] Al-Nuaimy, W., Huang, Y., Nakhkash, M., Fang, M.T.C., Nguyen, V.T. and Eriksen, A., 2000, Automatic detection of buried utilities and solid objects with GPR using neural networks and pattern recognition. *Journal of Applied Geophysics*, 43, pp. 157–165.

[11] Antonio, T., Jacopo, G. and Yahia, H., 2005, Multiscale techniques for the detection of precipitation using thermal IR satellite images. *IEEE Geoscience and Remote Sensing Letters*, 2, pp. 447–450.

[12] Axelsson, S.R.J., 2007, Analysis of random step frequency radar and comparison with experiments. *IEEE Transactions on Geoscience and Remote Sensing*, 45, pp. 890–904.

[13] Backer, B., Borjeson, H., Zutter, D. and Olyslager, F., 2003, Propagation mechanisms for UHF wave transmission through walls and windows. *IEEE Transactions on Vehicular Technology*, 52, pp. 1297–1307.

[14] Baranoski, E.J., 2008, Through-wall imaging: historical perspective and future directions. *Special Issue on Advances in Indoor Radar Imaging, Journal of the Franklin Institute*, 345, pp. 556–569.

[15] Barrie, G., 2003, Ultra-wideband synthetic aperture: data and image processing. Technical Memorandum, TM 2003–015 Defense R&D Canada DRDC Ottawa.

[16] Bell, D.C. and Narayanan, R.M., 2001, Theoretical aspects of radar imaging using stochastic waveforms. *IEEE Transactions on Signal Processing*, 49, pp. 394–400.

[17] Billingsley, J.B., Farina, A., Gini F., Greco, M.V. and Verrazzani, L., 1999, Statistical analyses of measured radar ground clutter data. *IEEE Transactions on Aerospace and Electronics Systems*, 35, pp. 579–593.

[18] Biradar, G.S., Merchant, S.N. and Desai, U.B., 2009, Frequency and Time Hopping PPM UWB Multiple Access Communication Scheme. *International Journal of Communication*, 4, pp. 14-19.

[19] Biswas, S. and Lohani, B., 2008, Development of high resolution 3D sound propagation model using LiDAR data and air photo. In *The International Archives of the Photogrammetry, Remote Sensing and Spatial Information Sciences*, XXXVII. Part B7, Beijing, 2008, pp. 1735-1740.

[20] Brunzell, H., 1999, Detection of shallowly buried objects using impulse radar. *IEEE Transactions on Geoscience and Remote Sensing*, 37, pp. 875–886.

[21] Burkholder, R.J. and Browne, K.E., 2010, Coherence factor enhancement of through–wall radar images. *IEEE Antennas and Wireless Propagation Letters,* 9, pp. 842–845.

[22] Cardoso, J.F., 1998, Blind source separation: statistical principles. In *Proceedings of the IEEE*, 86, pp. 2009-2024

[23] Carevic, D., 2000, Clutter reduction and detection of mine like objects in ground penetrating radar data using wavelets. *Subsurface Sensing Technologies and Applications,* 1, pp. 101 –117.

[24] Carin, L., Sichina, J. and Harvey, J.F., 2002, Microwave underground propagation and detection. *IEEE Transactions on Microwave Theory and Techniques*, 50, pp. 945–952.

[25] Carta, J.A. and Ramirez, P., 2007, Analysis of two-component mixture Weibull statistics for estimation of wind speed distributions. *Renewable Energy*, 32, pp. 518–531.

[26] Casanova, J.J., Judge, J. and Jang, M., 2007, Modeling transmission of microwaves through dynamic vegetation. *IEEE Transactions on Geoscience and Remote Sensing*, 45, pp.3145–3149.

[27] Catapano, I. and Crocco, L., 2009, An imaging method for concealed targets. *IEEE Transactions on Geoscience and Remote Sensing*, 47, pp. 1301–1309.

[28] Chandra, R., Gaikwad, A. N., Singh, D. and Nigam, M. J., 2008, An approach to remove the clutter and detect the target for ultra-wideband through-wall imaging. *Journal of Geophysics and Engineering*, 5, pp. 412–419.

[29] Chen, C.H. and Wang Z., 2006, ICA and factor analysis application in seismic profiling. In *IEEE International Geoscience and Remote Sensing Symposium*, 31 Jul.–4 Aug., 2006, Denver Colorado, USA, pp. 1560–1563.

[30] Chen, Y., Gu, Y., Gu, J. and Yang, J., 2005, Particle filter based road detection in SAR image. In *IEEE International Symposium on Microwave, Antenna, Propagation and EMC Technologies for Wireless Communications Proceedings*, 8–12 Aug., Beijing, China, pp. 301–305.

[31] Christopher, S., Singh, A.K. and Kaul, A., 1995, Design and development of dual polarised corrugated feed for VSAT applications. *IETE Technical Review*, 12, pp.331–35.

[32] Christopher, S. and Singh, A.K, 1996, Design and development of VSAT antenna. *Defence Science Journal*, 46, pp. 277–282.

[33] Chrysoulakis, N., Herlin, I., Prastacos, P., Yahia, H., Grazzini J. and Cartalis, C., 2007, An improved algorithm for the detection of plumes caused by natural or technological hazards using AVHRR imagery. *Remote Sensing of Environment*, 108, pp. 393–406.

[34] Comon, P., 1994, Independent component analysis, a new concept. *Signal Processing*, 36, pp. 287–314.

[35] Curie, N. C., 1989, *Radar Reflectivity measurement: Technique and Applications,* (Artech House, Norwood MA).

[36] Daniel, D. J., 2006, A review of GPR landmine. *International Journal of Sensing and Imaging,* 7, pp. 90–123.

[37] Das, A.K., Singh, C.P. and Mohan, S., 2006, Polarization signatures of land cover classes using L-band polarimetric SAR data. In *Proceedings of SPIE*, 6410, pp. 641003.1–641003.12.

[38] Dasari, A., Mohan, S. and Patel, B., 2006, Multifrequency SAR signatures of forest class covering parts of Rajpipla, Gujarat. In *Proceedings of SPIE*, 6410, pp. 641005.1–641005.11.

[39] Debes, C., Amin, M.G. and Zoubir, A.M., 2008, Target detection in single and multiple-view through-the-wall radar imaging. *IEEE Transactions on Geoscience and Remote Sensing*, 47, pp. 1349–1361.

[40] Debes, C., Hahn, J., Zoubir, A.M. and Amin, M.G., 2010, Feature extraction in Through-the-Wall radar imaging. In *IEEE International Conference on*

Acoustics Speech and Signal Processing (ICASSP), 14-19 March 2010, Texas, USA, pp.3562-3565.

[41] Debes, C., Riedler, J., Zoubir, A. M. and Amin, M.G., 2010, Adaptive target detection with application to through-the-wall radar imaging. *IEEE Transactions Signal Processing,* 58, pp.5572–5583.

[42] Dehmollaian, M. and Sarabandi, K., 2008, Refocusing through building walls using synthetic aperture radar. *IEEE Transactions on Geoscience and Remote Sensing*, 46, pp. 1589–1599.

[43] Dehmollaian, M., Thiel, M. and Sarabandi, K., 2009, Through the wall imaging using differential SAR. *IEEE Transactions on Geoscience and Remote Sensing*, 47, pp. 1289–1296.

[44] Didascalou, D., Dottling, M., Geng, N. and Wiesbeck, W., 2003, An approach to include stochastic rough surface scattering into deterministic ray-optical wave propagation modeling. *IEEE Transactions on Geoscience and Remote Sensing*, 51, pp. 1508–1515.

[45] Digby–Argus, S.A., Hawkins, R.K. and Singh, K.P., 1987, Microwave remote sensing of ice in Lake Melville and the Labrador Sea. *IEEE Journal of Oceanic Engineering*, OE 12, pp. 503–517.

[46] Dogaru, T. and Carin, L., 1998, Time domain sensing of targets buried under a rough air-ground interface. *IEEE Transactions on Antennas and Propagation*, 46, pp. 360–372.

[47] Duque, S., Lopez-Dekker, P. and Mallorqui, J.J., 2010, Single-pass bistatic SAR interferometry using fixed-receiver configurations: theory and experimental validation. *IEEE Transactions on Geoscience and Remote Sensing*, 48, pp. 2740–2749.

[48] Engin, E., Ciftcioglu, B., Ozcan, M. and Tekin, B., 2007, High resolution ultra wideband wall penetrating radar. *Microwave and Optical Technology Letters*, 49, pp. 320–325.

[49] Estephan, H., Amin, M.G. and Yemelyanov, K.M., 2010, Optimal waveform design for improved indoor target detection in sensing through-the-wall applications. *IEEE Transactions on Geoscience and Remote Sensing*, 48, pp.2930–2941.

[50] Falconer, D.G., Ficklin, R.W. and Konolige, K.G, 2000, Robot-mounted through-wall radar for detecting, locating, and identifying building occupants. In *IEEE International Conference on Robotics and Automation, Proceedings. ICRA,* 2, 24- 28 April San Fransico, California, pp.1868–1875.

[51] Farwell, M., Ross, J., Luttrell, R., Cohen, D., Chin, W. and Dogaru, T., 2008, Sense through the wall system development and design considerations. *Journal of the Franklin Institute*, 345, pp. 570–591.

[52] Fernandez, D., Juan C., Judge, J., Slatton, K., Shrestha, R., Carter, W. and Bloomquist, D., 2010, Characterization of full surface roughness in agricultural soils using groundbased LiDAR. In *IEEE International Geoscience and Remote Sensing Symposium (IGARSS),* 25–30 July 2010, Honolulu, USA, pp. 4442–4445.

[53] Ferris, D.D. Jr. and Currie, N. C., 1998, Microwave and millimeter wave systems for wall penetration. In *Proceedings of SPIE*, 3375, pp. 269–279.

[54] Ferris, D.D.Jr. and Currie, N.C., 1998, A survey of current technologies for through-the-wall surveillance (TWS). In *Proceedings of SPIE*, 3577, pp. 62–72.

[55] Fontana, R. J., 2004, Recent system applications of short pulse ultra wideband (UWB) technology. *IEEE Transactions on Microwave Theory and Techniques*, 52, pp. 2087–2104.

[56] Frazer, L. M., 1996, Surveillance through walls and other opaque materials. In *Proceedings of the IEEE National Radar Conference,* 13–16 May 1996, Michigen USA, pp. 27–31.

[57] Freeman, A., Johnson, W.T.K., Huneycutt, B., Jordan, R., Hensley, S., Siqueria, P. and Curlander, J., 2000, The 'Myth' of the minimum SAR antenna area constraint. *IEEE Transactions on Geoscience and Remote Sensing*, 38, pp. 320–324.

[58] Freundorfer, A. P. and Lizuka, K., 1993, A study on scattering of radio waves from buried spherical targets using the step frequency radar. *IEEE Transactions on Geoscience and Remote Sensing*, 31, 6, pp. 1253–1255.

[59] Frigui, H. and Gader,P, 2009, Detection and discrimination of land mines in ground penetrating radar based on edge histogram descriptors and a

possibilistic K nearest neighbour classifier. *IEEE Transactions Fuzzy system*, 17, pp. 185–199.

[60] Gaikwad, A. N., Singh, D. and Nigam, M. J., 2010, Application of clutter reduction techniques for detection of metallic and low dielectric target behind the brick wall by SFCW radar in UWB range. *IET Radar Sonar and Navigation*, 5, pp. 416–425.

[61] Garmatyuk, D.S. and Narayanan, R.M., 2002, Ultra-wideband continuous-wave random noise Arc-SAR. *IEEE Transactions on Geoscience and Remote Sensing*, 40, pp. 2543–2551.

[62] Gaugue, A.C. and Politano, J.L., 2005, Overview of current technologies for through-the-wall-surveillance. In *Proceedings of SPIE*, 5989, pp. 59891H-1–59891H-11.

[63] Gautam, R.S., Singh, D. and Mittal, A., 2008, An efficient contextual algorithm to detect subsurface fires with NOAA/AVHRR data. *IEEE Transactions on Geoscience and Remote Sensing*, 46, pp. 2005–2015.

[64] Gauthier, S.A. and Chamma, W., 2004, Surveillance through concrete walls. In *Proceedings of SPIE*, 5403, pp. 597–608.

[65] Gazdag, J. and Sguazzero, P., 1984, Migration of seismic data, In *Proceedings of IEEE*, 72, pp. 1302–1315.

[66] Gentili, G.G. and Spagnolini, U., 2000, Electromagnetic inversion in monostatic ground penetrating radar: TEM horn calibration and application. *IEEE Transactions on Geoscience and Remote Sensing*, 38, pp. 1935–1936.

[67] Ghosh, S. and Chakrabarty, A., 2007, Prediction of Antenna Factor of wire antenna in the GHz Transverse Electromagnetic Cell. *IETE Journal of Research*, 53, pp. 25-33.

[68] Ghosh, S. and Chakrabarty, A., 2008, Ultra Wideband Performance of Dielectric Loaded T-shaped Monopole Transmit and Receive Antenna / EMI Sensor. *IEEE Antennas and Wireless Propagation Letters*, 7, pp. 358-361.

[69] Ghosh, S. and Lohani, B., 2007, 3D visualization of LiDAR data: state of the art and proposed system. *GIM International*, 21, pp. 15–17.

[70] Gohil, B. S., Mathur, A. K. and Pandey, P. C., 1994, An algorithm for sea surface temperature estimation from ERS-1 ATSR using moisture dependent

coefficients: a simulation study. *International Journal of Remote Sensing*, 15, pp. 1161–1167.

[71] Goldstein, G.B., 2009, False-alarm regulation in log-normal and Weibull clutter. *IEEE Transactions on Aerospace and Electronic Systems*, 9, pp. 84–92.

[72] Grazzini, J., Turiel, A. and Yahia, H., 2002, Entropy estimation and multiscale processing in meteorological satellite images. In *Proceedings, 16th International Conference on Pattern Recognition*, 3, pp. 764–768.

[73] Grazzini, J., Turiel, A. and Yahia, H., 2005, Presegmentation of high-resolution satellite images with a multifractal reconstruction scheme based on an entropy criterium. In *Proceeding IEEE International Conference on Image Processing (ICIP'05)*, 11–14 Sept. 2005, Genova, Italy, pp. 11–14.

[74] Grazzini, J., Turiel, A., Yahia, H. and Isabelle, Herlin, 2003, Analysis and comparison of functional dependencies of multiscale textural features on monospectral infrared images. *In Proceedings IEEE International Geoscience and Remote Sensing Symposium, IGARSS '03*, 21–25 July, Toulouse France, pp. 2045–2047.

[75] Greco, M., Gini, F. and Rangaswamy, M., 2006, Statistical analysis of measured polarimetric clutter data at different range resolutions. In *IEE Proceedings Radar, Sonar & Navigation*, 153, pp. 473–481.

[76] Greneker, E. F., 1997, Radar sensing of heartbeat and respiration at a distance with security applications. In *Proceedings of SPIE, Radar Sensor Technology II*, 3066, Orlando, Florida, pp. 22–27.

[77] Gu, J., Yang, J., Zhang, H., Peng, Y., Wang, C. and Zhang, H., 2004, Speckle filtering in polarimetric SAR data based on the subspace decomposition. *IEEE Transactions on Geoscience and Remote Sensing*, 42, pp. 1635–1641.

[78] Guha, D. and Siddiqui, J.Y., 2002, New CAD model to calculate the resonant frequency of inverted microstrip circular patch antennas. *Microwave and Optical Technology Letters*, 35, pp. 434–437.

[79] Guha, D. and Siddiqui, J.Y., 2003, Resonant frequency of circular microstrip antenna covered with dielectric superstrate. *IEEE Transactions on Antennas and Propagation*, 51, pp. 1649–1652.

[80] Guha, D. and Siddiqui, J.Y., 2004, Effect of a cavity enclosure on the resonant frequency of inverted microstrip circular patch antenna. *IEEE Transactions Antennas and Propagation*, 52, pp. 2177–2180.

[81] Guha, D. and Siddiqui, J.Y., 2004, Resonant frequency of equilateral triangular microstrip. *IEEE Transactions on Antennas and Propagation*, 52, pp. 2174–2177.

[82] Guha, D., 2001, Resonant frequency of circular microstrip antennas with and without air gaps. *IEEE Transactions on Antennas and Propagation*, 49, pp. 55–59.

[83] Gurbuz, A.C., McClellan, J.H. and Scott, W.R., 2009, A compressive sensing data acquisition and imaging method for stepped frequency GPRs. *IEEE Transactions on Signal Processing*.57, pp.2640–2650.

[84] Hantscher, S., Reisenzahn, A. and Diskus, C.G., 2008, Through-wall imaging with a 3-D UWB SAR algorithm. *IEEE Signal Processing Letters*, 15, pp. 269–272.

[85] Herique, A., 1997, Optimal windows for step frequency radar. *Signal Processing*, 62, pp. 335–349.

[86] Ho, A.T.S., Tham, W.H. and Low, K.S., 2005, Improving classification accuracy in through-wall radar imaging using hybrid prony's and singular value decomposition method. In *IEEE International Geoscience and Remote Sensing Symposium, 2005, IGARSS '05,* 25-29 Jul. 2005, Seoul, Korea, pp. 4267–4270.

[87] Horikoshi, J., Tanaka, K. and Morinaga, T., 1986, 1.2 GHz wave propagating measurements in concrete building for indoor radio communications. *IEEE Transactions on Vehicular Technology*, 35, pp. 146–152.

[88] Huang, Q., Wu, L., Wu, B. and Fang, G., 2010, UWB through-wall imaging based on compressive sensing. *IEEE Transactions on Geoscience and Remote Sensing*, 48, pp. 1408–1415.

[89] Hunt, A.R. and Hogg, R.D., 2002, A stepped-frequency, CW radar for concealed weapon detection and through the wall surveillance. In *Proceedings of SPIE*, 4708, pp. 99–105.

[90] Hunt, A.R., 2003, Image formation through walls using a distributed radar sensor array. In *IEEE Proceedings of 32nd Applied Imagery Pattern*

Recognition Workshop, 15–17 Oct. 2003, Washington, DC, USA, pp. 232–237.

[91] Hunt, A.R., 2009, Use of a frequency hopping radar for imaging and motion detection through walls. *IEEE Transactions on Geoscience and Remote Sensing*, 47, pp. 1402–1408.

[92] Hyvarinen, A., 1999, Fast and robust fixed-point algorithms for independent component analysis. *IEEE Transactions Neural Network*, 10, pp. 626–634.

[93] Jacopo, G., Antonio, T., Yahia, H. and Isabelle, H., 2007, A multifractal approach for extracting relevant textural areas in satellite meteorological images. *Environmental Modelling and Software*, 22, pp. 323–334.

[94] Jain, A.K., Duin, R.P.W. and Mao, J., 2000, Statistical pattern recognition: a review. *IEEE Transactions on Pattern Analysis and Machine Intelligence*, 22, pp. 4–37.

[95] Janson, M., Zwick, T. and Wiesbeck, W., 2009, Performance of time domain migration influenced by non-ideal UWB antennas. *IEEE Transactions on Antennas and Propagation*, 57, pp. 3549–3557.

[96] Ji, Z., Sarkar, T.K. and Li, B., 2001, Analysis of the effects of walls on indoor wave propagation using the FDTD method. *Microwave and Optical Technology Letters*, 29, pp. 19–21.

[97] Johnson, J.T., Demir, M.A. and Majurec, N., 2009, Through-wall sensing with multi-frequency microwave radiometry: a proof of concept demonstration. *IEEE Transactions on Geoscience and Remote Sensing*, 47, pp. 1281–1288.

[98] Judge, J., England, A.W., Crosson, W.L., Laymon, C.A., Hornbuckle, B.K., Boprie, D.L., Kim E.J. and Liou, Y., 1999, A growing season land surface process/ radiobrightness model for wheat-stubble in the southern great plains. *IEEE Transactions on Geoscience and Remote Sensing*, 37, pp. 2152–2158.

[99] Judge, J., Galantowicz, J.F. and England, A.W., 2001, Comparison of ground-based and satellite-borne microwave radiometric observations in the great plains. *IEEE Transactions on Geoscience and Remote Sensing*, 39, pp. 1686–1696.

[100] Judge, J., Galantowicz, J.F., England, A.W. and Dahl, P., 1997, Freeze/thaw classification for prairie soils using SSM/I radio brightnesses. *IEEE Transactions on Geoscience and Remote Sensing*, 35, pp. 827–832.

[101] Karlsen, B., Larsen, J., Sorensen, H.B.D. and Jakobsen, K.B., 2001, Comparison of PCA and ICA based clutter reduction in GPR systems for anti personal landmine detection. In *Proceedings 11th IEEE workshop on statistical signal processing*, 6–8 Aug. 2001, Singapore, pp. 146–149.

[102] Kempen, V.L. and Sahli, H., 2001, Signal processing techniques for clutter parameters estimation and clutter removal in GPR data for landmine detection. In *proceedings of the 11th IEEE Signal Processing Workshop on Statistical Signal Processing,* 6–8 Aug. 2001, Singapore, pp. 158–161.

[103] Khairnar, D.G., Merchant, S.N. and Desai, U.B., 2008, Radar Signal Detection In Non-Gaussian Noise Using RBF Neural Network. *International Journal on Computers*, 3, pp. 32 - 39.

[104] Khatri, H., Le, C. and Se, R.A., 2006, Identification of electromagnetic parameters of a wall and determination of radar signal level behind a wall. In *Proceedings of SPIE*, 6210, pp. 1–7.

[105] Kidera, S., Sakamoto, T. and Sato, T., 2009, High resolution 3-D imaging algorithm with an envelope of modified spheres for UWB through the wall radars. *IEEE Transactions on Antenna and Propagation*, 57, pp. 3520–3529.

[106] Kim, K., Choi, I. and Kim, H., 2000, Efficient radar target classification using adaptive joint time frequency processing. *IEEE Transactions Antennas propagation*,48, pp. 1789–1801.

[107] Kovalenko, V., Yarovoy, A.G. and Ligthart, L.P., 2007, A novel clutter suppression algorithm for landline detection with GPR. *IEEE Transactions on Geoscience and Remote Sensing*, 45, pp. 3740–3751.

[108] Kumar, P., Krishna, A.P., Nathawat, M.S., Singh, C.P., Kandya, A.K. and Mohan, S., 2006, Tree height estimation in Tundi reserved forest using SAR interferometry. In *Proceedings of SPIE*, 6410, pp. 641004.1–641004.7.

[109] Kumar, R., Sarkar, A. and Pandey, P. C., 1999, Estimation of ocean depths off Goa coast using ERS-1 Synthetic Aperture Radar. *Continental Shelf Research*, 19, pp.171–181.

[110] Kundu, A. and Chakrabarty, A., 2008, Frequency Domain NLMS Algorithm for Enhanced Jam Resistant GPS Receiver. *Progress in Electromagnetics Research (PIER)*, 3, pp. 69-78.

[111] Kurner, T., Cichon, D.J. and Wiesbeck, W., 1993, Concepts and results for 3D digital terrain-based wave propagation models: an overview. *IEEE Journal on Selected Areas in Communications*, 11, pp. 1002–1012.

[112] Lai, C.P., Ruan, Q. and Narayanan, R.M., 2007, Hilbert-Huang transform (HHT) analysis of human activities using through–wall noise radar. In *International Symposium on Signals, Systems and Electronics, 2007. ISSSE '07*, 30 Jul.– 2 Aug. 2007, Montreal Canada, pp. 115–118.

[113] Lavely, E.M., Zhang, Y., Hill III, E.H., Lai, Y., Weichman, P. and Chapman, A., 2008, Theoretical and experimental study of through-wall microwave tomography inverse problems. *Special Issue on Advances in Indoor Radar Imaging, Journal of the Franklin Institute*, 345, pp. 592–617.

[114] Le–Tien, T., Talhami, H. and Nguyen, D.T., 1997, Target signature extraction based on the continuous wavelet transform in Ultrawideband radar. *Electronics letters*, 33, pp. 89–91.

[115] Le, C., Dogaru, T., Nguyen, L. and Ressler, M.A., 2009, Ultrawideband radar imaging of building interior: measurements and predeictions. *IEEE Transactions on Geoscience and Remote Sensing*, 47, pp. 1409–1420.

[116] Lenz, R., Pontes, J. and Wiesbeck, W., 2005, A high accuracy calibration and receive instrument for TerraSAR-X ground calibration. In *Radar Conference*, 6–7 Oct. 2005, Paris, France, pp. 411–414.

[117] Lenz, R., Schuler, K., Younis, M. and Wiesbeck, W., 2006, TerraSAR-X active radar ground calibrator system. *IEEE Aerospace and Electronic Systems Magazine*, 21, pp. 30–33.

[118] Li, C.H. and Tam, P.K.S., 1998, An iterative algorithm for optimum cross entropy thresholding. *Pattern Recognition Letters*, 19, pp. 771–776.

[119] Li, L., Zhang, W. and Li, F., 2010, A novel auto focusing approach for real time through wall imaging under unknown wall characteristics. *IEEE Transactions on Geoscience and Remote Sensing,* 48, pp. 423–431.

[120] Li, Li., Zhang, W. and Li, F., 2010, Derivation and Discussion of the SAR Migration Algorithm Within Inverse Scattering Problem: Theoretical Analysis. *IEEE Transactions on Geoscience and Remote Sensing,* 48, pp. 415–422.

[121] Liseno, A., Tartaglione, F. and Soldovieri, F., 2004, Shape reconstruction of 2-D buried objects under a Kirchhoff approximation. *IEEE Transactions on Geoscience and Remote Sensing*, 1, pp. 118–121.

[122] Livingstone, C.E., Onstott, R.G., Arsenault, L.D., Gray, A.L. and Singh, K.P., 1987, Microwave sea ice signature near the onset of melt. *IEEE Transactions on Geoscience and Remote Sensing*, GE–25, pp. 174–187.

[123] Livingstone, C.E., Singh, K.P. and Gray, A.L., 1987, Seasonal and regional varations of active/passive microwave signatures of sea ice. *IEEE Transactions on Geoscience and Remote Sensing*, GE–25, pp. 159–173.

[124] Lizuka, K., Freundorfer, A.P., Wu, K.H., Mori, H., Ogura, H. and Nguyen, V., 1999, Step frequency radar. *Journal of Applied Physics*, 56, pp. 2572–2583.

[125] Lohani, B. and Singh, R., 2007, Development of a Hough transform based algorithm for extraction of buildings from actual and simulated LiDAR data. In *Mapworld Forum*, 22–25 January 2007, Hyderabad, India, pp. 1–12.

[126] Lohani, B. and Singh, R., 2008, Effect of data density, scan angle, and flying height on the accuracy of building extraction using LiDAR data. *Geocarto International*, 23, pp. 81-94.

[127] Lohania, B., Masonb, D.C., Scottb, T.R. and Sreenivasa, B., 2006, Extraction of tidal channel networks from aerial photographs alone and combined with laser altimetry. *International Journal of Remote Sensing*, 27, pp. 5–25.

[128] Lopera, O., Milisavljevie, N., Daniels, D. and Macq, B., 2007, Time-frequency domain signature analysis of GPR data for landmine identification. *4th International Workshop on Advanced Ground Penetrating Radar*, pp.159–162.27-29.

[129] Lopez-Dekker, P. and Frasier, S.J., 2004, Radio acoustic sounding with a UHF volume imaging radar. *Journal of Atmospheric and Oceanic technology*, 21, pp. 766–776.

[130] Lopez-Dekker, P., Mallorqui, J.J., Serra-Morales, P. and Sanz-Marcos, J., 2008, Phase synchronization and doppler centroid estimation in fixed receiver bistatic SAR systems. *IEEE Transactions on Geoscience and Remote Sensing*, 46, pp. 3459–3471.

[131] Lopez-Dekker, P., Mallorqui, J.J., Serra-Morales, P. and Sanz-Marcos, J., 2007, Phase and temporal synchronization in bistatic SAR systems using

sources of opportunity. In *IEEE International Geoscience and Remote Sensing Symposium, IGARSS '07*, 23–28 Jul. 2007, Barcelona, Spain, pp. 97–100.

[132] Lowe, D.G., 2004, Distinctive image features from scale-invariants key points. *International Journal of Computer Vision*, 60, pp. 91–110.

[133] Luis, A. J. and Pandey, P. C., 2005, Characteristics of atmospheric divergence and convergence in the Indian Ocean inferred from scatterometer winds. *Remote Sensing of Environment*, 97, pp.231–237.

[134] Maaref, N., Millot, P., Pichot, C. and Picon, O., 2009, A study of UWB FM-CW radar for the detection of human beings in motion inside a building. *IEEE Transactions on Geoscience and Remote Sensing*, 47, pp. 1297–1300.

[135] Madhavan, B. B., Venkataraman, G., Mohan, B. K. and Shah, S. D., 1999, Airborne SAR and IRS-1A LISS II data interpretation of coastal geomorphology in godavari delta, India. *Geocarto International*, 14, pp.52–61.

[136] Madhavan, B. B., Venkataraman, G., Shah, S. D. and Mohan, B. K., 1997, Revealing the geology of the Great Nicobar Island, Indian Ocean, by the interpretation of airborne synthetic aperture radar images. *International Journal of Remote Sensing*, 18, pp.2723–2742.

[137] Magid, A., Rotman, S. R. and Weiss, A. M., 1990, Comment on picture thresholding using an iterative selection method. *IEEE Transactions on Systems, Man and Cybernetics*, 20, pp. 1238–1239.

[138] Mahfouz, M., Fathy, A., Yang, Y., Ali, E.E. and Badawi, A., 2005, See through wall imaging using ultra wideband pulse systems. In *34th Applied Imagery and Pattern Recognition Workshop, AIPR' 05*, 19–21 Oct. 2005, Washington D.C., USA, pp. 8–16.

[139] Mahtre, B.M., Kankanhalli, M.S. and Lee, W.F., 1997, Shape measures for content based image retrieval: a comparison. *Information Processing and Management*, 33, pp. 319–337.

[140] Mallett, J.D. and Brennan, L.E., 1962, Cumulative probability of detection for targets approaching a uniformly scanning search radar. In *Proceedings of the IEEE*, 51, pp. 596–601.

[141] Merwe, A. and Gupta, I.J., 2000, A novel signal processing technique for clutter reduction in GPR measurements of small, shallow land mines. *IEEE Transactions on Geoscience and Remote Sensing*, 38, pp. 2627–2637.

[142] Mikhnev, V.A. and Vainikainen, P., 2003, Single-reference near-field calibration procedure for step-frequency ground penetrating radar. *IEEE Transactions on Geoscience and Remote Sensing*, 41, pp. 75–80.

[143] Mobasseri, B.G. and Rosenbaum, Z., 2008, 3D Classification of Through-the-Wall Radar Images Using Statistical Object Models. In *IEEE Southwest Symposium Image Analysis and Interpretation, SSIAI' 2008*, 24-26 March 2008, Santa Fe New Mexico USA, pp.149–152.

[144] Mohan, S., 1986, An approach for the relative calibration of radar imagery. *International Journal of Remote Sensing*, 7, pp.589–595.

[145] Mondal, P. and Chakrabarty, A., 2008, Slotted Waveguide Antenna with Two Radiation Nulls. *IEEE Transactions on Antennas & Propagation*, 56, pp. 3045-3049.

[146] Moriyama, T., Nakamura, M., Yamaguchi, Y., Yamada, H. and Boerner, W. M., 1999, Classification of target buried in underground by radar polarimetry. *IEICE Transactions on Communication,* E82-B, pp. 951–957.

[147] Morrow, I. L. and Van Genderen, P.A., 2001, 2D Polarimetric back propagation algorithm for ground-penetrating radar applications. *Microwave Optical Technology Letters*, 28, pp. 1–4.

[148] Morrow, I.L. and Genderen, P.V., 2002, Effective imaging of buried dielectric objects. *IEEE Transactions on Geoscience and Remote Sensing*, 40, pp. 943–949.

[149] Muqaibal, A.H. and Safaai-Jazi, A., 2003, A new formulation for characterization of materials based on measured insertion transfer function. *IEEE Transactions on Microwave Theory and Techniques*, 51, pp. 1946–1951.

[150] Muqaibel, A., Safaai-Jazi, A., Bayram, A., Attiya, A.M. and Riad, S.M., 2005, Ultra-wideband through the wall propagation. In *IEE Proceedings Microwave Antennas Propagation*, 152, pp. 581–588.

[151] Nag, S., Fluhler, H. and Barnes, M., 2001, Preliminary interferometric images of moving targets obtained using a time modulated ultra wide band through

wall penetration radar. In *Proceedings of the 2001 IEEE Radar Conference*, 1–3 May 2001, Atlanta, GA, USA, pp. 64–69.

[152] Nagarajan, R. and Venkataraman, G., 1988, Reflectance characteristics of rocks in geological remote sensing. *Journal of the Indian Society of Remote Sensing*, 16, pp. 11–14, 1988.

[153] Narayanan, R. M., Xu, X. and Henning, J. A., 2004, Radar penetration imaging using ultra wideband random noise waveforms. *IEE Proceedings Radar Sonar Navig*ation , 151, pp. 143–148.

[154] Narayanan, R.M., 2008, Through-wall radar imaging using UWB noise waveforms. *Journal of the Franklin Institute*, 345, pp. 659–678.

[155] Nguyen, L., Le, C. and Gaunaurd, G.C., 2007, Computerized tomography radar target imaging behind opaque walls. *Optical Engineering*, 46, pp. 076201–1–10.

[156] Nicolaescu, I. and Genderen, P.V., 2008, Archimedean spiral antenna calibration procedures to increase the downrange resolution of a SFCW radar. *International Journal of Antennas and Propagation*, 2008, pp. 1–7.

[157] Nikolic, M.M., Nehorai, A. and Djordjevic, A.R., 2009, Estimating moving targets behind reinforced walls using radar. *IEEE Transactions on Antennas and Propagation*, 57, pp.3530–3538.

[158] Oberger, G., Buchegger, T., Scimback, E., Pfeil, R., Stelzer, A. and Weigel, R., 2006, Adaptive ground clutter removal algorithm for ground penetrating radar applications in harsh environments. *Sensing and Imaging*, 7, pp. 71–89.

[159] Otsu, N., 1979, A threshold selection method from gray level histograms. *IEEE Trans. Systems, Man and Cybernetics*, 9, pp.62–66.

[160] Ozdemir, C., Demirci, S. and Yigit, E., 2008, Practical algorithms to focus B-scan GPR images: theory and application to real data. *Progress in Electromagnetic Research, PIER*, B, 6, pp. 109–128.

[161] Ozdemir, C., Demirci, S., Yigit, E. and Kavak, A., 2007, A hyperbolic summation method to focus B-scan ground penetrating radar images: An experimental study with a stepped frequency system. *Microwave and Optical Technology Letters*, 49, pp. 671–676.

[162] Ozdemir, C., Lim, S. and Ling, H., 2004, A synthetic aperture algorithm for ground penetrating radar imaging. *Microwave and Optical Technology Letters*, 42, 412–414.

[163] Pabari, J.P, Acharya, Y.B., Marchant, S. N. and Desai, U. B., 2009, Investigation of Wireless Sensor Deployment Schemes for In-Situ Measurement of Water Ice near Lunar South Pole. *Sensors & Transducers Journal*, 111, pp. 86 – 105.

[164] Paik, J., Lee, C.P. and Abidi, M.A., 2002, Image processing based mine detection techniques: a review. *Subsurface sensing technologies and applications*, 3, pp. 153–201.

[165] Pandey, P. C. and Kakar, R., 1982, An empirical microwave emissivity model for a foam-covered sea. *IEEE Journal of Oceanic Engineering*, 7, pp.135–140.

[166] Pandey, P. C., Gairola, R. M. and Gohil, B. S., 1986, Wind-wave relationship from SEASAT radar altimeter data. *Boundary-Layer Meteorology*, 37, pp.263–269.

[167] Pandey, P.C. and Hariharan, T. A., 1984, Advances in microwave remote sensing of the ocean and atmosphere. *Journal of Earth System Science*, 93, pp.257–282.

[168] Papson, S. and Narayanan, R.M., 2005, Multiple location SAR/ISAR image fusion for enhanced characterization of targets. In *Proceedings of SPIE*, 5788, pp. 128–139.

[169] Partida, J. T. G., Gonzalez, A., Garcia, M. B., Naranjo, B. P. D. and Alonso, J. I., 2009, Through the wall surveillance with millimeter wave LFMCW radars. *IEEE Transactions on Geoscience and Remote Sensing*, 47, pp. 1–10.

[170] Pasolli, E., Melgani, F. and Donelli, M., 2009, Automatic analysis of GPR images: a Pattern-Recognition Approach. *IEEE Transactions on Geoscience and Remote Sensing*, 47, pp. 2206–2217.

[171] Peck, R., Olsen, C. and Devore, J., *Introduction to Statistics and data analysis*. Singapore: Duxbery Thomson Learning, 2001.

[172] Pena, D., Feick, R., Hristov, H.D. and Grote, W., 2003, Measurement and modeling of propagation losses in brick and concrete walls for the 900-MHz band. *IEEE Transactions on Antennas and Propagation*, 51, pp. 31–39.

[173] Pieraccini, M., Luzi, G., Noferini, L., Mecatti, D. and Atzeni, C., 2004, Joint time-frequency analysis for investigation of layered masonry structures using penetrating radar. *IEEE Transactions on Geoscience and Remote Sensing*, 42, pp. 309–317.

[174] Pipia, L., Fabregas, X., Aguasca, A., Lopez-Martinez, C., Duque, S., Mallorqui, J.J. and Marturia, J., 2009, Polarimetric differential SAR interferometry: first results with ground-based measurements. *IEEE Geoscience and Remote Sensing Letters,* 6, pp. 167–171.

[175] Potin, D., Duflos, E. and Vanheeghe, P., 2006, Landmine ground-penetrating radar signal enhancement by digital filtering. *IEEE Transactions on Geoscience and Remote Sensing*, 44, pp. 2393–2406.

[176] Potin, D., Vanheeghe, P., Duflos, E. and Davy, M., 2006, An abrupt change detection algorithm for buried landmines localization. *IEEE Transactions on Geoscience and Remote Sensing*, 44, pp. 260–272.

[177] Prats, P. and Mallorqui, J.J. 2003, Estimation of azimuth phase undulations with multisquint processing in airborne interferometric SAR images. *IEEE Transactions on Geoscience and Remote Sensing*, 41, pp. 1530–1533.

[178] Raghavan, R.S., 1991, A method for estimating parameters of K-distributed clutter. *IEEE Transactions on Aerospace and Electronic Systems*, 27, pp. 238–246.

[179] Ram, S.S., Li, Y., Lin, A. and Ling, H., 2008, Doppler-based detection and tracking of humans in indoor environments. *Journal of Franklin Institute*, 345, pp. 679–699.

[180] Rao, Y. S., Sharma, S., Garg, V. and Venkataraman, G., 2006, Soil Moisture Mapping over India using Aqua AMSR-E derived Soil Moisutre Product. In *IEEE International Geoscience and Remote Sensing Symposium, IGARSS '06*, 31 Jul. – 04 Aug., Denver, CO, USA, pp. 2999–3002.

[181] Ratha, D. S. and Venkataraman, G., 1997, Application of statistical methods to study seasonal variation in the mine contaminants in soil and groundwater of Goa, India. *Environmental Geology*, 29, pp. 253–262.

[182] Ren, Y., Lai, C., Chen, P. and Narayanan, R.M., 2009, Compact ultrawideband UHF array antenna for through-wall radar applications. *IEEE Antennas and Wireless Propagation Letters*, 8, pp. 1302–1305.

[183] Reppert, P.M., Morgan, F.D. and Toksoz, M.N., 2000, Dielectric constant determination using ground-penetrating radar reflection coefficients. *Journal of Applied Geophysics*, 43, pp. 189–197.

[184] Richalot, E., Bonilla, M., Wong, M.F., Hanna, V.F., Baudrand, H. and Wiart, J., 2000, Electromagnetic propagation into reinforced-concrete walls. *IEEE Transactions on Microwave Theory and Techniques*, 48, pp. 357–366.

[185] Robinson, L.A., Weir, W.B. and Young, L., 1974, Location and recognition of discontinuities in dielectric media using synthetic RF pulses. *IEEE Proceedings*, 62, pp. 36- 44.

[186] Rubin, D. and Thayer, D., 1982, EM algorithms for factor analysis. *Psychometrika*, 47, pp. 69–76.

[187] Sahoo, P.K., Soltani, S. and Wong, A.K.C., 1988, A survey of thresholding techniques. *Computer Vision, Graphics and Image Processing*, 41, pp. 233–260.

[188] Sanz-Marcos, J., Lopez-Dekker, P., Mallorqui, J.J., Aguasca, A. and Prats, P., 2007, SABRINA: a SAR bistatic receiver for interferometric applications. *IEEE Geoscience and Remote Sensing Letters*, 4, pp. 307–311.

[189] Savelyev, T. G., Kempen, L.V. and Sahli, H., 2004, Deconvolution techniques, *Ground Penetrating Radar*, 2nd ed. ser. IEE Radar, Sonar, Navigation and Avionics Series 15.Ed. London, U.K.:Inst. Electr. Eng., 2004, pp. 298–310.

[190] Savelyev, T.G., Kempen, L.V., Sahli, H., Sachs, J. and Sato, M., 2007, Investigation of time–frequency features for GPR landmine discrimination. *IEEE Transactions on Geoscience and Remote Sensing*, 45, pp. 118–129.

[191] Schleher, D.C., 1976, Radar detection in Weibull clutter. *IEEE Transactions on Aerospace and Electronic Systems*, 12, pp. 736–743.

[192] Shihab, S., Al-Nuaimy, W. and Huang, Y., 2003, A comparison of segmentation techniques for target extraction in ground penetrating radar data. In *2nd International Workshop on Advanced Ground Penetrating Radar*, 14-16 May 2003, Delft, Netherlands, pp. 95–100.

[193] Singh, A.K., 2010, Dish to digital, amazing growth in military radar antenna technology. *Journal of Indian Institute of Science*, 90, pp. 413–451.

[194] Singh, A.K., Elizabeth, S.A. and Dongaonkar, D, 2007, Ultra low side lobe electronically steerable multibeam antenna system for long range 3D naval surveillance radar. In *IEEE Radar Conference*, USA, pp. 457–462.

[195] Singh, A.K., Elizabeth, S.A. and Kumar, P., 2007, Multi beam antenna system for portable 3-D surveillance radar. In *Second European Conference on Antennas and Propagation, EuCAP–2007*, 11–16 Nov., Edinburg, UK, pp. 1–4.

[196] Singh, D., Choudhary, N.K. and Tiwari, K.C., 2009, Shape recognition of shallow buried metallic objects at X-band using ANN and image analysis techniques. *Progress In Electromagnetics Research B*, 13, pp. 257–273.

[197] Singh, D., Gaikwad, A.N., Verma, P.K. and Nigam, M.J., 2009, Study of wall effect for size determination in through wall imaging. In *International Radar Symposium India, IRSI-2009*, Bangalore, India.

[198] Singh, G., Kumar, V., Mohite, K., Venkataraman, G., Rao, Y. S. and Snehmani, 2006, Snow wetness estimation in Himalayan snow covered regions using ENVISAT-ASAR data. In *Proceedings of SPIE*, 6410, 641008.

[199] Singh, G., Kumar, V., Venkataraman, G, Rao, Y.S. and Snehmani, 2007, Snow porosity estimation using advanced synthetic aperture radar single look complex data analysis and its effects on backscattering coefficient. *Journal of Applied Remote Sensing*, 1, 013522, pp. 1-18.

[200] Singh, K.P., Gray, A.L., Hawkins, R.K. and O'Neil, R.A., 1986, The influence of surface oil on C-and Ku-band ocean backscatter. *IEEE Transactions on Geoscience and Remote Sensing*, GE-24, pp. 738–744.

[201] Skolnik, M.I., 2001, *Introduction to RADAR systems*, 3rd ed., New York, NY, McGraw-Hill.

[202] Soldovieri, F. and Solimene, R., 2007, Through-wall imaging via a linear inverse scattering algorithm. *IEEE Geoscience and Remote Sensing Letters*, 4, pp. 513–517.

[203] Soldovieri, F., Leone, G. and D'Urso, M., 2009, A simple strategy for life signs detection via an X-band experimental set-up. *Progress in Electromagnetics Research C*, 9, pp. 119–129.

[204] Soldovieri, F., Solimene, R. and Pierri, R., 2009, A simple strategy to detect changes in through the wall imaging. *Progress in Electromagnetic Research M, PIER*, 106, pp. 75–89.

[205] Soliman, M. and Wu, Z., 2008, Buried object location based on frequency-domain UWB measurements. *Journal of Geophysics and Engineering*, 5, pp. 221–231.

[206] Song, L., Yu, C. and Liu, Q. H., 2005, Through-wall imaging (TWI) by radar: 2-D tomographic results and analyses. *IEEE Transactions on Geoscience and Remote Sensing*, 43, pp. 2793–2798.

[207] Soumekh, M., 1995, Reconnaissance with ultra wideband UHF synthetic aperture radar. *IEEE Signal Processing Magazine*, 12, pp. 21–40.

[208] Spagnolini, U., 1997, Permittivity measurements of multilayered media with monostatic pulse radar. *IEEE Transactions on Geoscience and Remote Sensing*, 35, pp. 454–563.

[209] Tantum, S. L., Wei, Y., Munshinand, V.S. and Collins, L.M., 2002, A comparison of algorithms for landmine detection and discrimination using ground penetrating radar. In *Proceedings of SPIE,* 4742, pp. 728–735.

[210] Taylor, D.J., 2001, *Ultra-wideband Radar Technology*, pp. 303–325. (CRC Press, USA).

[211] Tello, M., Lopez-Dekker, P. and Mallorqui, J.J., 2010, A novel strategy for radar imaging based on compressive sensing. *IEEE Transactions on Geoscience and Remote Sensing*, 48, pp. 4285–4295.

[212] Tien, K.J.C., Judge, J. and De-Roo, R.D., 2004, Comparsion of different microwave radiometric calibration techniques. In *IEEE International Geoscience and Remote Sensing Symposium, IGARSS '04*, 20–24 Sept. 2004, Anchorage, Alaska, pp. 3748–3751.

[213] Tien, K.J.C., Roo, R.D.D., Judge, J. and Pham, H., 2007, Comparison of calibration techniques for ground-based C-band radiometers. *IEEE Geoscience and Remote Sensing Letters*, 4, pp. 83–87.

[214] Urazghildiiev, I., Ragnarsson, R. and Rydberg, A., 2007, High-resolution estimation of ranges using multiple-frequency CW radar. *IEEE Transactions on Intelligent Transportation Systems*, 8, pp. 332–339.

[215] Venkata, N.D., Kite, T.D., Geisler, W.S., Evans, B.L. and Bovik, A.C., 2000, Image quality assessment based on a degradation model. *IEEE Transactions on Image Processing*, 9, pp. 636–650.

[216] Venkataraman, G., Madhavan, B. B., Ratha, D. S., Antony, J. P., Goyal, R. S., Banglani, S. and Roy, S. S., 2000, Spatial modeling for base-metal mineral exploration through integration of geological data sets. *Natural Resources Research*, 9, pp. 27–42.

[217] Verma, P.K., Gaikwad, A.N., Singh, D. and Nigam, M.J., 2009, Analysis of clutter reduction techniques for through wall imaging in UWB range. *Progress In Electromagnetics Research B*, 17, pp. 29–48.

[218] Vitebskiy, S., Carin, L., Ressler, M.A. and Le, F.H., 1997, Ultra-wideband, short-pulse ground-penetrating radar: simulation and measurement. *IEEE Transactions on Geoscience and Remote Sensing*, 35, pp. 762–772.

[219] Wang, G. and Amin, M.G., 2006, Imaging through unknown walls using different standoff distances. *IEEE Transactions on Signal Processing*, 54, pp. 4015–4025.

[220] Wang, G., Amin, M. G. and Zhang, Y., 2006, New approach for target locations in presence of wall ambiguities. *IEEE Transactions on Aerospace and Electronic Systems*, 42, pp. 301–315.

[221] Wehner, D.R., 1995, *High Resolution Radar*, (Artech House, Norwood, MA).

[222] Wei, G. W., 1999, Generalized Perona-Malik equation for Image restoration. *IEEE Signal Proc. Letters*, 6, No.7, 165–167.

[223] Withington, P., Fluhler, H. and Nag, S., 2003, Enhancing homeland security with advanced UWB sensors. *IEEE Microwave Magazine*, 4, pp. 51–58.

[224] Wong, A.K.C. and Sahoo, P.K., 1989, A gray level threshold selection method based on maximum entropy principle. *IEEE Transactions on Systems, Man, and Cybernetics*, 19, pp. 866–871.

[225] Wong, S.K., 2009, High range resolution profiles as motion-invariant features for moving ground targets identification in SAR-based automatic target recognition. *IEEE Transactions on Aerospace and Electronic Systems*, 45, pp. 1017–1039.

[226] Wu, N. and Zhang, J., 2003, Factor analysis based anomaly detection. In *Information Assurance Workshop, IEEE Systems, Man and Cybernetics Society*, 18–20 Jun. 2003, US military academy, Newyork, USA, pp. 108–115.

[227] Xu, X., Miller, E.L., Rappaport, C.M. and Sower, G.D., 2002, Statistical method to detect subsurface objects using array ground-penetrating radar data. *IEEE Transactions on Geoscience and Remote Sensing*, 40, pp. 963–976.

[228] Yacoub, H. and Sarkar, T.K., 2009, A Homomorphic approach for through-wall sensing. *IEEE Transactions on Geoscience and Remote Sensing*, 47, pp. 1318–1327.

[229] Yahia, H., Turiel, A., Chrysoulakis, N., Grazzini, J., Prastacos, P. and Herlin, I., 2007, Multifractal pre-processing of AVHRR images to improve the determination of smoke plumes from large fire. In *Proceedings of IEEE International Geoscience and Remote Sensing Symposium, (IGARSS '07)*, 23-27 July 2007, Barcelona, Spain, pp. 5335–5338.

[230] Yajima, Y., Yamaguchi, Y., Sato, R., Yamada, H. and Boerner, W. M., 2008, POLSAR image analysis of wetlands using a modified four-component scattering power decomposition. *IEEE Transactions on Geoscience and Remote Sensing*, 46, pp. 1667–1673.

[231] Yamaguchi, Y. and Moriyama, T., 1996, Polarimetric detection of objects buried in snowpack by a synthetic aperture FMCW radar. *IEEE Transactions on Geoscience and Remote Sensing*, 34, pp. 45–51.

[232] Yamaguchi, Y., Maruyama, Y., Kawakami, A., Sengoku, M. and Abe, T., 1991, Detection of objects buried in wet snowpack by an FMCW radar. *IEEE Transactions on Geoscience and Remote Sensing*, 29, pp. 201–208.

[233] Yamaguchi, Y., Mitsumoto, M., Sengoku, M. and Abe, T., 1992, Human body detection in wet snowpack by an FMCW radar. *IEEE Transactions on Geoscience and Remote Sensing*, 30, pp. 186–189.

[234] Yamaguchi, Y., Mitsumoto, M., Sengoku, M. and Takeo, A., 1994, Synthetic aperture FM-CW radar applied to the detection of objects buried in snowpack. *IEEE Transactions on Geoscience and Remote Sensing*, 32, pp. 11–18.

[235] Yamaguchi, Y., Nishikawa, T., Sengoku, M. and Boerner, W.M., 1995, Two-dimensional and full polarimetric imaging by a synthetic aperture FMCW

radar, *IEEE Transactions on Geoscience and Remote Sensing*, 33, pp. 421–427.

[236] Yang, C, Wu, B. and Ko, C., 1998, A ray tracing method for modeling Indoor wave propagation and penetration. *IEEE Transcations on Antennas and Propagation*, 46, pp. 907–919.

[237] Yang, J., Peng, Y. N. and Lin, S. M., 2001, Similarity between two scattering Matrices. *Electronics Letters*, 37, pp. 193–194.

[238] Yang, J., Xiong, T. and Peng, Y.N., 2006, Polarimetric SAR image classification by using generalized optimization of polarimetric contrast enhancement. *International Journal of Remote Sensing*, 27, pp. 3413–3424.

[239] Yang, J., Yamaguchi, Y., Boerner, W. and Lin, S., 2000, Numerical methods for solving the optimal problem of contrast enhancement. *IEEE Transactions on Geoscience and Remote Sensing*, 38, pp. 965–971.

[240] Yang, Y. and Fathy, A.E., 2005, See-through-wall imaging using ultra wideband short–pulse radar system. In *IEEE Antennas and Propagation Society International Symposium*, 3–8 Jul. 2005, Washington, DC, USA, pp. 334–337.

[241] Yang, Y. and Fathy, A.E., 2009, Development and implementation of a real time see through wall radar system based on FPGA. *IEEE Transactions on Geoscience and Remote Sensing*, 47, pp. 1270–1280.

[242] Yarovoy, A.G., Savelyev, T.G., Aubry, P. J., Lys, P. E. and Ligthart, L. P., 2007, UWB array-based sensor for near-field imaging. *IEEE Transactions on Microwave Theory and Techniques*, 55, pp. 1288–1295.

[243] Yemelyanov, K.M., Engheta, N., Hoorfar, A. and McVay, J.A., 2009, Adaptive polarization contrast techniques for through-wall microwave imaging applications. *IEEE Transactions on Geoscience and Remote Sensing*, 47, pp. 1362–1374.

[244] Yigit, E., Demirci, S., Ozdemir, C. and Kavak, A., 2007, A synthetic aperture radar based focusing algorithm for B-scan ground penetrating radar imagery. *Microwave and Optical Technology Letters*, 49, pp. 2534–2540.

[245] Yoon, Y. S. and Amin, M.G., 2009, Spatial filtering for wall-clutter mitigation in through the wall radar imaging. *IEEE Transactions on Geoscience and Remote Sensing*, 47, pp. 3192–3208.

[246] Yoon, Y.S. and Amin, M.G., 2008, High-resolution through-the-wall radar imaging using beam space music. *IEEE Transactions on Antennas and Propagation*, 56, pp.1763–1774.

[247] Younis, M., Fischer, C. and Wiesbeck, W., 2003, Digital beamforming in SAR systems. *IEEE Transactions on Geoscience and Remote Sensing*, 41, pp. 1735–1739.

[248] Zetik, R., Sachs, J. and Thoma, R., 2005, Modified cross-correlation back projection for UWB imaging: numerical examples. In *IEEE International Conference on Ultra-Wideband, ICU 2005,* 5-8 Sep.2005,Zurich, Switzerland, pp.650–654.

[249] Zhang, D. and Lu, G., 2003, A comparative study of curvature scale space and Fourier descriptors for shape based image retrieval. *Journal of Visual communication and Image Representation*, 14, pp. 41–60.

[250] Zhang, W. and Hoorfar, A., 2010, Through the wall target localization with time reversal music method. *Progress in Electromagnetic Research, PIER*, 106, pp. 75–89.

[251] Zhao, M., Shea, J.D., Hagness, S.C., Van der Weide, D.W., 2006, Calibrated free-space microwave measurements with an ultrawideband reflectometer-antenna system. *IEEE Microwave and wireless components*, 16, pp. 675–677.

[252] Zoubir, A.M., Chant, I.J., Brown, C.L., Barkat, B. and Abeynayake, C., 2002, Signal processing techniques for landmine detection using impulse ground penetrating radar. *IEEE Sensors J*ournal, 2, pp. 41–51.

Author's Publications

International Journals

[1] Chandra R., Gaikwad, A. N., Singh, D. and Nigam, M. J., 2008, An approach to remove the clutter and detect the target for ultra-wideband through-wall imaging. *Journal of Geophysics and Engineering*, 5, pp. 412–419, 2008.

[2] Verma, P. K., Gaikwad, A., N., Singh, D. and Nigam, M. J., 2009, Analysis of clutter reduction techniques for through wall imaging in UWB range. *Progress In Electromagnetics Research B,* 17, pp. 29-48.

[3] Gaikwad, A. N., Singh, D. and Nigam, M. J., 2010, Application of clutter reduction techniques for detection of metallic and low dielectric target behind the brick wall by SFCW radar in UWB range. *IET Radar Sonar and Navigation*, 5, pp. 416–425.

[4] Gaikwad, A. N., Singh, D. and Nigam, M. J., A novel approach to detect and classify the targets for through wall imaging system is under review in *IEEE Transaction on GeoScience and Remote sensing* (Second review completed).

National/International Conferences

[1] Gaikwad, A., N., Verma, P. K., Singh, D. and Nigam, M. J., 2009, Study of wall effect for size determination in through wall imaging," presented in International Radar symposium India, (IRSI-09), Bangalore, India, 8-11 Dec. 2009, pp. 387–391.

[2] Verma, P. K., Gaikwad, A., N., Singh, D. and Nigam, M. J., 2009, Detection and identification of low dielectric material object in presence of metallic object using ultra wideband through wall imaging. In *International Radar symposium India*, (*IRSI-09*), Bangalore, India, 8-11 Dec. 2009, pp. 392–396.

[3] Gaikwad, A. N., Singh, D. and Nigam, M. J., 2010, High resolution ultra wideband based SFCW radar to detect and image objects behind wall. In *2nd* Rastriya Yuva Vaigyanik Sammelan 2010, Dehradun, Uttarakhand, Feb. 6–7, 2010.

[4] Gaikwad, A. N., Singh, D. and Nigam, M. J., 2011, Recognition of target in through wall imaging using shape feature extraction. In *IEEE International Geoscience and Remote sensing* 24–29 Jul., Vancouver, Canada, (accepted for presentation).